UNIVERSIDAD DE CONCEPCIÓN
FACULTAD DE CIENCIAS FÍSICAS Y MATEMÁTICAS
MAGÍSTER EN CIENCIAS CON MENCIÓN EN FÍSICA

Gliese 832c: ¿Actividad Estelar o Exoplaneta?

Gliese 832c: Stellar Activity or Exoplanet?

Profesores: Dr. Nicola Astudillo Defru
Dr. Ronald Mennickent Cid
Dr. Sandro Villanova

Tesis para ser presentada a la Dirección de Postgrado de la Universidad de Concepción

PAULA GORRINI HUAIQUIMILLA
CONCEPCION - CHILE 2020

"... we cannot accept anything as granted, beyond the first mathematical formulae. Question everything else. "

Maria Mitchell

UNIVERSIDAD DE CONCEPCIÓN

Abstract

Facultad de Ciencias Físicas y Matemáticas
Departmento de Astronomía

MSc.

Stellar activity mimics planetary signal in the habitable zone of Gliese 832

by Paula GORRINI

Exoplanets are planets located outside our Solar System. The search of these objects have grown during the years due to the scientific interest and to the advances on astronomical instrumentation. There are many methods used to detect exoplanets, where one of the most efficient is the radial velocity (RV) method. But this technique accounts false positives as stellar activity can produce RV variation with an amplitude of the same order of the one induced by a planetary companion. In this thesis, we study Gliese 832, an M dwarf located 4.96 pc away from us. Two planets orbiting this star were found independently by the RV method: a gas-giant planet in a wide orbit, and a super Earth or mini-Neptune located within the stellar habitable zone. However, the orbital period of this latter planet is close to the stellar rotation period, casting doubts on the planetary origin of this RV signal. This motivated us to perform a rigours analysis on stellar activity in order to determine if this phenomenon is causing these RV variations. We re-calculated the period of the stellar rotation using Gaussian process (GP) regression on the S-index activity indicator. This resulted in a stellar rotation period of $35.76\ ^{+0.95}_{-0.26}$ days, in agreement with the reported value but reducing the errors by 89.78%. By performing a 1-planet Keplerian model, the Generalised Lomb Scargle (GLS) periodogram displayed the strongest signal around the reported planet in a wide orbit (planet b). The periodogram of the residuals showed a significant (FAP $< 1\%$) signal near 184, while the signal of the inner planet (planet c) does not reach this level of confidence. By incorporating a GP trained on the S-index, these signals were absorbed. We subsequently made 2-planets Keplerian models including the signal of planet b plus the 35 and 184 days signal in different models, and then added a GP (stellar activity) to each model. By comparing our different models in a Bayesian framework, the favored model resulted to be 1-planet plus stellar activity model, updating in this way the orbital solutions of the Gl 832 system. Since the 35 days signal is attributable to stellar rotation, we conclude planet c is an artifact of stellar activity.

Acknowledgements

First, I would like to express my deepest gratitude to my supervisor Nicola for his guidance and support during my Master. I enjoyed very much working on this topic, learning new things and put into practice my knowledge. Your suggestions and corrections made me a better student. Thank you for always encouraging and motivating me through this amazing field. I am also grateful to you for allowing me to perform a professional observation in La Silla Observatory with HARPS. This was one of the best experiences that I had during my thesis. Thank you for everything!

Also, I gratefully thank professor Ronald and Sandro, for being part of this thesis. Your advice and revising were fundamental for the fulfillment of this study. I am also grateful for the Stellar Variability Group (SVG), for which all the members helped to improve this work.

Thanks to my mom and dad, Gloria and Bruno, who worked hard for giving me (and my brothers) everything, especially a good education. Without you this thesis would have not been possible. I will be forever grateful for the effort, comfort and support you have provided me during every moment of my life. Also, I thank my brothers Enzo and Tomás, who have accompanied me since my first breath. And I also would like to thank my dear grandmother. I love you all.

I am grateful to my partner Juan, who gave me his love and support during this process. Also to my friends from the office who also provided me with ideas for this thesis, as well as helping me clear my mind during difficult moments. Also, I thank my cousins Fernanda and Camila, who besides being family, are friends. And to my beloved friends Katharina and Aurora, with who I have maintained a beautiful friendship throughout many years in spite of the distance.

I also would like to thank my modern dance teacher Juan Carlos and my ballet teacher Laura. They had taught me the beautiful art of dance. This discipline has been an important part of my life, and therefore, an important part of this thesis.

Finally, I thank funding from CONICYT project 22181925 and to Dirección de Postgrado of Universidad de Concepción whose financial support allowed me to present my results in LARIM 2019.

Contents

List of Figures

List of Tables

To my family . . .

Chapter 1

Context

A planet is an object that satisfies three conditions: it must orbit a star, be massive enough to have a spherical shape and be gravitationally dominant in its orbit. Extrasolar planets, commonly known as exoplanets, are planets that are located outside our Solar System, i.e., they orbit different stars than the Sun. At the beginning, the Solar System was the only planetary system known. But the idea of the existence of exoplanets has raised great interest in humans beings since from remote times we have questioned our origin and if we are alone in the Universe. Ancient philosophers, such as Epicurus (341-270 BC) and modern philosophers such as Giordano Bruno (1548-1600), expressed their belief of other worlds should exist, where this latter man was executed by burning during the Inquisition, as these ideas were against the church and religion.

The bodies in our Solar system that were visible by naked eyed from the Earth were contemplated by the first civilizations, who used the movements of Moon, the Sun, Venus, Mercury, Mars, Jupiter and Saturn to develop calendars. With the invention of the telescope by Galileo Galilei in 1609, other "invisible" objects became a subject of study. Galileo found four satellites orbiting Jupiter, and he looked and studied Saturn's rings, the phases of Venus, the Sun's spots and the unsmooth surface of the Moon. His observations, alongside the study of elliptical orbit performed by Johannes Kepler, gave strong evidence to the Heliocentric model of Nicolaus Copernicus. After Galileo stated that the Heliocentric model was correct, he was accused by the church of being a heretic, being sentenced to life imprisonment. Despite of this, his discoveries inspired next generations of scientists and philosophers.

Later on, Uranus, Neptune, Pluto, orbiting satellites, comets and asteroids were found. By the beginning of the 20th century, there was still no technology capable of detecting exoplanets, and no one knew for certain whether our Solar System was typical or singular. And due to the lack of evidence, many astronomers were unenthusiastic about the search of exoplanets, and those who were interested were viewed as "dreamers". But with the advance of technology, it was later possible to detect low-mass stars and brown dwarfs, allowing the discovery of exoplanets to be more achievable.

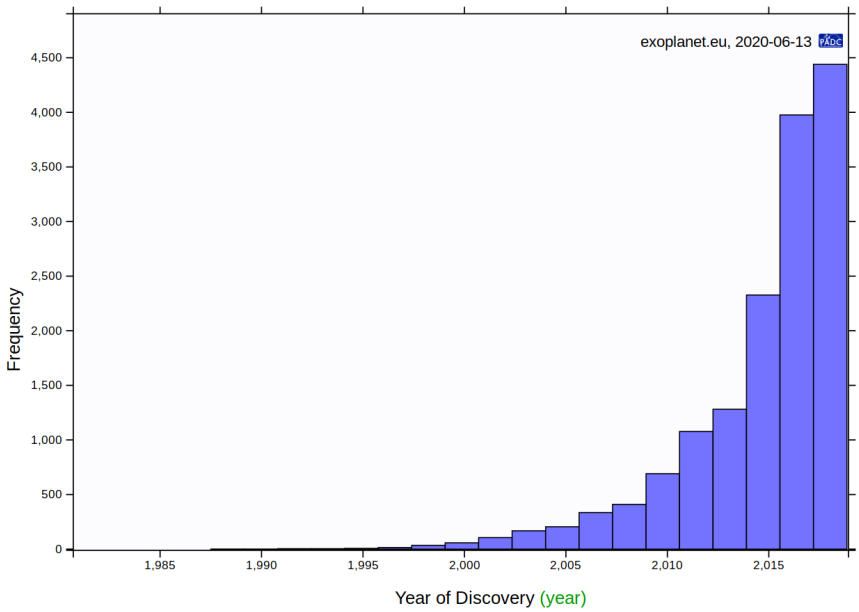

FIGURE 1.1: Cumulative histogram of exoplanets discovered as a function of time (taken from The Extrasolar Planets Encyclopaedia).

The search of these extrasolar systems has become one the most attractive subject for research, which has begun at the end of the last century. The first exoplanet discovery was made by Wolszczan and Frail (1992), detecting a planet orbiting around a pulsar. A few years later, 51 Pegabsi b, an exoplanet around a Sun-like star, was discovered in 1995 by Mayor et al. (1995), obtaining the Nobel Prize in physics 24 years later. Its discovery was remarkable as it marked the beginning of the exoplanetary hunt and it demonstrated the capability and precision of the instrument behind the discovery.

This Jupiter-like planet was found to be orbiting its star in a close-orbit, being different from the planets in our Solar System. In this sense, the study of exoplanets allows us to understand our own Solar System, being essential in the development of planetary formation and evolution theories. Theories of planetary formation indicate that planets are formed in protoplanetary discs, which are regions of dust and gas around young stars, where accretion of grain particles end up forming a planet. Giants planets are believed to form far from its host star but slowly spiralled inwards over time. This is known as orbital migration and it explains why some gaseous giants planets have close orbits, such as 51 Pegasi b.

To date (June 2020), there are 4270 exoplanets confirmed, with this number increasing in time due to the great scientific interest and the advances on astronomical instrumentation which allow these planets to be detected. In Fig. 1.1 we observe a cumulative histogram displaying the confirmed exoplanets that has been detected since the early 90's by different techniques.

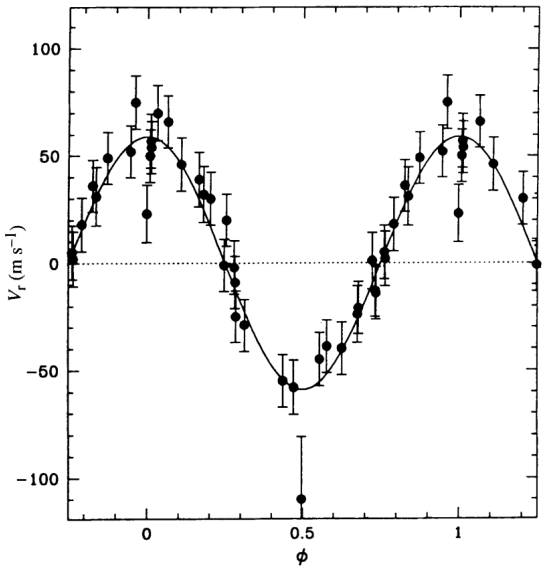

FIGURE 1.2: RV measurments of 51 Pegasi b (taken from Fig. 4 - Mayor et al., 1995).

As we will see in Section 2.1, there are a variety of methods to detect exoplanets, where the most commonly used are the transit and radial velocity (RV) methods. The former consist in the planetary transit, where a planet passes in front of the star causing a decrease in the stellar flux. Since planets orbit periodically their host star, this decrease in flux also occurs periodically, indicating that the star could have a planetary companion. As for the RV method, it is based on the Doppler Effect: due to the presence of a planet the star orbits the center of mass of the system, causing the star to move towards or away from us, generating a blueshift and redshift, respectively, of the stellar spectral lines. These doppler shifts induce periodically variations in the radial velocity of the star, providing us with evidence of the possible presence of a planet in the system. In Fig. 1.2 we observe how 51 Pegasi b was found with this latter method.

Both methods have their advantages and disadvantages. The advantage of the transit method is that it can determine the size of the planet directly, whereas the RV method provides us with the eccentricity of the planetary orbit. Combining both methods, the mass of the planet can be calculated. But these methods have the disadvantage of only working when the planetary system is in our line of sight, reducing the quantity of the planetary system that can be found by these techniques. Still, theses methods have been the most efficient for the detection of exoplanets, especially when used simultaneously.

The detection of planets through the RV method is possible using the available instrumentation nowadays, such as the "High Accuracy Radial Velocity Planet Searcher" (HARPS), an echelle spectrograph that reaches a precision up to 0.97 ms^{-1}, being one of the only instruments with such precision over the world. It is mounted in the 3.6m ESO telescope located in La Silla Observatory. This instrument can detect easily planets orbiting around low mass stars, such as M dwarfs, which make up

about 70% of the stars near the Sun. Their masses ranges from 0.07 to 0.6 $M_{\odot}$, making them ideal to search for Earth-mass planets either by the transit or RV method. In M dwarfs, the *habitable zone* (HZ), which is defined as the range of distances from the host star where a planet could maintain liquid water on its surface, tends to be closer to the star (between 0.03 and 0.4 AU; Kasting, Whitmire, and Reynolds, 1993) as their luminosites are lower compared to Sun-like stars.

But as we will see in Chapter 4, these stars tend to be magnetically active (e.g. Reiners, Joshi, and Goldman, 2012), being able to mimic the effect of a planet. The presence of a planet induces periodic variations on the stellar RV, but quasi-periodic RV variations can also be produced by the activity of the star. These RV variations can be generated by stellar oscillations, granulation, spots, plages, and long activity cycles. Of all of these signatures, one of the most complicated to mitigate their effected are stellar spots. As they rotate within the star, they appear and disappear of the stellar surface, causing an imbalance between the blue and redshifted parts of the stellar surface.

This alters the shape of the spectral lines, leading to RV variations of the order of a few ms^{-1}. Therefore, this phenomena can cause RV variations of the same order that a planetary companion does, leading to false planet detections (e.g. Queloz et al., 2001; Desidera et al., 2004; Bonfils et al., 2007; Huélamo et al., 2008; Santos et al., 2014; Robertson et al., 2014), demonstrating the importance of comprehending and treating the presence of activity signals in the search of exoplanets. In the Gl 832 system, a Jupiter-like planet in a wide orbit (Bailey et al., 2009), and a super Earth or mini-Neptune orbiting within the stellar habitable zone (Wittenmyer et al., 2014) have been detected using the RV methods. The inner planets has a minimum mass of 5.4 Earth-masses $\pm$1.0 and an orbital period of 35.68 $\pm$0.03 days. A recent investigation performed by Suárez Mascareño et al. (2015) shows that the stellar rotation period (45.7 $\pm$ 9.3 days) is close to the planetary orbital period, for which is necessary to perform a rigorous analysis in order to determine if the observed signal is indeed produced by the planetary companion or by stellar magnetic activity.

In this thesis we investigate in depth the RV of Gl 832 and magnetic activity tracers, using spectroscopic high resolution data obtained by HARPS between 2002 and 2018. We also used archival RV data from PFS and UCLES spectograph. The aim of this thesis is to either to confirm the presence of the inner planet or to discard it due to the activity of the star.

This study is structured as follows. In Chapter 2 we introduce the detection methods of exoplanets and give a detail description of the RV method. In Chapter 4 we describe the stellar magnetic activity present in Sun-like stars and M dwarfs, its manifestations and how they can mimic planetary signals. We also describe a Bayesian approach that is used to model stellar activity. In Chapter 5 we explain our study of Gl 832 system and in Chapter 6 we report the main conclusion of this thesis.

Chapter 2

Introduction to Exoplanets

2.1 Detection Methods

A variety of methods are used in order to discover exoplanets. These can be divided into two categories: direct and indirect techniques. The former consist on the detection of the planet itself, while the latter resides on the study of the stellar signal that it is influenced by a planetary companion. Within these categories, the direct imaging (direct method) and the transit, astrometry, microlensing, and radial velocity (indirect methods) are the most-known and used, which are described in this section.

2.1.1 Direct Imaging

We can say that this technique is unique; it allows us to detect the planet directly. Despite their difficulties, as the planet is much fainter than the star, it is possible to observe them. This is done by performing observations in visible wavelength where the reflecting light from their star can be detected, or in the infrared (IR) where the thermal emission of the planet is observable. The planet then must be massive and hot enough to emit in the IR and should be far away from its host star ($a > 5$ AU) so it does not outshine the emission of the planet. Coronographs are usually used in this technique to block the light from the star.

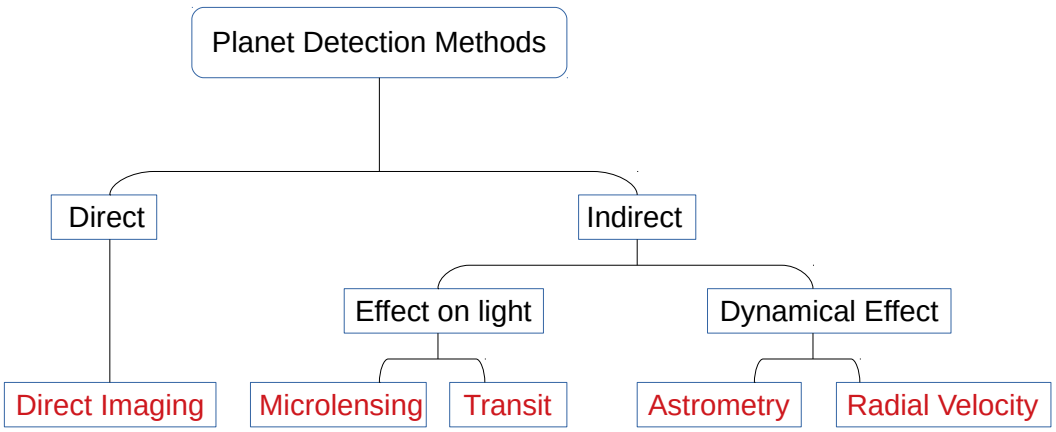

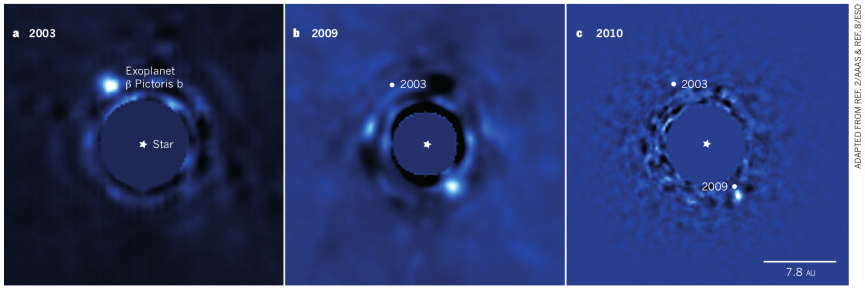

FIGURE 2.1: Infrared images of the planet β Pictoris b obtained by direct imaging in **(a)** 2003, **(b)** 2009 and **(c)** 2010 (taken from Fig. 1 - Barman, 2014).

Direct imagining measures the photons coming from the planet, allowing to perform photometric and spectroscopic studies, obtaining in this way information about the planet such as atmospheric composition of the planet and effective temperature. As it reveals images of planets, this technique can also reveal debris disk. In this sense, this is the only method that allows us to observe the planet directly, obtaining one of the first images of an exoplanet in 2004, in which 2M1207b was detected around a brown dwarf. Fig. 2.1 shows an IR image of the planet β Pictoris b obtained in different epochs.

However, it is very difficult to perform this technique. For instance, if we observed our Solar System from 10 pc away, Jupiter would look 10^{-9} fainter than the Sun with an angular separation of 0.5 arcsec. Also, diffraction, scattering and planet-star contrast are some of the obstacles of this method. Therefore a high quality instrumentation is required to discover exoplanets through direct imaging. For good results, large telescopes are required in order to resolve small angular separation, as

$$\Theta \propto \frac{\lambda}{D} \tag{2.1}$$

where Θ is the angular separation, λ the observation wavelength and D the diameter of the telescope. An extraordinary planetary detection was made by Macintosh et al. (2015) with this technique, in which the angular separation of the instrument was able to resolve less than 0.5 arcsec between the planet and it host star.

2.1.2 Microlensing

Microlensing is based on the event of a lens produced by the gravitational field of a star that is aligned to another background star, magnifying the light of the latter. In order for this to happen, the stars alignment must be in the observer's line of sight. As seen in Fig. 2.2, the star acting as a lens (located at a distance D_L from the observer) bends the light of the source star (located at a distance D_S from the observer), producing an image visible to the observer.

Microlensing events are based on the Einstein radius, which describes how the light is bend from the perfectly alignment of the source, lens, and observer, due to

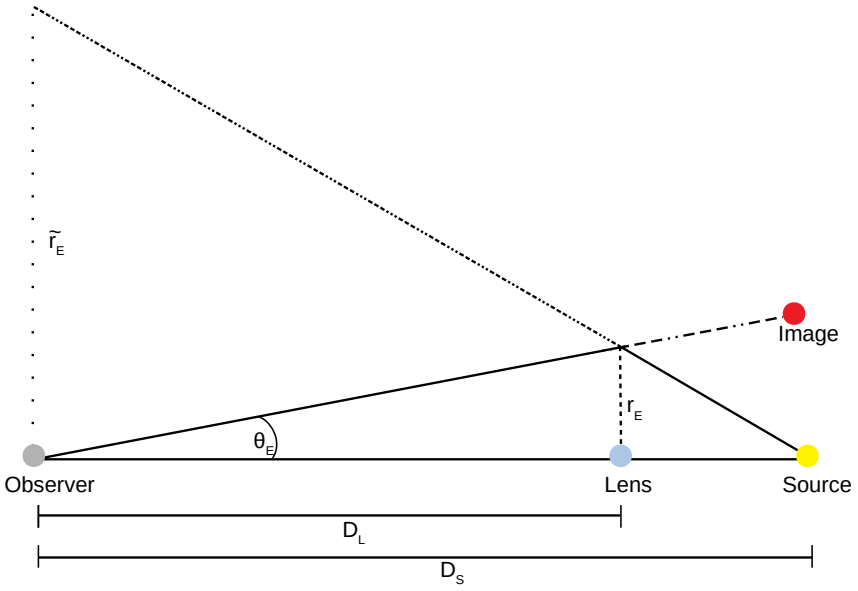

FIGURE 2.2: Representation of the geometry of a microlensing event.

the gravitational effect. If the light of the source passes at at distance r from an object of mass M, the light will be bent by an angle of:

$$\theta_E = \sqrt{\frac{4GM}{c^2}\frac{D_S - D_L}{D_S D_L}} \tag{2.2}$$

and therefore the Einstein radius is given as:

$$r_E = \theta_E D_L = \sqrt{\frac{4GM}{c^2}\frac{D_S - D_L}{D_S}} \tag{2.3}$$

with a magnification of:

$$A(u) = \frac{u^2 + 2}{u\sqrt{u^2 + 4}} \tag{2.4}$$

where u is the angular separation, in units of the Einstein radius, between the source and the lens. In the case of a perfect alignment, $u = 0$ and therefore the magnification is infinite, known as caustic. For caustic perturbations produced by a planetary companion, the planet will detected by the presence of a "bump" in the transient light curve of the background star, as seen in Fig. 2.3.

The advantage of this method is that is sensitive to detect Earth-sized planets and also is able to detect planets from other galaxies. But this event is temporary. This is because the observer, lens and source are all in relative motion and their angular separation with respect of another is dependent of time. Thus, a microlensing event is also a function of time. This is the main disadvantage of this method.

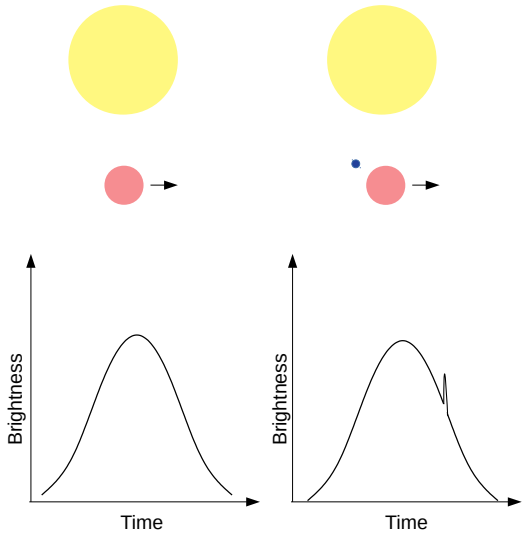

FIGURE 2.3: *(Left)* Acting as a lens, the foreground star magnifies the brightness of the background star. *(Right)* If the foreground star has a planetary companion, this will also act as a gravitational lens for a short period of time, producing a perturbation in the transient light curve of the background star.

2.1.3 Transit

When a planet passes in front of a star, it blocks part of the stellar light if the system is in the observer's line of sight. As the planet is orbiting around it host star, it will also hide behind it. This produces a periodic drop of flux in the stellar light curve, as seen in Fig 2.4. This means that the star has a companion, discovering in this way exoplanets through this method. The main observables of a this technique are the orbital period and the duration and depth of the transit. Planetary transit allows us to calculate the radius of the planet, as

$$\frac{\Delta F}{F} = \left(\frac{R_p}{R_s}\right)^2 \tag{2.5}$$

where F is the total stellar flux, R_s and R_p the radius of the star and the planet, respectively. This technique has been one of the best on the exoplanetary hunt, but as every technique, it has its disadvantages. As planets through this method can only be detected if the system is in the observer's line of sight, it limits enormously the exoplanet discoveries as not all planetary system are aligned following that geometry. The probability of a transit to be observable is given by:

$$\mathcal{P} \approx \frac{R_s}{a} \tag{2.6}$$

Therefore, in order to ensure its effectiveness, several surveys have been carried out, such as CoRoT (Barge et al., 2008), TESS (Ricker et al., 2009) and the Kepler mission (Borucki et al., 2010).

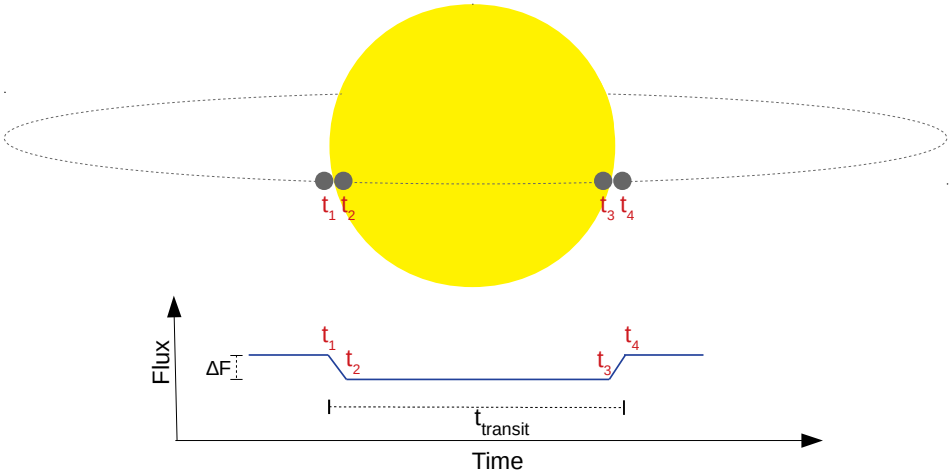

FIGURE 2.4: Diagram of the transit.

2.1.4 Astrometry

Astrometry measures the position and motion of a star with respect to the position of its background stars. This change in position is due to the gravitational influence of a companion. In a star-planet system, they both the center of mass. So by performing precise measurements of the position of the star, the planetary companion would be discovered.

The main advantage consists of being the only technique that allows to determine all the orbital parameters, including the planetary mass (if the stellar mass is calculated independently). Also, this technique is not affected by stellar activity (see Chapter 4), being less prone to false positives.

The astrometric motion θ of a planet of mass M_p that orbits in a circular orbit around its host star of mass M_s at a distance d with a semi major axis a is given by

$$\theta = \frac{M_p}{M_s}\frac{a}{d} \tag{2.7}$$

$$\theta'' = \left(\frac{M_p}{M_s}\right)\left(\frac{a}{AU}\right)\left(\frac{pc}{d}\right) \tag{2.8}$$

We note that astrometry is directy proportional to the mass of the planet and the semi major axis, being sensitive in detecting large mass planet in wide orbits. It is also sensitive to low-mass stars and planetaty system close to Earth. This latter is a disadvantage since this method cannot be used for system located far away. Also, it requires an extremely high precision, requiring high-quality instrumentation. As the turbulence in the atmosphere of the Earth can be a main difficult, space astrometry is more efficient.

The GAIA mission (Lindegren et al., 2008), which has been operating since 2014, is space mission designed to perform astrometric observations and is promising in

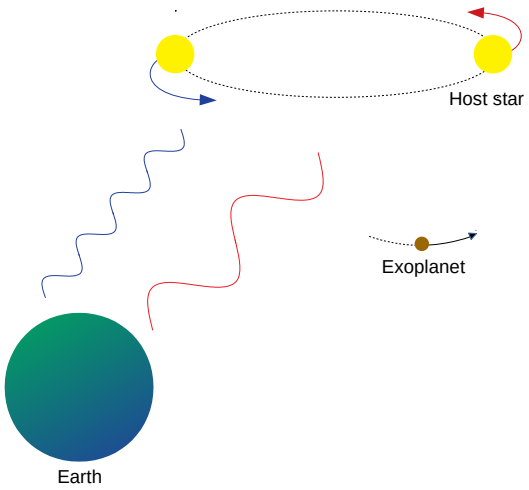

FIGURE 2.5: Radial velocity illustration described by the doppler shifted light of a star with a planetary companion.

the detection of exoplanets through this technique.

2.1.5 Radial Velocity

As the planetary system orbit their common center of mass, it is possible to detect a planet by measuring the stellar "wobble" produced by the gravitational influence of the planetary companion. This is produced by the Doppler effect, which is given by

$$\mathbf{k} \cdot \mathbf{v}_* = c\frac{\lambda_B - \lambda_0}{\lambda_0} \tag{2.9}$$

where $\mathbf{k}$ is the unit vector pointing to source from the observer in the rest frame of the observer, $\mathbf{v}_*$ is the source velocity, c is the speed of light in the vacuum, λ_0 is the wavelength of the emitted photon in the rest frame of the source, and λ_B is the wavelenght that would be measured by the observer considering barycentric correction.

The sign of this equation tell us how the object is moving with respect of the observer. A positive sign indicates that the object is moving away from us, producing an increase in wavelength and therefore there is redshift of the spectral lines. A negative sign implies that the object is moving towards us, causing a decrease in wavelength and thus producing a blueshift in the spectral lines. In this manner, if a star located in our line of sight presents periodic radial velocity (RV) variation, it implies that one or more planets are orbiting the host star, as seen in Fig 2.5.

From this RV variation, the orbital period, eccentricity and semi-major axis can be determined (see Section 3). With these observables, if the stellar mass is known or calculated independently, the minimum planetary mass ($M_p \sin i$) can be inferred as the orbital inclination cannot be determined.

The first planet detected with this method was Pegasi 51 b (Mayor et al., 1995), the first exoplanet found orbtiting a main sequence star. This planet corresponds to a Hot-Jupiter planet, as this method was biased to Jupiter-like planets since they are

easier to detect due to the greater gravitational influence on their host star. But as high precision instruments have been developed, with this technique it is now possible to detect Earth-mass planets around low-mass stars. Some high precision spectrograph are CORALIE (Queloz et al., 2000) installed at the 1.2-metre Leonhard Euler Telescope in La Silla Observatory with a precision of 3.05 ms^{-1}, HARPS (Mayor et al., 2003) mounted in the 3.6m telescope in La Silla Observatory with precision up to 0.97 ms^{-1}, ESPRESSO (Pepe et al., 2010) installed in VLT at Paranal observatory which precision goes up tp 0.1 ms^{-1}, CARMENES (Quirrenbach et al., 2010) mounted in 3.5m telescope at the Calar Alto Observatory reaching a precision of 1 ms^{-1}.

2.1.6 Methods sensitivities

As we have seen, each of the previously described technique has its detection tendency. We can see this in Fig. 2.6, which shows the planetary mass as a function of the semi-major axis. The RV and transit method tend to detect bigger mass planets in close orbits, whereas direct imaging, microlensing and astrometry tend to detect planets in wider orbits. From the data points, we observe that more planets have been discovered by the transit method, beating the RV method which was the most efficient technique to find planets. But as seen in Section 2.1.5, the RV method is being more sensitive to detect Earth-mass planet as new instruments are being developed, being promising in the planetary hunt. This latter method is described in detail in Chapter 3, but we first need to understand the mathematics and physics beyond the planetary orbits, which is shown in the following section.

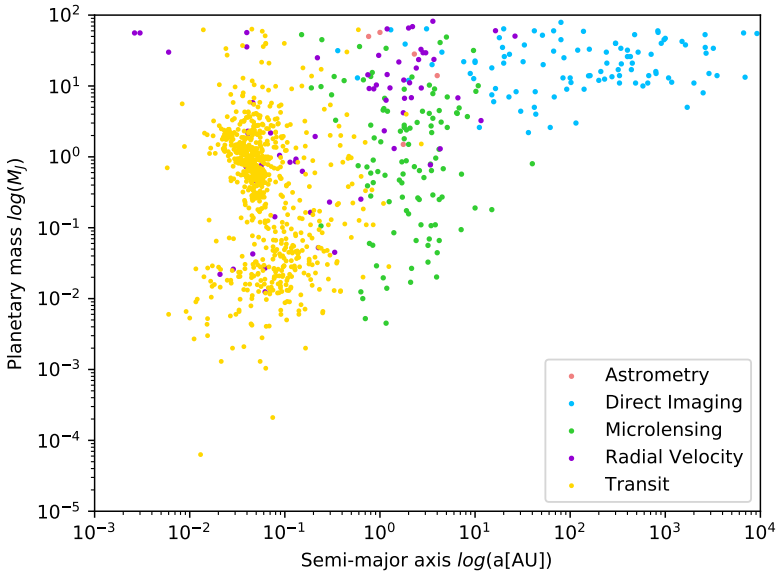

FIGURE 2.6: Planetary mass vs. semi-axis major for different detection methods.

2.2 Keplerian Orbits

Johannes Kepler took a big step in our understanding of planetary motion. His laws and implications allows us to model planetary systems. In this section, we will derive Kepler's laws of motion and solve the two-body problem and the Kepler problem. For the most part we follow Murray and Correia (2010).

2.2.1 Kepler's law of planetary motion

Kepler was delighted by the sky since his early years. This fascination led him to study the motion of the objects of our Solar System. From observational data obtained by Tycho Brahe, Kepler was able to derive in 1609 the first two laws of planetary motion, whereas the third law was deduced a decade later, in 1619. These laws state that:

1. Planets orbit the Sun in elliptical paths, where the Sun is located in one of the focus.
2. A radius vector joining the Sun to a planet sweeps outs equal areas in equal lengths of time.
3. The square of the orbital period of a planet is directly proportional to the cube of its semi-major axis.

Although Kepler derived these laws, he did not understand the physical phenomena behind it. Years later, in 1687, Kepler's laws motivated Isaac Newton, who showed that these laws where a natural consequence of an inverse square law of force acting between the Sun and a planet. In his *Principia* Newton proposed that:

1. A body will persist in its state of rest or uniform motion in a straight line unless a force acts upon it.
2. Force is equal to the change in momentum per change in time.
3. For every action, there is an equal and opposite reaction.

He also formulated the universal law of gravitation, revolutionizing science. In the context of the two-body problem, he was able to derived Kepler's laws of planetary motion. This is what we will carry out through these pages.
From Newton's universal law of gravitation, we have that

$$F = G\frac{m_1 m_2}{r^2} \tag{2.10}$$

where F is the magnitude of the force between masses m_1 and m_2 separated by a distance r and G is the universal gravitational constant (G= 6.67250 $\times 10^{-11}$ $\mathrm{Nm^2kg^{-2}}$). Considering a star with mass m_1 and position vector $\mathbf{r_1}$ and a planet

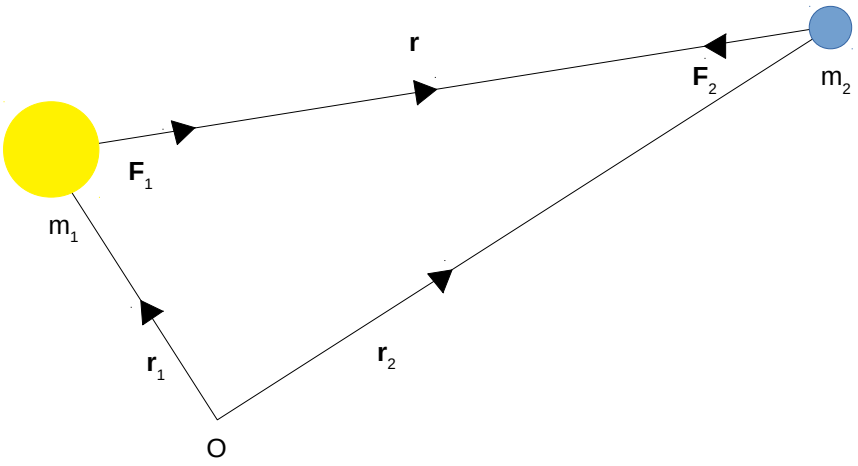

FIGURE 2.7: Diagram showing the forces (not to scale) acting on masses m_1 and m_2, with their postition vector $\mathbf{r_1}$ and $\mathbf{r_2}$ respectively.

with mass m_2 with a postion vector $\mathbf{r_2}$ with respect to an origin O (Figure 2.7), the gravitation forces acting on each other are given by

$$\mathbf{F_1} = m_1\ddot{\mathbf{r}}_\mathbf{1} = +G\frac{m_1 m_2}{r^3}\mathbf{r} \tag{2.11}$$

$$\mathbf{F_2} = m_2\ddot{\mathbf{r}}_\mathbf{2} = -G\frac{m_1 m_2}{r^3}\mathbf{r} \tag{2.12}$$

where $\mathbf{r} = \mathbf{r_2} - \mathbf{r_1}$ is the relative motion of the planet with respect to the star. Dividing by their respective masses we have, for $\mathbf{F_1}$

$$\begin{aligned} \frac{\cancel{m_1}\ddot{\mathbf{r}}_\mathbf{1}}{\cancel{m_1}} &= +G\frac{\cancel{m_1} m_2}{\cancel{m_1} r^3}\mathbf{r} \\ \Rightarrow \ddot{\mathbf{r}}_\mathbf{1} &= +G\frac{m_2}{r^3}\mathbf{r} \end{aligned} \tag{2.13}$$

and for $\mathbf{F_2}$

$$\begin{aligned} \frac{\cancel{m_2}\ddot{\mathbf{r}}_\mathbf{2}}{\cancel{m_2}} &= -G\frac{m_1 \mathbf{m_2}}{\cancel{m_2} r^3}\mathbf{r} \\ \Rightarrow \ddot{\mathbf{r}}_\mathbf{2} &= -G\frac{m_1}{r^3}\mathbf{r} \end{aligned} \tag{2.14}$$

From subtracting Eq. (2.13) from Eq. (2.14) we get

$$\begin{aligned} \ddot{\mathbf{r}}_\mathbf{2} - \ddot{\mathbf{r}}_\mathbf{1} &= -G\frac{m_1}{r^3}\mathbf{r} - G\frac{m_2}{r^3}\mathbf{r} \\ &= -G\frac{1}{r^3}\mathbf{r}(m_1 + m_2) \end{aligned}$$

Using $\ddot{\mathbf{r}} = \ddot{\mathbf{r}}_\mathbf{2} - \ddot{\mathbf{r}}_\mathbf{1}$ we obtain

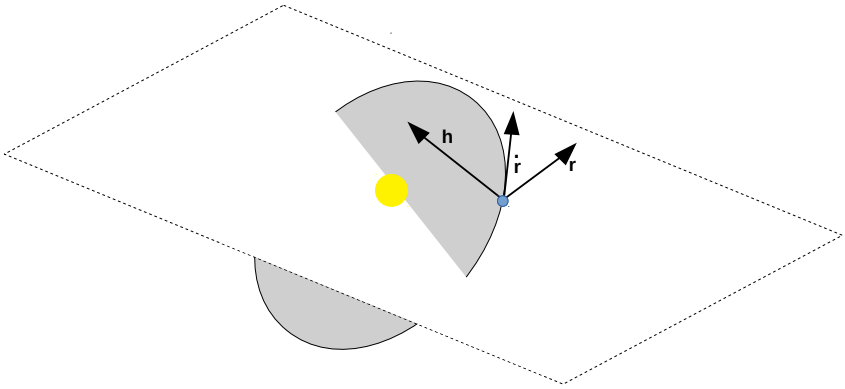

FIGURE 2.8: Illustration of the orbital plane (gray ellipse) and how the angular momentum vector **h** is always perpendicular to it.

$$\ddot{\mathbf{r}} + G\frac{m_1 + m_2}{r^3}\mathbf{r} = 0 \tag{2.15}$$

Since $\mathbf{r} \times \mathbf{r} = 0$, then $\mathbf{r} \times \ddot{\mathbf{r}} = 0$, which integrated yields to

$$\mathbf{r} \times \dot{\mathbf{r}} = \mathbf{h} \tag{2.16}$$

where **h** is a constant vector perpendicular to both **r** *and* $\ddot{\mathbf{r}}$. Thus, the motion of both bodies lies in a plane, known as the *orbit plane*, which is illustrated in Figure 2.8. Now we perform a transformation into polar coordinates.

The position vector **r** in cartesian coordinates is given by $\mathbf{r} = x\hat{\mathbf{i}} + y\hat{\mathbf{j}}$. Using the transformation

$$x = r\cos\theta$$
$$y = r\sin\theta$$

We have

$$\mathbf{r} = r\cos\theta\hat{\mathbf{i}} + r\sin\theta\hat{\mathbf{j}}$$

The unit vectors are defined as

$$\hat{\mathbf{r}} = \frac{\partial\mathbf{r}/\partial r}{|\partial\mathbf{r}/\partial r|} = \cos\theta\hat{\mathbf{i}} + \sin\theta\hat{\mathbf{j}}$$
$$\hat{\theta} = \frac{\partial\mathbf{r}/\partial\theta}{|\partial\mathbf{r}/\partial\theta|} = -\sin\theta\hat{\mathbf{i}} + \cos\theta\hat{\mathbf{j}}$$

Thus,

$$\begin{aligned}\mathbf{r} &= r\cos\theta\hat{\mathbf{i}} + r\sin\theta\hat{\mathbf{j}} \\ &= r(\cos\theta\hat{\mathbf{i}} + \sin\theta\hat{\mathbf{j}}) \\ &= r\hat{\mathbf{r}}\end{aligned}$$

And the velocity and acceleration vector are given by

$$\begin{aligned}\dot{\mathbf{r}} &= \dot{r}(\cos\theta\hat{\mathbf{i}} + \sin\theta\hat{\mathbf{j}}) + r\dot{\theta}(-\sin\theta\hat{\mathbf{i}} + \cos\theta\hat{\mathbf{j}}) \\ &= \dot{r}\hat{\mathbf{r}} + r\dot{\theta}\hat{\theta} \\ \ddot{\mathbf{r}} &= \ddot{r}(\cos\theta\hat{\mathbf{i}} + \sin\theta\hat{\mathbf{j}}) + \dot{r}\dot{\theta}(-\sin\theta\hat{\mathbf{i}} + \cos\theta\hat{\mathbf{j}}) + \dot{r}\dot{\theta}(-\sin\theta\hat{\mathbf{i}} + \cos\theta\hat{\mathbf{j}}) + r\ddot{\theta}(-\sin\theta\hat{\mathbf{i}} + \cos\theta\hat{\mathbf{j}}) \\ &\quad - r\dot{\theta}^2(\cos\theta\hat{\mathbf{i}} + \sin\theta\hat{\mathbf{j}}) \\ &= \ddot{r}\hat{\mathbf{r}} + 2\dot{r}\dot{\theta}\hat{\theta} + r\ddot{\theta}\hat{\theta} - r\dot{\theta}^2\hat{\mathbf{r}} \\ &= (\ddot{r} - r\dot{\theta}^2)\hat{\mathbf{r}} + (2\dot{r}\dot{\theta} + r\ddot{\theta})\hat{\theta} \\ &= (\ddot{r} - r\dot{\theta}^2)\hat{\mathbf{r}} + \left(\frac{1}{r}\frac{d}{dt}(r^2\dot{\theta})\right)\hat{\theta}\end{aligned}$$

Summarizing we have

$$\mathbf{r} = r\hat{\mathbf{r}} \tag{2.17}$$

$$\dot{\mathbf{r}} = \dot{r}\hat{\mathbf{r}} + r\dot{\theta}\hat{\theta} \tag{2.18}$$

$$\ddot{\mathbf{r}} = (\ddot{r} - r\dot{\theta}^2)\hat{\mathbf{r}} + \left(\frac{1}{r}\frac{d}{dt}(r^2\dot{\theta})\right)\hat{\theta} \tag{2.19}$$

Substituting the velocity vector onto Eq. (2.16) we get

$$\begin{aligned}(r\hat{\mathbf{r}}) \times (\dot{r}\hat{\mathbf{r}} + r\dot{\theta}\hat{\theta}) &= \mathbf{h} \\ r\hat{\mathbf{r}} \times r\dot{\theta}\hat{\theta} &= \mathbf{h} \\ r^2\dot{\theta}\hat{\mathbf{z}} &= \mathbf{h}\end{aligned}$$

where $\hat{\mathbf{z}}$ is a unit vector perpendicular to both $\hat{\mathbf{r}}$ and $\hat{\theta}$. The magnitude of this vector is therefore

$$h = r^2\dot{\theta} \tag{2.20}$$

which tell us that the quantity $r^2\dot{\theta}$ remains constant when the planet orbits the star. The area element swept out by the radius vector of the star and planet is given by

$$dA = \int_0^r r dr d\theta = \frac{1}{2} r^2 d\theta$$

Hence

$$\dot{A} = \frac{1}{2} r^2 \dot{\theta} \tag{2.21}$$

$$= \frac{1}{2} h \tag{2.22}$$

which means that

$$\boxed{\dot{A} = \text{constant}} \tag{2.23}$$

This is equivalent to the **second law** of Kepler of planetary motion, stating that the line between the star and the planet sweeps equal areas in equal times.
Recalling Eq. (2.15) and substituting the $\hat{\mathbf{r}}$ components of Eq. (2.17) and Eq. (2.19) yields to

$$\ddot{r} - r\dot{\theta}^2 = -\frac{G(m_1 + m_2)}{r^2} \tag{2.24}$$

But we can write r as a function of θ. Using the chain rule we obtain

$$\dot{r} = \frac{d}{dt}\Big(r(\theta(t))\Big) = \frac{dr}{d\theta}\frac{d\theta}{dt} = \frac{dr}{d\theta}\dot{\theta}$$

Making the substitution $u = 1/r$, we have that $du = -\frac{1}{r^2} dr$, which implies that $dr = -r^2 du$, thus

$$\dot{r} = -r^2 \frac{du}{d\theta}\dot{\theta} = -\frac{1}{u^2}\frac{du}{d\theta}\dot{\theta}$$

But from equation 2.20 we have that $\dot{\theta} = \frac{h}{r^2}$, thus

$$\dot{r} = -h\frac{du}{d\theta}$$

And in this manner $\ddot{r}$ is given by

$$\ddot{r} = -h\frac{d^2u}{d\theta^2}\dot{\theta}$$

$$= -h^2u^2\frac{d^2u}{d\theta^2}$$

Replacing this result into equation 2.24 and using again equation 2.20 we have

$$
\begin{aligned}
-h^2u^2\frac{d^2u}{d\theta^2} - r\frac{h^2}{r^4} &= -G(m_1+m_1)u^2 \\
\frac{d^2u}{d\theta^2} + \frac{1}{r^3u^2} &= \frac{G(m_1+m_2)}{h^2} \\
\frac{d^2u}{d\theta^2} + \frac{u^3}{u^2} &= \frac{G(m_1+m_2)}{h^2} \\
\frac{d^2u}{d\theta^2} + u &= \frac{G(m_1+m_2)}{h^2}
\end{aligned}
$$

This second order linear differential equation it is known as *Binet's equation*, which general solution is given by

$$u = \frac{G(m_1+m_2)}{h^2}[1 + e\cos(\theta - \omega)]$$

where e, which corresponds to an amplitude, and ω, which corresponds to a phase, are two constants of integration.

Substituting back for r we get

$$r = \frac{h^2}{G(m_1+m_2)} \cdot \frac{1}{[1 + e\cos(\theta - \omega)]}$$

Making

$$p = \frac{h^2}{G(m_1+m_2)} \tag{2.25}$$

We get

$$r = \frac{p}{1 + e\cos(\theta - \omega)} \tag{2.26}$$

This corresponds to the general solution in polar coordinates of a conic. For a given conic, the values of e and p are shown in the following table.

conic	e	p
circle	= 0	= a
ellipse	$0 < e < 1$	$= a(1-e^2)$
parabola	= 1	$= 2q$
hyperbola	$e > 1$	$= a(e^2-1)$

where q is the shortest distance to the central mass and where a is called the *semi-major axis*. Considering an elliptical motion and substituting the value of p into 2.27 we have

$$\boxed{r = \frac{a(1-e^2)}{1 + e\cos(\theta - \omega)}} \tag{2.27}$$

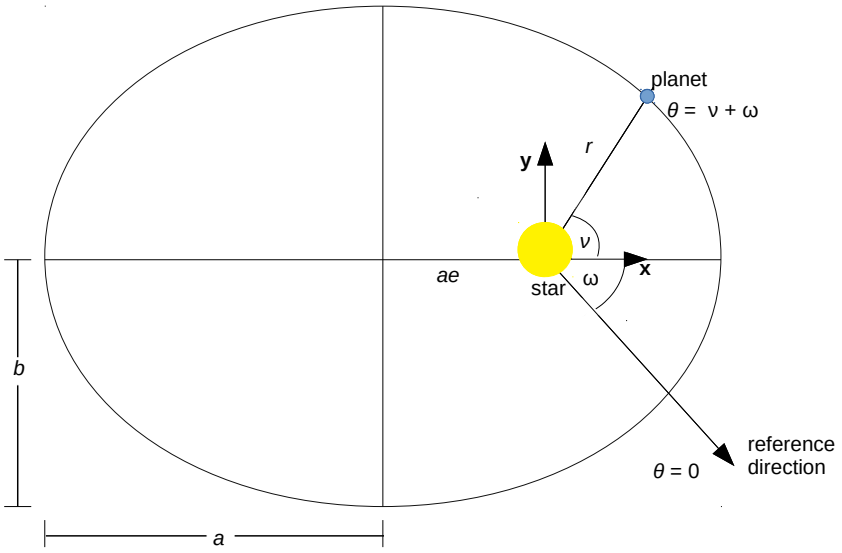

FIGURE 2.9: Representation of the geometry of the ellipse.

This represents the **first law** of Kepler of planetary motion, stating that the orbit of a planet around the stars is an ellipse, in which the star is located in one of the focus. In Figure 2.9 the geometry and parts of the ellipse are shown. The angle θ is called *true longitude* and the angle ω is knows as the *longitude of periastron*, where the *periastron* is the closest star-planet distance r, while the *apastron* is the maximun distance. Thus, the longitude of periastron is the angular location of the periastron with respect to the reference direction.

Defining the angle $\nu = \theta - \omega$, known as *true anomaly*, then

$$r = \frac{a(1-e^2)}{1+e\cos\nu} \tag{2.28}$$

Now we just need to derive the third law of Kepler. We saw that the orbital trajectory of a planet around a star is an ellipse, with an area of $A = \pi ab$ (where b is the *semi-minor axis* of the ellipse), which is traveled by the planet in a time P. But from Eq. (2.22) we have that

$$\dot{A} = \frac{1}{2}h$$
$$\Rightarrow A = \frac{1}{2}hP$$

Thus, we have the following equality

$$\frac{1}{2}hP = \pi ab$$
$$P = \frac{2\pi ab}{h}$$
$$P^2 = 4\pi^2 \cdot \left(\frac{ab}{h}\right)^2$$

But we know from Eq. (2.25) that

$$h^2 = p \cdot G(m_1 + m_2)$$

Then, we have that

$$P^2 = 4\pi^2 \frac{a^2 b^2}{p \cdot G(m_1 + m_2)}$$

But the quantities a and b are related by

$$b^2 = a^2(1 - e^2) \tag{2.29}$$

Replacing this and knowing that $p = a(1 - e^2)$, we obtain

$$P^2 = \frac{4\pi^2}{G(m_1 + m_2)} \frac{a^2 \cdot a^2(1 - e^2)}{a(1 - e^2)}$$

$$\boxed{P^2 = \frac{4\pi^2}{G(m_1 + m_2)} a^3} \tag{2.30}$$

which corresponds to the **third law** of Kepler of planetary motion.

2.2.2 Solution of the two-body problem

So far, we have derived the three laws of kepler of planetary motion. Since the two-body problem consists of calculating the trajectory of two bodies of known masses and initial velocities, we will now find the relation between the velocity of the planet v with the distance r.

Taking the scalar product of $\dot{\mathbf{r}}$ with Eq. (2.15) yields to

$$\dot{\mathbf{r}} \cdot \ddot{\mathbf{r}} + G(m_1 + m_2)\dot{\mathbf{r}} \cdot \mathbf{r} = 0$$

Replacing Eq. (2.17) and Eq. (2.19) we get

$$\dot{\mathbf{r}} \cdot \ddot{\mathbf{r}} + G(m_1 + m_2)(\dot{r}\hat{\mathbf{r}} \cdot r\hat{\mathbf{r}}) = 0$$
$$\dot{\mathbf{r}} \cdot \ddot{\mathbf{r}} + G(m_1 + m_2)\frac{\dot{r}}{r^2} = 0$$

Integrating this yields to

$$\frac{1}{2}\dot{\mathbf{r}} \cdot \dot{\mathbf{r}} - \frac{G(m_1 + m_2)}{r} = C \tag{2.31}$$

where C is a constant of the motion. Since $\nu = \theta - \omega$, then

$$\theta = \nu + \omega$$
$$\Rightarrow \dot{\theta} = \frac{d(\nu + \omega)}{dt}$$

And since ω is fixed,

$$\dot{\theta} = \dot{\nu} \tag{2.32}$$

Replacing this into Eq. (2.18), we calculate the scalar product of $\dot{\mathbf{r}} \cdot \dot{\mathbf{r}}$

$$\dot{\mathbf{r}} \cdot \dot{\mathbf{r}} = \dot{r}^2 + r^2\dot{\theta}^2 \tag{2.33}$$
$$= \dot{r}^2 + r^2\dot{\nu}^2 \tag{2.34}$$

Now we need to find the values of $\dot{r}^2$ and $r^2\dot{\nu}^2$. First, we differentiate Eq. (2.28)

$$\dot{r} = \frac{a(1 - e^2)}{(1 + e\cos\nu)}\frac{e\sin\nu}{(1 + e\cos\nu)}\dot{\nu}$$
$$= r\dot{\nu}\frac{e\sin\nu}{(1 + e\cos\nu)} \tag{2.35}$$

But from Eq. (2.20) and Eq. (2.32) we have that

$$h = r^2\dot{\theta} = r^2\dot{\nu} \tag{2.36}$$

Defining the *mean motion* of the planet's motion as

$$n = \frac{2\pi}{P}$$

Then from the third law of Kepler we have that

$$\frac{\cancel{4\pi^2}}{n^2} = \frac{\cancel{4\pi^2}}{G(m_1+m_2)}a^3 \tag{2.37}$$

$$\Rightarrow G(m_1+m_2) = n^2a^3 \tag{2.38}$$

And from Eq. (2.25) we have that

$$h = \sqrt{a(1-e^2)G(m_1+m_2)} \tag{2.39}$$

$$= \sqrt{a(1-e^2)n^2a^3} \tag{2.40}$$

$$= na^2\sqrt{1-e^2} \tag{2.41}$$

Replacing this into Eq. (2.36), yields to

$$h = r^2\dot{\nu} = na^2\sqrt{1-e^2}$$

$$\Rightarrow r\dot{\nu} = \frac{na^2\sqrt{1-e^2}}{r}$$

Replacing Eq. (2.28)

$$r\dot{\nu} = na\cancel{^2}\sqrt{1-e^2}\cdot\frac{(1+e\cos\nu)}{\cancel{a}(1-e^2)}$$

$$= \frac{na}{\sqrt{1-e^2}}(1+e\cos\nu) \tag{2.42}$$

Replacing this into Eq. (2.35) we get

$$\dot{r} = \frac{na}{\sqrt{1-e^2}}\cdot\cancel{(1+e\cos\nu)}\cdot\frac{e\sin\nu}{\cancel{(1+e\cos\nu)}} \tag{2.43}$$

$$= \frac{na}{\sqrt{1-e^2}}\cdot e\sin\nu \tag{2.44}$$

Now we can replace Eq. (2.44) and Eq. (2.42) into Eq. (2.34)

$$\dot{\mathbf{r}}\cdot\dot{\mathbf{r}} = \dot{r}^2 + r^2\dot{\nu}^2$$

$$= \left(\frac{na}{\sqrt{1-e^2}}\cdot e\sin\nu\right)^2 + \left(\frac{na}{\sqrt{1-e^2}}(1+e\cos\nu)\right)^2$$

$$= \frac{n^2a^2}{(1-e^2)}[e^2\sin^2\nu + (1+e\cos\nu)^2]$$

$$
\begin{aligned}
&= \frac{n^2a^2}{(1-e^2)}[e^2\sin^2\nu + 1 + 2e\cos\nu + e^2\cos^2\nu] \\
&= \frac{n^2a^2}{(1-e^2)}[1 + 2e\cos\nu + e^2(\sin^2\nu + \cos^2\nu)] \\
&= \frac{n^2a^2}{(1-e^2)}[1 + 2e\cos\nu + e^2] \qquad (2.45)
\end{aligned}
$$

But from Eq. (2.28) we have that

$$e\cos\nu = \frac{a(1-e^2)}{r} - 1 \qquad (2.46)$$

Thus,

$$
\begin{aligned}
\dot{\mathbf{r}}\cdot\dot{\mathbf{r}} &= \frac{n^2a^2}{(1-e^2)}(1 + 2\left[\frac{a(1-e^2)}{r} - 1\right] + e^2) \\
&= \frac{n^2a^2}{(1-e^2)}\left[\frac{2a(1-e^2)}{r} - 1 + e^2\right] \\
&= \frac{n^2a^2}{(1-e^2)}\left[\frac{2a(1-e^2)}{r} - (1-e^2)\right] \\
&= n^2a^2\left[\frac{2a}{r} - 1\right] \\
&= n^2a^2\cdot a\left[\frac{2}{r} - \frac{1}{a}\right] \\
&= n^2a^3\left[\frac{2}{r} - \frac{1}{a}\right] \qquad (2.47)
\end{aligned}
$$

And replacing Eq. (2.38) we obtain

$$v^2 = \dot{\mathbf{r}}\cdot\dot{\mathbf{r}} = G(m_1+m_2)\left[\frac{2}{r} - \frac{1}{a}\right] \qquad (2.48)$$

where $v^2 = \dot{\mathbf{r}}\cdot\dot{\mathbf{r}}$ is the square of the velocity. This relation shows the dependence of v on r. Comparing Eq. (2.31) with Eq. (2.48) we find that the energy constant is given by

$$C = -\frac{G(m_1+m_2)}{2a} \qquad (2.49)$$

2.2.3 Solution to the Kepler problem

Now we must find r as a function of time. This is often known as the *Kepler problem*. To find a relation between $\dot{r}$ and r, we recall Eq. (2.34) and Eq. (2.47)

$$\begin{aligned}\dot{\mathbf{r}} \cdot \dot{\mathbf{r}} &= \dot{r}^2 + r^2\dot{\nu}^2 \\ &= n^2a^3\left[\frac{2}{r} - \frac{1}{a}\right]\end{aligned}$$

From here we have that

$$\begin{aligned}\dot{r}^2 + r^2\dot{\nu}^2 &= n^2a^3\left[\frac{2}{r} - \frac{1}{a}\right] \\ \Rightarrow \dot{r}^2 &= n^2a^3\left[\frac{2}{r} - \frac{1}{a}\right] - r^2\dot{\nu}^2\end{aligned}$$

Replacing Eq. (2.42) and Eq. (2.46) we obtain

$$\begin{aligned}\dot{r}^2 &= n^2a^3\left[\frac{2}{r} - \frac{1}{a}\right] - \frac{n^2a^2}{1-e^2}(1 + e\cos\nu)^2 \\ &= n^2a^3\left[\frac{2}{r} - \frac{1}{a}\right] - \frac{n^2a^2}{1-e^2}\left[\frac{a(1-e^2)}{r}\right]^2 \\ &= n^2a^3\left[\frac{2}{r} - \frac{1}{a}\right] - \frac{n^2a^4(1-e^2)}{r^2}\end{aligned} \tag{2.50}$$

Which means that

$$\begin{aligned}\dot{r} &= \sqrt{n^2a^3\left[\frac{2}{r} - \frac{1}{a}\right] - \frac{n^2a^4(1-e^2)}{r^2}} \\ &= \sqrt{\frac{2n^2a^3}{r} - n^2a^2 - \frac{n^2a^4}{r^2} + \frac{n^2a^4e^2}{r^2}} \\ &= \sqrt{\frac{n^2a^2}{r^2}\left[2ra - r^2 - a^2 + a^2e^2\right]} \\ &= \frac{na}{r}\sqrt{a^2e^2 - (r-a)^2}\end{aligned} \tag{2.51}$$

Introducing a new variable E, called the *eccentric anomaly*, as

$$r = a(1 - e\cos E) \tag{2.52}$$

Then

$$\dot{r} = ae \sin E \dot{E} \tag{2.53}$$

The differential equation transforms to

$$\dot{E} = \frac{n}{1 - e \cos E} \tag{2.54}$$

Where the solution can be solved by considering a constant of integration T_0 and use the boundary condition $E = 0$ when $t = T_0$. Therefore, the solution is given by

$$n(t - t_0) = E - e \sin E \tag{2.55}$$

Now we define a new quantity as the *mean anomaly* M, expressed as

$$M = n(t - T_0) \tag{2.56}$$

where T_0 is known as the *time of periastron passage*. When $t = T_0$ or $t = T_0 + P$ (periapse passage), then $M = \nu = 0$. When $t = T_0 + P/2$ then $M = \nu = \pi$.
The mean anomaly can be written as

$$M = E - -e \sin E \tag{2.57}$$

Which is known as Kepler's equation. Solving this equation allows to find the orbital position at a given time. The following steps can be done in order to characterize and orbit.

1. Find M (Eq. 2.56)
2. Find E from Kepler's equation (Eq. 2.57)
3. Find r (Eq. 2.52)
4. Find ν (Eq. 2.28)

As we will see in the following Chapter, these parameters are essential in the RV method. They are used to solve the radial velocity equation, which allows to perform fits over the RV data and therefore obtain orbital parameters from planetary systems.

Chapter 3

The Radial Velocity Method

As this thesis is based on the RV method, we will focus on it for a better understanding. Even thought we mentioned the main basis of this technique in Section 2.1.5, here we will review in detail the orbital elements and parameters, the RV equation, its signal analysis and how to obtain RV measurements from stellar spectra.

3.1 Orbital elements and parameters

As seen in Fig. 3.1, a Keplerian orbit in 3-dimensions has its orbital elements that defines its geometry. These elements are the following. The inclination i is the angle between the sky plane (perpendicular to the line-of-sight toward the star) and orbital plane. The ascending node Υ corresponds to the point where the star recedes from the observer when it crosses the sky plane. The stellar periastron p defines the stellar closest approach to the center of mass CM of the system. The position vector $\vec{r}$ illustrates the connection of the centre of mass and the position of the star with respect of time. The true anomaly ν indicates the angle between the periastron and $\vec{r}$. As the vector $\vec{r}$ changes in time, this angle is also time dependent. The line of nodes illustrates the orbital and sky plane intersection through the centre of mass. The angle of the ascending node Ω defines the orientation of the node line. The longitude of periastron ω is the angle between the periastron and the line of nodes.
In order to define completely the orbit, we need to describe the orbital parameters. These seven parameters are the following. The orbital period P, which is the time the planet takes to orbit its host star. The eccentricity e measures how much the ellipse deviates from being circular, with values going from 0 to 1 (the eccentricity of a circle is zero). The semi-major axis a corresponds to the orbital distance. The passage of periastron T_0 is the time at which the orbit of a planet goes through its periastron. And the orbital elements described above: the longitude of periastron ω, the longitude of the ascending node Ω and the orbital inclination i.

All of these elements describes the shape, size and orientation of the orbit, allowing us to describe the physics of the orbiting bodies.

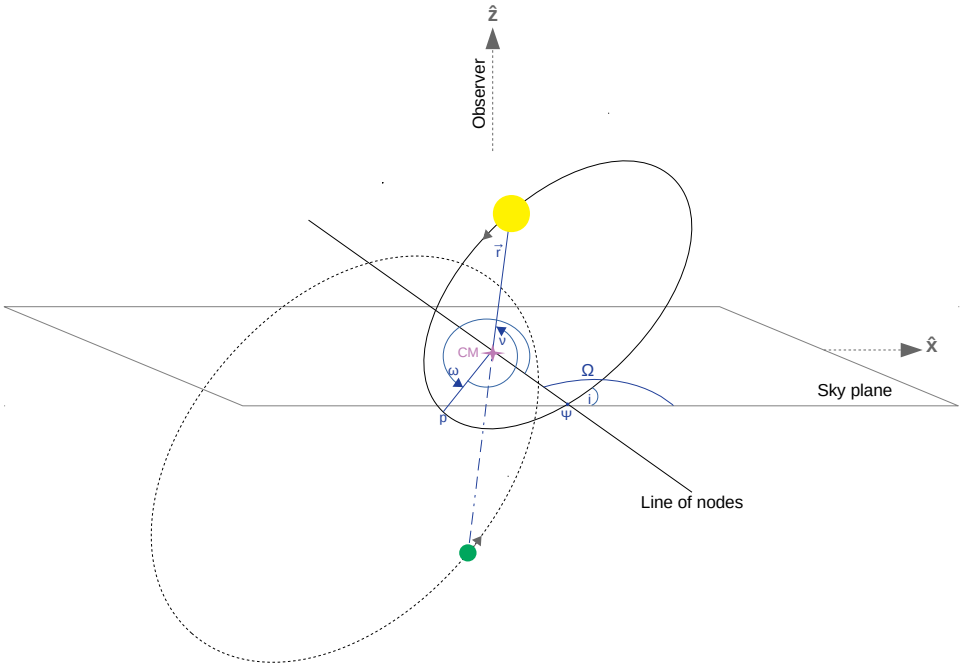

FIGURE 3.1: Schematized representation of a Keplerian orbit in 3-dimensions.

3.2 The radial velocity curve

The mathematical details of this part is described in Section 2.2. As we know from the two-body problem, each body orbits in an elliptical orbit around the common center of mass, which is the focus of the ellipse. For a star-planet system each of their semi-major axis are given by

$$a_s = \frac{M_p}{M_p + M_s} \cdot a \tag{3.1}$$

$$a_p = \frac{M_s}{M_p + M_s} \cdot a \tag{3.2}$$

where M_p is the mass of the planet and M_s is the stellar mass. From the first law of Kepler of planetary motion, we know that the ellipse is described in polar coordinates by (Eq. 2.27)

$$r = \frac{a(1-e^2)}{1 + e\cos\nu}$$

From trigonometry (see Fig. 3.1), we know that the $\hat{z}$ coordinate (the observer's line of sight) of the star is given by

$$z = r(t)\cos\left(\nu(t) + \omega\right)\sin i \tag{3.3}$$

Deriving z with respect of time we get

$$v_r = \frac{dz}{dt} = \frac{dr}{dt}\sin(\nu+\omega)\sin i + r\frac{d\nu}{dt}\cos(\nu+\omega)\sin i \tag{3.4}$$

From Eq. (2.42) we have that

$$\begin{aligned} r\frac{d\nu}{dt} &= \frac{na_s(1+e\cos\nu)}{\sqrt{1-e^2}} \\ &= \frac{2\pi a_s(1+e\cos\nu)}{P\sqrt{1-e^2}} \end{aligned} \tag{3.5}$$

as $n = 2\pi/P$. Now, from the ellipse equation we have that

$$\begin{aligned} \frac{dr}{dt} &= \frac{a(1-e^2)e\sin\nu}{(1+e\cos\nu)^2}\frac{d\nu}{dt} \\ &= \frac{e\sin\nu}{(1+e\cos\nu)}r\frac{d\nu}{dt} \\ &= \frac{2\pi a_s e\sin\nu}{P\sqrt{1-e^2}} \end{aligned} \tag{3.6}$$

Thus, replacing Eq. (3.6) and Eq. (3.5) into Eq. (3.4) we get

$$\begin{aligned} v_r &= \frac{2\pi a_s}{P\sqrt{1-e^2}}\sin i\Big[e\sin\nu\sin(\nu+w) + (1+e\cos\nu)\cos(\nu+w)\Big] \\ &= \frac{2\pi a_s}{P\sqrt{1-e^2}}\sin i\Big[e\sin\nu\big(\sin\nu\cos w + \cos\nu\sin w\big) + (1+e\cos\nu)\big(\cos\nu\cos w - \sin\nu\sin w\big)\Big] \\ &= \frac{2\pi a_s}{P\sqrt{1-e^2}}\sin i\Big[e\cos w + \cos\nu\cos w - \sin\nu\sin w\Big] \\ &= \frac{2\pi a_s}{P\sqrt{1-e^2}}\sin i\Big[e\cos w + \cos(\nu+w)\Big] \end{aligned} \tag{3.7}$$

Now, replacing Eq. (3.1) in the latter expression we obtain

$$v_r = \frac{2\pi a\sin i}{P\sqrt{1-e^2}}\frac{M_p}{M_s+M_p}\Big[e\cos w + \cos(\nu+w)\Big]$$

And replacing the semi-major axis a from Kepler's third law (Eq. 2.30) we have

$$v_r = \left(\frac{2\pi G}{P}\right)^{1/3}\frac{1}{\sqrt{1-e^2}}\frac{M_p\sin i}{(M_s+M_p)^{2/3}}\Big[e\cos w + \cos(\nu+w)\Big] \tag{3.8}$$

Defining the radial velocity semi-amplitude as

$$K = \left(\frac{2\pi G}{P}\right)^{1/3}\frac{1}{\sqrt{1-e^2}}\frac{M_p\sin i}{(M_p+M_s)^{2/3}} \tag{3.9}$$

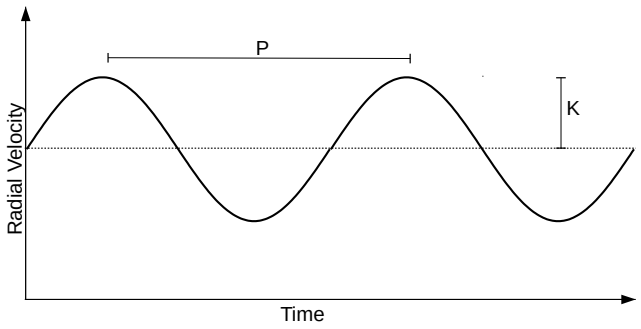

FIGURE 3.2: Illustration of an hypothetical RV curve indicating the parameters P and K.

And adding the stellar systemic velocity γ we finally obtain the radial velocity curve given by

$$\boxed{v_r = K\big[\cos(\nu+\omega)+e\cos(\omega)\big]+\gamma} \tag{3.10}$$

The value of K gives us the amplitude of the signal while the terms in the brackets are responsible for the shape of the curve. By making a fit to the data using the RV equation we are performing a Keplerian fit. This allows us to derive planetary parameters from the RV data. As seen in Fig. 3.2 we can visualize the parameters P and K on the velocity curve, and in Fig. 3.3 we see how the shape of the RV curve depends on e and ω.

Since the parameters described in the RV curve are not lineal, they cannot be adjust analytically and they must be found through an algorithmic search. One way to do this is to analyze the periodograms to identify the periods of the potential planets, where all the highest significant peaks can be used as starting guesses for the fitting algorithm. The Generalized Lomb-Scargle periodogram (GLS; Zechmeister and Kürster, 2009) is an efficient tool to analyze periodic and stable RV signals in order to identify possible planets. This algorithm is described in the following section.

3.3 Generalized Lomb-Scargle periodogram

To understand the GLS periodogram we first need to be familiarized with the Lomb-Scargle periodogram (Lomb, 1976; Scargle, 1982), which allows to detect periodicities of uneven time series data. This periodogram is based on the following equation (Barning, 1963; Lomb, 1976; Scargle, 1982)

$$\hat{p}(\omega) = \frac{1}{\hat{Y}Y}\left[\frac{\hat{Y}C_{\hat{\tau}}^2}{\hat{C}C_{\hat{\tau}}}+\frac{\hat{Y}S_{\hat{\tau}}^2}{\hat{S}S_{\hat{\tau}}}\right] \tag{3.11}$$

$$= \frac{1}{\sum_i y_i^2}\left[\frac{[\sum_i y_i \cos w(t_i-\hat{\tau})]^2}{\sum_i \cos^2 w(t_i-\hat{\tau})}+\frac{[\sum_i y_i \sin w(t_i-\hat{\tau})]^2}{\sum_i \sin^2 w(t_i-\hat{\tau})}\right] \tag{3.12}$$

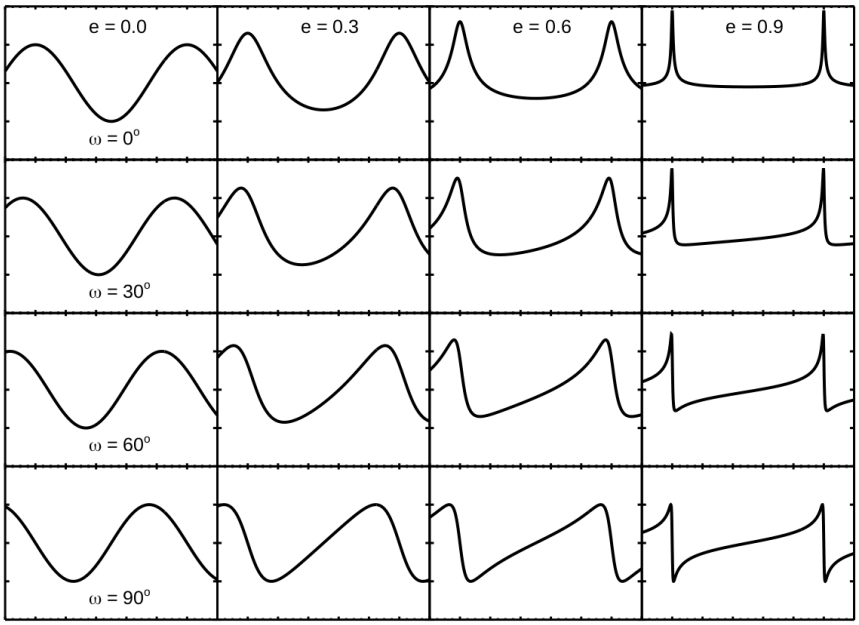

FIGURE 3.3: The effects that different values of e and ω have on RV curves. These RV curves have the same value of K, P and T_0. Each column shows fixed values of e and each row shows fixed values of ω (taken from Fig. 3 - Wright and Gaudi, 2013).

where τ is derived from the following expression

$$\tan 2w\tau = \frac{\sum_i \sin 2wt_i}{\sum_i \cos 2wt_i} \tag{3.13}$$

The disadvantage that it has is that it does not take into account measurement errors and assumes that the mean of the data is the same to the mean of the fitted periodic function.

In order to take into consideration these deficiencies, an incorporation of modifications was performed by Zechmeister and Kürster (2009), introducing the generalised Lomb-Scargle (GLS) periodogram. This method considers an offset in the periodic sine wave ($y = a\cos\omega t + b\sin\omega t + c$) and also considers measurement errors. The equation describing the power of a frequency in the GLS periodogram is given by

$$p(\omega) = \frac{1}{YY}\left[\frac{YC_{\hat{\tau}}^2}{CC_{\hat{\tau}}} + \frac{YS_{\tau}^2}{SS_{\tau}}\right] \tag{3.14}$$

$$= \frac{1}{\sum_i w_i(y_i - \bar{y})^2}\left[\frac{[\sum_i w_i(y_i - \bar{y})\cos w(t_i - \tau)]^2}{\sum_i w_i^2 \cos^2 w(t_i - \tau)} + \frac{[\sum_i w_i(y_i - \bar{y})\sin w(t_i - \tau)]^2}{\sum_i w_i^2 \sin^2 w(t_i - \tau)}\right] \tag{3.15}$$

with

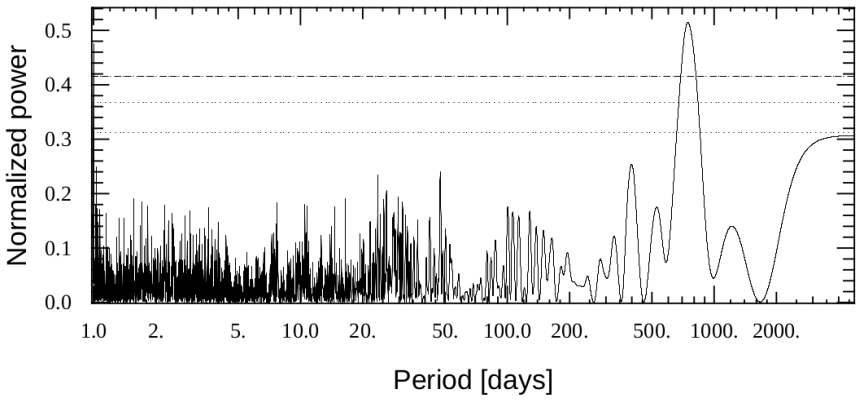

FIGURE 3.4: GLS periodogram of HD 85390 derived from RV observations. The horizontal lines indicate the power required for a FAP of 0.1, 1 and 10% from top to bottom (taken from Fig. 1 - Mordasini et al., 2011).

$$\tan 2w\tau = \frac{\sum w_i \sin 2wt_i - 2\sum w_i \cos wt_i \sum w_i \sin wt_i}{\sum w_i \cos 2wt_i - [(\sum w_i \cos wt_i)^2 - (\sum w_i \sin wt_i)^2]} \tag{3.16}$$

We note that this equation has the same form as the Lomb-Scargle periodogram equation (Eq. 3.12), but in the GLS periodgoram the weights of the errors w_i are considered. This generalization of the Lomb-Scargle periodogram is more efficient since it provides more precise frequencies, determining better the spectral intensity, in addition to not being susceptible to aliases.

With this tool we can look for signals of potential planets and perform Keplerian fits in order to obtain orbital parameters of planetary system. As we are aware of its efficiency, we performed GLS periodogram analysis in this thesis.

False alarm probability

In order to evaluate how significant a peak is in the GLS periodogram, the following things need to be considered. Noise can generate a higher peak than the data, which is known as false alarm probability (FAP). If in the data there is a periodic signal which is known, it is important to know the value of the FAP in that frequency. The FAP for a peak of a certain power is given by

$$\text{FAP} = 1 - [1 - e^{-z}]^M \tag{3.17}$$

where z is the power of the peak in the GLS periodogram and M is the number of independent frequencies. In order to consider a signal to be significant its confidence level should be at a level of FAP $\leq 1\%$. In Fig. 3.4 we show an example of a GLS periodogram of RV data where the FAP levels are indicated. A significant signal is found near 800 days, which could be a promising planetary companion.

Another possibility to access M and the FAP are Monte Carlo or bootstrap simulations in order to determine how often a certain power level is exceeded just by chance (Zechmeister and Kürster, 2009).

3.4 Deriving radial velocities from stellar spectra

3.4.1 Cross-correlation function

The radial velocity from a star are obtained through their spectra. The absorption lines are shifted due to the Doppler effect by

$$\lambda = \lambda_0 \left(1 + \frac{vr}{c}\right) \tag{3.18}$$

where λ is the wavelength measured by the observer (considering barycentric correction), λ_0 is the wavelength emitted in the rest frame of the star, c is the speed of light and vr is the radial velocity.

So measuring this spectrum shift can give us the radial velocity of the star. In practice, this is done by cross-correlating. Once the stellar spectrum has been normalized and correlated with respect of template mask, the lines of the spectrum are combined into one single mean line profile, known as the cross-correlation function (CCF). A Gaussian fit is performed to the peak of the CCF in order to determine the best spectral shift. Therefore, the radial velocity of the star can be obtained when measuring the centre of the Gaussian fit over the CCF, as seen in Fig. 3.5. This technique is widely used and has been incorporated into the pipelines of HARPS and SOPHIE.

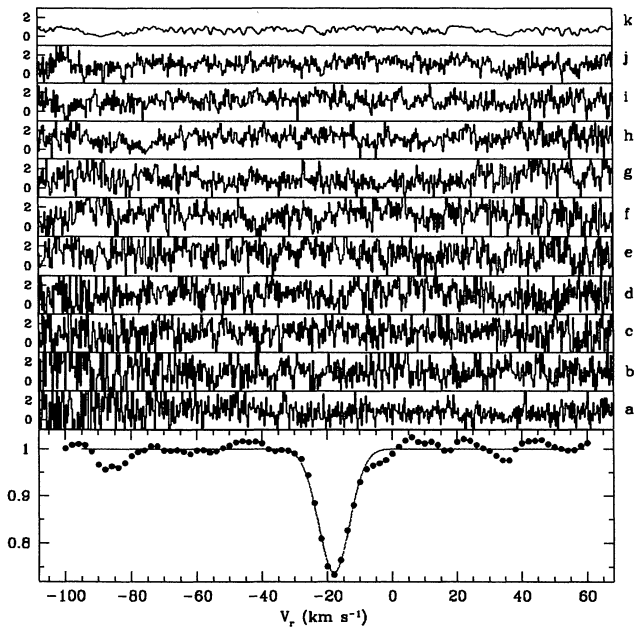

FIGURE 3.5: Representation of the CCF of a ten order spectrum with S/N $\sim$ 1 (taken from Fig. 2 - Queloz, 1995).

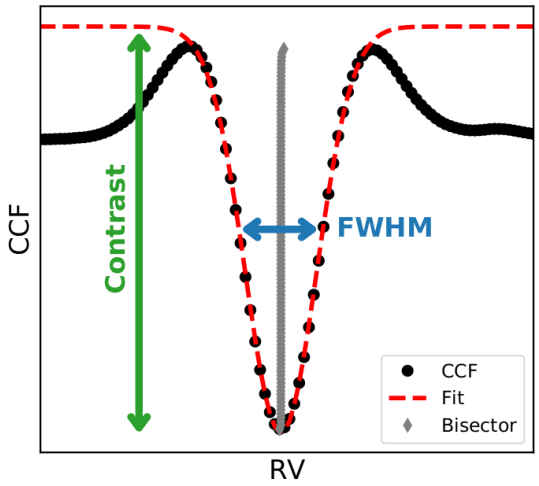

FIGURE 3.6: Sketch of a CCF (black dots) with the best Gaussian fit (red dashed lines). The parameters FHWM, BIS and contrast are also illustrated (taken from Fig. 4 - Lafarga et al., 2020).

The CCF is derived from

$$C(\epsilon) = \frac{R(\epsilon)}{R(\infty)} \tag{3.19}$$

$$R(\epsilon) = \int_{-\infty}^{+\infty} S(v)M(v-\epsilon)dv \tag{3.20}$$

where C corresponds to the cross-correlation function, S to the stellar spectrum, M to the template spectrum, both expressed in velocity space v. The aim is to minimizes the value of ϵ in C.

In Fig. 3.6 we display some of the parameters of the CCF. The full width at half-maximum (FWHM) of the CCF is determined by the stellar rotation. The bisector (BIS) measures the symmetry of the CCF. As the CCF contains the spectrum lines, the shape and symmetry of the CCF depends on the shape and symmetry of the spectrum lines. The contrast corresponds to the relative depth of the CCF at its central point.

3.4.2 χ^2-minimisation

In this thesis we used NAIRA pipeline developed by Astudillo-Defru (2015), which consists of a χ^2 minimisation method instead of the CCF method. The binary mask used in the CCF method does not take into consideration all the spectral features in the case of cool stars. However, NAIRA is an adequate pipeline when deriving radial velocities of M dwarfs as the stellar template consists of a true spectrum of a star of this spectral type, rather than a synthetic one. It consists in a high signal-to-noise spectrum obtained from the median of the entire set of data. It also incorporates a true telluric template in order to account for telluric lines correction.

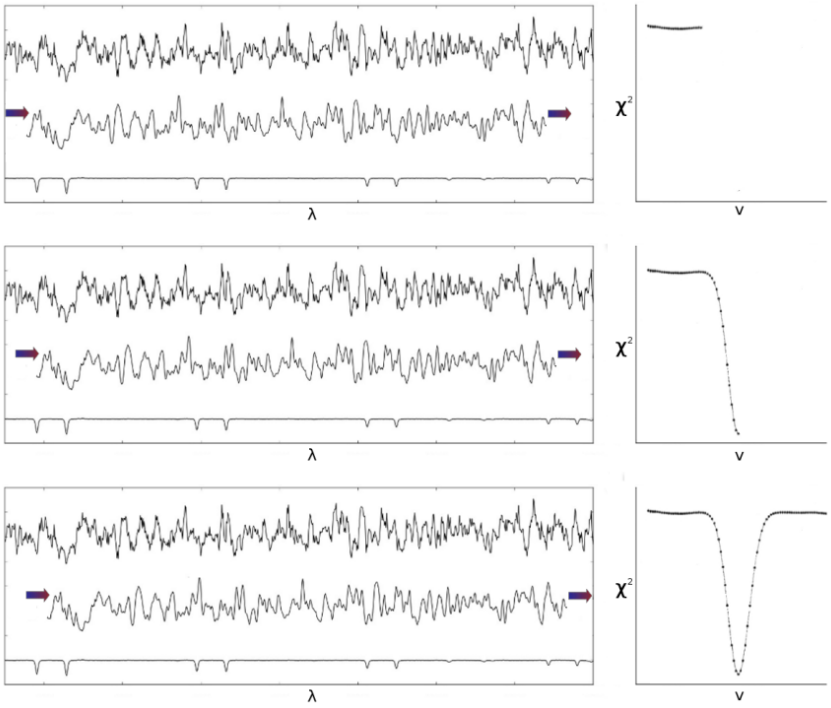

FIGURE 3.7: *(Left panels):* An observed spectrum, a stellar template and a telluric template (from top to bottom). The stellar template is shifted at different velocities and the telluric template is used to discard telluric zones. *(Right panels):* Illustration of the χ^2-minimisation approach (taken from Fig. 4.2 - Astudillo-Defru, 2015)

In Fig. 3.7 we show a representation of the χ^2-minimisation process, which is computed by the following equation

$$\chi^{2_i}_s = \frac{1}{\mathrm{df}} \cdot \sum \left(\frac{N^i - T^i_{s,Bl,Scl}}{\sigma_i} \right)^2 \tag{3.21}$$

$$\sigma_i = \sqrt{T^i_{s,Bl,Scl} + \sigma^{2_i}_{ro}} \tag{3.22}$$

where df refers to the degrees of freedom given by $\mathrm{df} = n_o \cdot n - 2$, N^i is the observed flux, $T^i_{s,Bl,Scl}$ is the template flux, σ_i is the photon error, and σ^i_{ro} is the CCD read-out-noise. This approach considers at once the entire spectral range (except for rejected zones, such as tellurics). The residuals scaled by photon errors are stored for every order, the squared sum is performed, and the degrees-of-freedom are normalized.

For a detailed description of this procedure please refer to Astudillo-Defru (2015). His pipeline has demonstrated to work efficiently as it has been compared to the CCF method by computing RV for many stars. Its RV errors are smaller compared to other CCF methods, such as the official HARPS pipeline. Therefore, due to its successful performance on M dwarfs, we use it in our work in order to obtain more adequate and precise RV for Gl 832, an M dwarf which is the subject of our study.

Chapter 4

Stellar Activity

Stellar activity is a term referred to the stellar phenomena produced by the magnetic fields in cool stars. In this section we will review how activity works in our Sun and low-mass stars, how it can be measured, it effects on the detection of exoplanets by the RV method and its modelling.

4.1 Magnetic activity in the Sun

Our own Sun has been a subject of study since remote times and its understanding allows us to comprehend the physics of other stars. Spots on the Sun's surface have been observed since the epoch of Galileo, which led to the posterior calculation of the solar activity cycle period. This activity is quasi-periodic as the activity level is not constant over time, lasting approximately 11 years. It is measured by the observed sunspots on the stellar surface, as they variate in quantity, increasing over time but reaching a minimum at the end of the cycle. This is followed by a flip of the magnetic field, switching the places of the north and south poles.

In order to understand how magnetism works in the Sun, we must first be familiar with its structure. In Fig. 4.1 we observe the layers found in the interior of the Sun. At the center is the core, making up about 25% of the solar interior (in radius). On top, we find the radiative zone and just above it we find the convective zone, which makes about 30% of the interior. We then have the photosphere, chromosphere and the corona, which extends into outer space through solar wind. Stellar activity appears in these latter layers.

Energy is generated in the core by nuclear fusion and is transported outwards by photons through the radiative zone, heating the bottom part of the convective zone. This produces the plasma to move towards the surface and sinking back down as it cools down (see the red arrows in Fig. 4.1). Between the radiative and convective zone there is a thin layer known as *tachocline* (Spiegel and Zahn, 1992), where strong shear forces are produced due to the different rotations of the adjacent zones. Since the Sun is not a solid body, it does not rotates as one, it rather rotates deferentially as the the Sun's equatorial regions rotate faster (about 24 days) than the polar regions (rotating once in more than 30 days). In the interior, the radiative zone rotates uniformly whereas the convective zone has a differential rotation, as seen in Fig. 4.2.

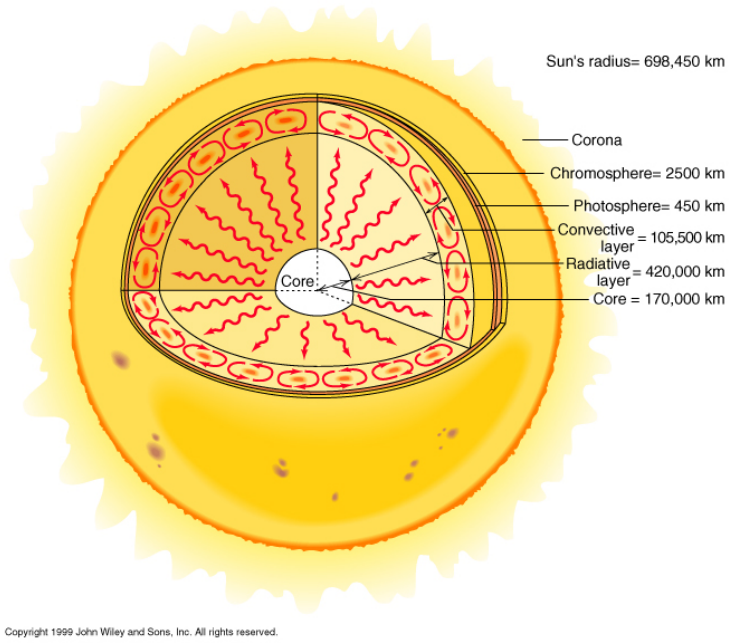

FIGURE 4.1: Schematized representation of the solar interior with its corresponding layers. The red arrows illustrates the energy transport in the radiative and convective zone (taken by ESO; Copyright 1999 John Wiley and Sons, Inc.).

The shear forces produced in the tachocline are responsible for the generation of the magnetic field explained by the dynamo theory (e.g. Parker, 1955), being therefore responsible for stellar activity.

4.2 Magnetic activity in cool low-mass stars

The above description occurs for stars with masses ranging from 0.35 to 1.5 solar masses. In low-mass stars ($M<0.35\ M_{\odot}$) the main mechanism of energy transport is convection as the convective layer is bigger than the radiative layer (if present at all). If there is no radiative zone, then the star is fully convective and therefore there is no tachocline present. These stars present a different dynamo mechanism (e.g. Morin et al., 2008; Chabrier and Küker, 2006). Low-mass stars are magnetically active and their activity level depends on many factors, such as age, rotation period, mass and spectral type.

As for M dwarfs, a large fraction of them tend to have strong magnetic fields (e.g. Shulyak et al., 2019, and references therein). More massive M dwarfs have magnetic fields with a strong toroidal component and lowest mass M dwarfs present poloidal magnetic fields (e.g. Donati et al., 2008). This transition occurs in the full-convection threshold ($M>0.35\ M_{\odot}$), giving a strong evidence that the dynamo process mainly depends on the presence of the tachocline.

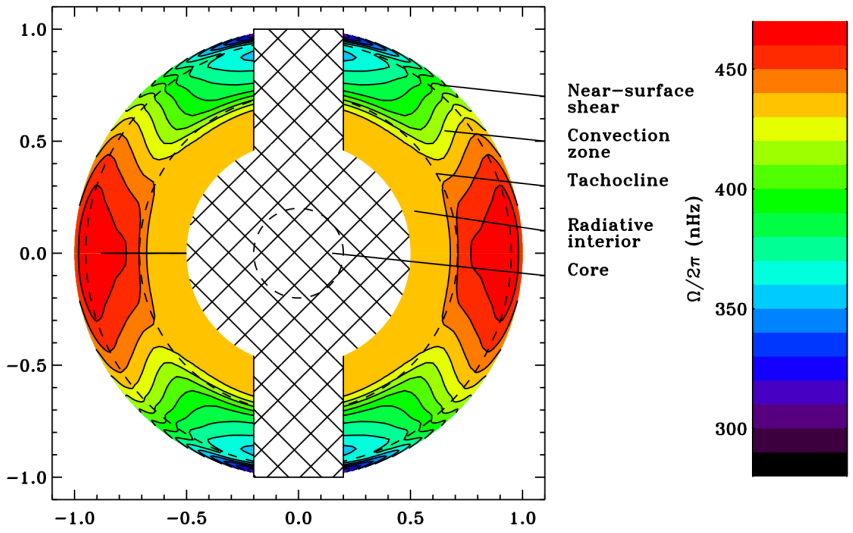

FIGURE 4.2: A section of the Sun's interiors showing its different rotation (taken from Fig. 1 - Howe, 2009).

4.3 Stellar magnetic activity manifestations

Stellar magnetic activity manifestations have a great impact on RV measurements, for which is necessary to comprehend them in order to mitigate their effects on the data. The main manifestation of activity in Sun-like and cool low-mass stars are presented below.

4.3.1 Oscillations

Acoustic oscillations, commonly known as *p-modes*, are generated in the interior of stars due to pressure fluctuations and produce ripples on the surface of the star. Oscillations in the Sun were detected in the early 1960s (Leighton, Noyes, and Simon, 1962), and approximately after a decade it was realized that oscillations could be used to study the Sun's interior. Therefore, the study of stellar oscillations allows us to comprehend the internal structure and dynamics of stars, with the combination of theory and observations performed thanks to the great advancement in technology. But this phenomenon can be a difficulty in RV measurements, specially when looking for planetary signals.

In Fig. 4.3 we observe stellar oscillation present in RV data of Aldebaran, the brightest star in the constellation Taurus. A planet was found orbiting around this star but they also noticed oscillation phenomenon present in the RV data. Stellar oscillations have timescales of minutes and produce RV variations of the order of tens of cms^{-1} (Schrijver and Zwaan, 2000). In order to mitigate stellar oscillation effect on RV data some observational strategies can be performed, such as making observations of at least 15 minutes per night (Dumusque et al., 2011).

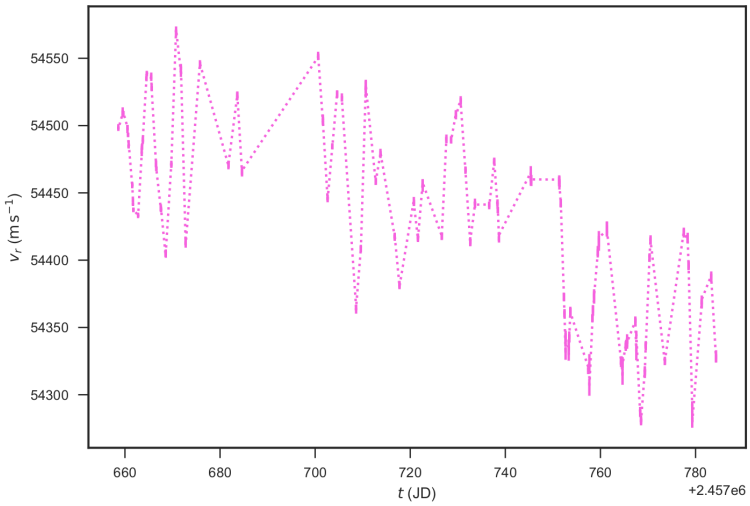

FIGURE 4.3: Aldebaran RV measurements. The presence of oscillations can be observed (taken from Fig. 3 - Farr et al., 2018).

4.3.2 Granulation

Granulation is the process of the formation of granules in the stellar photosphere, just above the convection zone. In the latter layer, energy transport by convection takes place, producing convection cells in the stellar surface, as illustrated in Fig. 4.4. They are brighter in the center due to the hotter rising plasma which when cooling down they descend forming the darker edges. This results in blueshift and redshift due to their ascending and descending motions, respectively. In this manner, granulation produces RV variations as there is a larger portion of hot ascending plasma in the surface, resulting in a net blueshift.

The time-scale of granulation ranges from 5 minutes to 30 minutes (Bray, Loughhead, and Durrant, 1984; Hirzberger et al., 1999) causing RV variations of the order of meters per second (Lindegren and Dravins, 2003). They can be organized into larger assemblies, which can remain in the surface from 30 minutes to 6 hours for mesogranules (Del Moro, 2004) and 20 hours for supergranules (Rast, 2003).

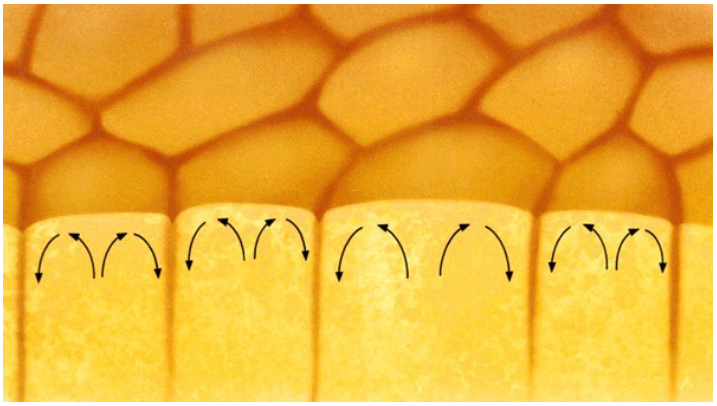

FIGURE 4.4: Representation of a section of the Sun with granulation. The black arrows represent the convective motion produced in the convection zone (taken from Coe College).

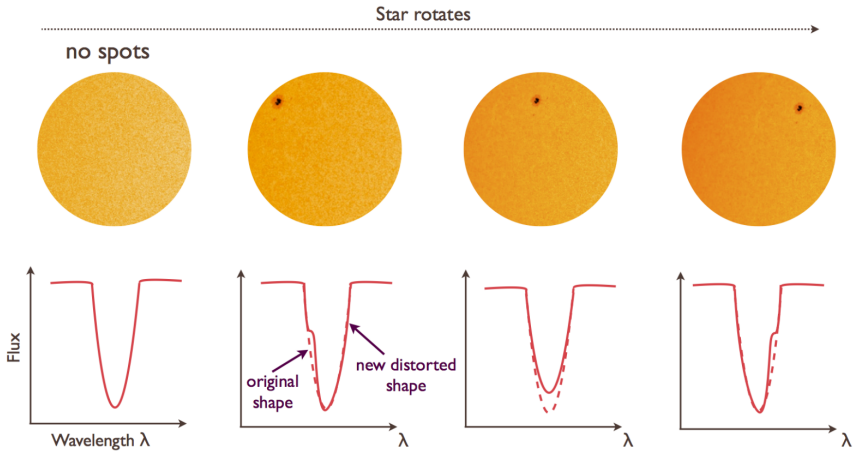

FIGURE 4.5: Illustration of how spots modulated by the rotation of the star can induce RV variation as they produce asymmetries in the spectral lines (taken by Fig. 1.4 - Haywood, 2015).

In order to suppress their effect on RV data, observational approaches can be performed, such as the one proposed in Dumusque et al. (2011) in which they state that the important factor is the number of measurements instead of the time total observational time.

4.3.3 Spots, faculae and plages

Spots, faculae and plages are modulated by the stellar rotational period, making them a challenge to deal with as they cause significant RV variations that can interfere with exoplanet detection and characterization.

Spots are produced by magnetic fields that inhibit part of the outgoing hot and bright plasma, producing dark areas of lower temperature and brightness compared to their surrounding. Spots on the Sun have been studied since last century (Hale, 1908) and they have helped us to understand spot in other stars. As seen in Fig.4.5, as the star rotates spots move in and out of view, altering the shape of spectral lines and leading to RV variations. The suppression of convective blueshift also induces RV variations.

The strength of the RV variations produced by spots depends on the rotation and activity levels of the surface of the star, reaching quasi-periodic RV variations up to tens of meters per second (Saar and Donahue, 1997). Their time-scales are also associated to the rotation of the star, which can last from hours, days or weeks.

Faculae are "bright spots". Similar to spots, they are produced by strong magnetic fields and are formed in the stellar photosphere. They can also remain in the stellar surface for days and weeks and can cause RV of up to 10 ms^{-1} (Haywood, 2015). In Fig. 4.6 we can observe solar facuale which correspond to the bright section of the solar photosphere, which can be grouped together into larger assembles or surrounding dark sunspots.

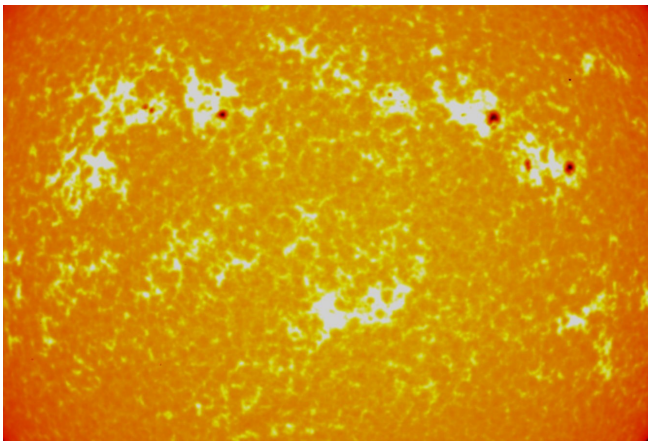

FIGURE 4.6: Section of the stellar disk with sunspots and facuale on its surface (taken from NASA).

Plages are bright regions but unlike faculae they are formed in the chromosphere instead of the photosphere. These characteristic has a great impact as spectral lines produced in the chromosphere such as Ca II H & K and Hα (see Section 4.4) can be used to study the level of activity in a star.

All these phenomenon have an effect on RV measurements as they induce variations in spectral lines by moving in and out out view of the stellar surface as well as inhibiting convection that causes blueshift distortion of spectrum lines. They are very significant in planetary detection as these RV variations can be of the same order as a planetary companion, leading to false positives (e.g. Queloz et al., 2001; Desidera et al., 2004; Udry et al., 2007; Bonfils et al., 2007; Huélamo et al., 2008; Santos et al., 2014; Haywood et al., 2014; Johnson et al., 2016). Of all the activity manifestations, they are the most complicated to treat, but there are ways to disentangle their effect, as seen in Section 4.5.

4.3.4 Magnetic cycles

As we have seen in Section 4.1, our Sun has a long term magnetic cycle. In Fig. 4.7 we observe the sunspots migration related with the quasi-periodic solar cycle. This is known as the "butterfly diagram" and it shows that as the cycle begins, sunspots are located at mid latitude ($\pm$ 30°) and they start to move towards the equator until there is a decrease of solar activity and the cycle starts again.

According to a survey performed by Baliunas et al. (1998) with the aim to study activity in stars, about 60% of the stars in the study were found to have periodic variations with cycles ranging from 7 to 30 years. Stars with long-term magnetic cycles can induce RV variations up to tens of meters per second for a lifetime of many years (Gomes da Silva et al., 2012). In this manner, long-term magnetic cycles can be a difficulty in planetary detection when dealing with promising planets with long periods as the RV measurements can be contaminated with stellar noise.

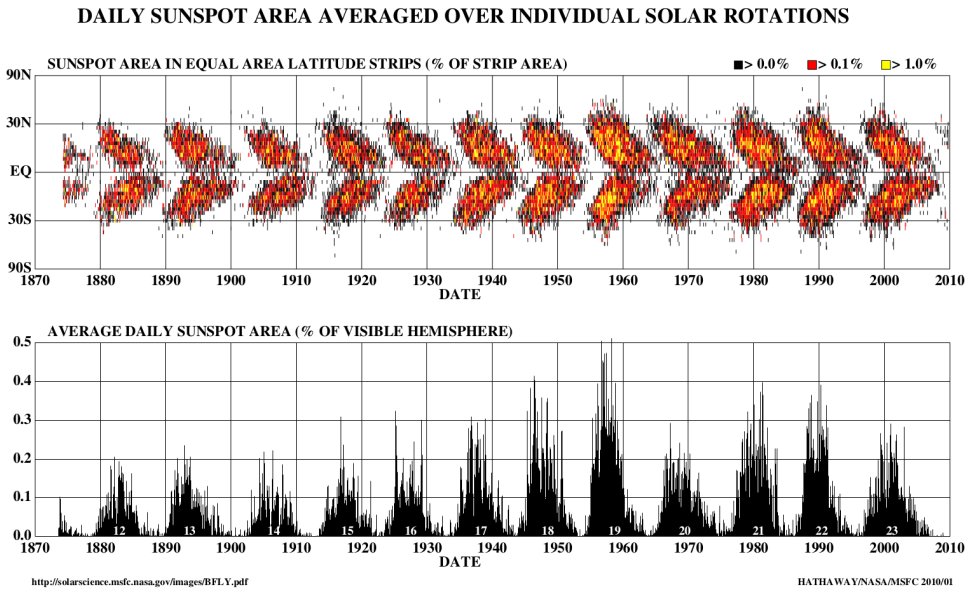

FIGURE 4.7: Solar butterfly diagram displaying sunspots migration towards the equator and the area they are occupying in the surface of the Sun as the cycle progresses (taken from Fig. 8 - Hathaway, 2010).

We have seen that due to the magnetic activity of a star, a series of phenomenon can be produced in the stellar surface which produces RV variations. These has a great impact on the signal analysis as they contribute to noise. Oscillations and granulation can be treated by an observation strategy, while long-term magnetic cycle have to be considered when dealing with long observations and studying long periodic promising signals. This leaves us only with rotational modulated phenomena, which are the hardest to treat in RV data. In the following section we will review spectroscopic analysis that allows us to quantify activity in stars.

4.4 Spectroscopic stellar activity indicators

Stellar activity indices are tracers of stellar magnetic activity. In this section we will review the main stellar indicators derived from stellar spectra that are used in the analysis of stellar activity. They are affected mainly by magnetic activity, meaning that they do not provide information of planetary companions, making them ideal to disentangle planetary signal from stellar noise.

For active stars, such as M stars, the Ca II H & K, Hα and Na I D lines are dominated by the chromospheric component, causing the appearance of these lines in emission. Magnetic activity arises from H and Ca II atoms which are excited by collision of free electrons produced by the photoionization due to high temperatures. The atoms excited by collision of free electron emit radiation and therefore are used as magnetic activity tracers in the chromosphere.

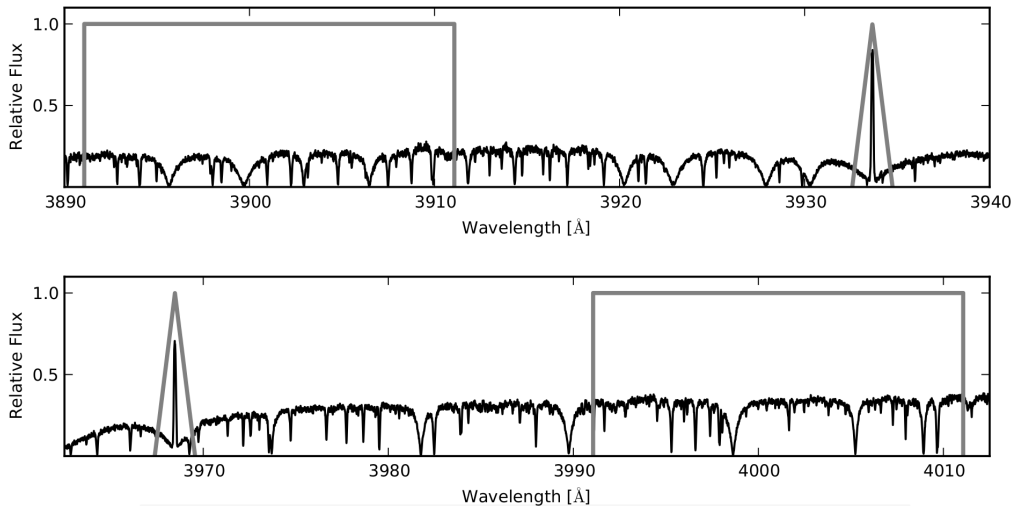

FIGURE 4.8: Median HARPS rest-frame spectrum of a Gl 699 showing the pass-bands matching th Mount Wilson Ca II H & K pass-band (taken from Fig. 1 - Astudillo-Defru et al., 2017).

4.4.1 S-index

The S-index, defined from the emission lines of Ca II H & K, was first used by Vaughan, Preston, and Wilson (1978) in the Mount Wilson Observatory. During the program, they made a stellar activity monitoring, observing approximately sixty stars of solar type in order to quantify stellar activity through the S-index. This index can be expressed as

$$S = \alpha \frac{F_H + F_K}{F_V + F_R} \tag{4.1}$$

where F_H y F_K represent the flux in pass-bands centered in the H and K lines and F_V and F_R indicate the flux in pass-bands in the violet and red part of the H and K lines. The value α is a normalization factor. The flux measured in the pass-bands depend on the stellar spectral type and on the instrument used. In this thesis, we used S-index derived from HARPS data, where for F_H and F_K triangular pass-bands of FWHM 1.09 Å centered in the H and K lines are used. While for F_V and F_R square pass-bands of width of 20 Å in the violet part (centered at 3901 Å) and red (centered at 4001 Å) part of the H and K lines are used (Suárez Mascareño et al., 2015). This can be visualized in the Fig. 4.8. The constant $\alpha \sim 1$ (Astudillo-Defru et al., 2017).

4.4.2 Hα

Another activity index used is Hα, which is defined as

$$H\alpha_{\text{Index}} = \frac{H\alpha}{H\alpha_L + H\alpha_R} \tag{4.2}$$

where Hα refers to the Hα spectral line while Hα_L is the left continuum and Hα the right continuum. Considering HARPS instrument, a rectangular pass-band with

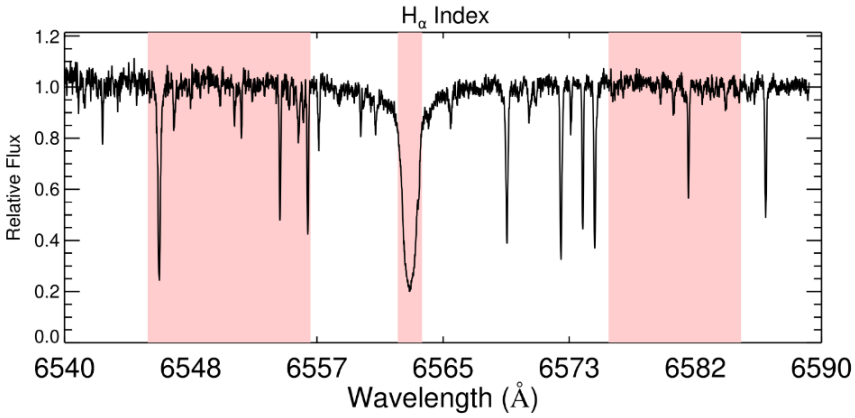

FIGURE 4.9: Spectrum of GJ176 illustrating the pass-bands of the Hα index (taken from Fig. 3 - Suárez Mascareño et al., 2018).

a width of 1.6 Å centred at 6562.808 Å is used in the Hα line, whereas the continuum bands consists of pass-bands of width of 10.75 Å and a 8.75 Å centred at 6550.87 Å and 6580.31 Å, for Hα_L and Hα_R, respectively (Gomes da Silva et al., 2011). This is illustrated in Fig. 4.9

Other Balmer lines indices are used to study magnetic activity, such as the **Hβ index** (λ=4861.3 Å) and **Hγ index** (λ= 4340.4 Å) are but are not commonly used as the Hα index. This is due to the fact that these lines are less strong compared to Hα since the Hα transition has more probability to occur compared to the other transitions, causing the Hα transition to occur with more frequency in comparison to the other Balmer series lines. In fact, as we move forward in the Balmer series, they decrease their significance as activity indicators since the transitions are less probable than the previous one. These tracers are defined in the same way was the other indicators described above: the ratio between the flux of the line and the sum oh the continuum flux on both side of the line.

4.4.3 Na I D

A different activity tracer is the Na I D index, which lines are centered in λ= 5895.9 Å and λ= 5889.9 Å. On M dwarfs, the sodium lines give information about the conditions on lower and medium parts of the chromosphere (Mauas, 2000). As Hα and Ca II H & K are emitted from the upper and lower chromosphere, respectively, the use of all of these indices allows us to have a complete study of magnetic activity. Following the definition of Gomes da Silva et al. (2011), the Na I D index from HARPS is calculated from the average flux centered in both lines using pass-bands of width of 0.5 Å for each one. This average flux is later divided by the average of two references bands with windows of 10 and 20 Å centered in 5805.0 y 6090.0 Å, respectively. Nevertheless, it is important to mention that these lines are usually contaminated by emission lines coming from sodium telluric lines (Hanuschik, 2003), for which a careful treatment must be performed.

In this sense, the S, Hα and Na I D indices are efficient tracers that are used in the study of magnetic activity in M-dwarfs (Gomes da Silva et al., 2011). These indicators can be modelled in order to disentangle planetary signal form stellar activity signal, as we will see later.

4.5 Modelling stellar activity with Gaussian Processes

In this thesis we use Gaussian Process (GP) regression to analyze stellar activity as they are useful tool to model correlated noise (e.g. Rasmussen and Williams, 2006; Roberts et al., 2012). GP are used to model stochastic processes with some known properties. They can describe signals of stellar activity because although there are many unknown parameters, we know that they are (quasi-) periodic since they are modulated by the stellar rotation.

GP is based on Bayesian framework as it is a non-parametric model, in which the form of the model is not imposed previously. The correlation of the data points is what needs to be determined formerly, for which the covariance matrix $\mathbf{K}$ is used, where its elements are determined by a covariance function $k(t_i, t_j; \phi)$ given by

$$\mathbf{K}_{i,j} = k(t_i, t_j; \phi) \tag{4.3}$$

The covariance function k with *hyperparameters* ϕ provides the covariance element between any two times t_i and t_j. In exoplanet literature, a quasi-periodic kernel is commonly used to model stellar magnetic activity (e.g. Haywood et al., 2014; Grunblatt, Howard, and Haywood, 2015; Rajpaul et al., 2015; Faria et al., 2016), with its covariance function defined as

$$\sum_{ij} = \eta_1^2 \exp\left[-\frac{|t_i - t_j|^2}{\eta_2^2} - \frac{\sin^2(\frac{\pi|t_i - t_j|}{\eta_3^2})}{2\eta_4^2} \right]. \tag{4.4}$$

where η_1 corresponds to the amplitude of correlations, η_2 is the aperiodic timescale decay of correlations , η_3 is the periodic component and η_4 is the periodic timescale. These corresponds to the hyperparameters. When modelling stellar magnetic activity, η_3 can be interpreted as the stellar rotation and η_2 as the timescale decay of an active zone. Determining the best hyperparameters to use is a procedure known as "training the GP".

Accounting for the orbital parameters γ and the hyperparameters ϕ, these can be varied in order to maximize the marginal likelihood function (Gibson et al., 2012) which is described by the probability density function (PDF) defined by Bayes's Theorem as

$$p\Big(\theta(\gamma, \phi)|\mathcal{D}\Big) \propto \ln \mathcal{L}\Big(\mathcal{D}|\theta(\gamma, \phi)\Big) \tag{4.5}$$

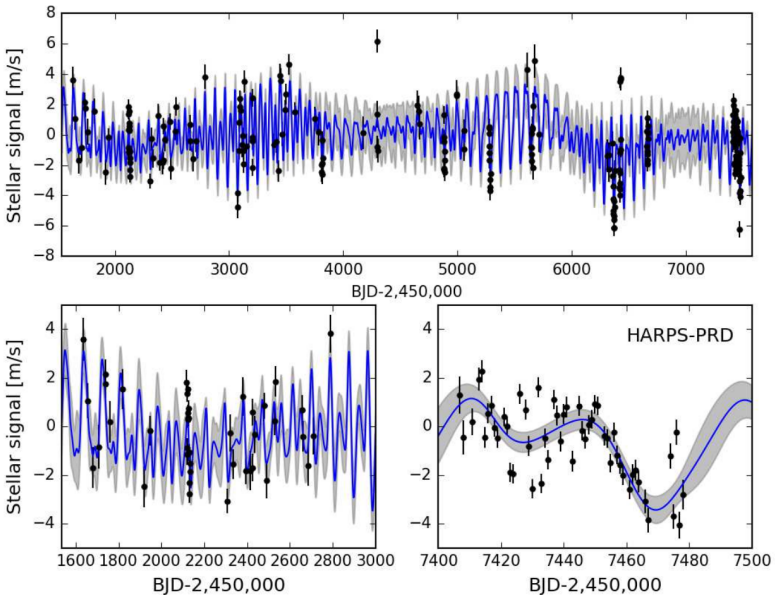

FIGURE 4.10: RV residuals of Proxima b. The blue line with grey 1σ region represents the GP best-fit model for the stellar noise. The bottom panels are a close up zoom in order to visualize the efficient fit (taken from Fig. 5 - Damasso and Del Sordo, 2017).

with θ (which includes γ and ϕ) being the priors and $\mathcal{D}$ the data set. The likelihood function is given by

$$\ln \mathcal{L}\Big(\mathcal{D}|\theta(\gamma,\phi)\Big) = -0.5\mathbf{r}^T\mathbf{K}^{-1}\mathbf{r}^T - 0.5\ln\left[\det\right](\mathbf{K}) - 0.5N\ln\left(2\pi\right) \tag{4.6}$$

where N is the number of data points, and $\mathbf{r}$ the vector of residuals of the data. In the GP framework, this function is maximized by the Markov chain Monte Carlo (MCMC). This refines lousy distributions over many different functions, which shapes are controlled by γ and ϕ, and precisely defines distributions that better fit the data.

In Fig. 4.10 we show how stellar noise of the residuals of Proxima b was modelled with GP, noticing the agreement between the model and the data. Therefore, in the RV models that accounts for both the Keplerian K (with its orbital parameters γ) and stellar activity (included in the GP with its hyperparameters ϕ), the total RV model is given by

$$\mathrm{RV}_{\mathrm{model}} = K(\gamma) + GP(t_i, t_j; \phi) \tag{4.7}$$

GP has been used in stellar activity analysis in order to mitigate their effect of exoplanetary detection, being an elegant and efficient way already proven to work accurately. In our study, we used RADVEL (Fulton et al., 2018) to model planetary signals (Keplerians) and stellar activity (see Chapter 5). This python package is easy to use and is suited for our study as it incorporates GP modelling. It contains a variety of priors to constrain the hyper-parameters (e.g. Jeffreys, HardBounds, Gaussian) and estimates their uncertainties through MCMC exploration of the posterior probability, determining the size and shape of the posterior probability density.

Chapter 5

A detailed re-analysis of the planetary system around Gl 832

This chapter contains the main study of this thesis. The research consist of a spectroscopic study of the RV and activity tracers of the Gl 832 system in order to determine if the inner planet exists or if its signal was mimicked by the activity of the star. This study is in process of publication.

5.1 Introduction

Gliese 832 (Gl 832) is an M2V star located in the constellation of Grus (RA: 21h 33m 33.9s, DEC: 49°00'32.4"). In Table 5.1 we show its stellar parameters, noticing that it consist of an M dwarf located only 4.95 pc away from us with a mass of 0.45 $M_{\odot}$. In this very close system, a gas-giant planet in a wide orbit was discovered (Bailey et al., 2009) and also an inner planet orbiting within the stellar habitable zone (Wittenmyer et al., 2014), corresponding to a super Earth or mini-Neptune. They both were discovered by the RV method. But the inner planet has a orbital period of 35.68 $\pm$0.03 days, being close to the stellar rotational period 45.7 $\pm$9.3 days (Suárez Mascareño et al., 2015). In this sense, our aim is to determine if the this the 35 RV signal is modulated by stellar activity, causing a false positive, or if in fact corresponds to the inner reported planet.

TABLE 5.1: Stellar parameters of Gl 832.

Parameter	Value	Reference
RA (J2000)	21h33m33.97s	Gaia Collaboration (2018)
Dec (J2000)	-49°00′32.40′′	Gaia Collaboration (2018)
Parallax (mas)	201.4073 ± 0.0429	Gaia Collaboration (2018)
Distance (pc)	4.965 ± -0.001	Gaia Collaboration (2018)
Spectral Type	M2V	Suárez Mascareño et al. (2015)
Luminosity ($L_{\odot}$)	0.020	Boyajian et al. (2012)
Mass ($M_{\odot}$)	0.45	Bonfils et al. (2013)
T_{eff}(K)	3522	Gaidos et al. (2014)
Fe/H	-0.19	Santos et al. (2013)
log R'_{HK}	-5.10	Jenkins et al. (2006)
log g	4.83	Gaidos et al. (2014)

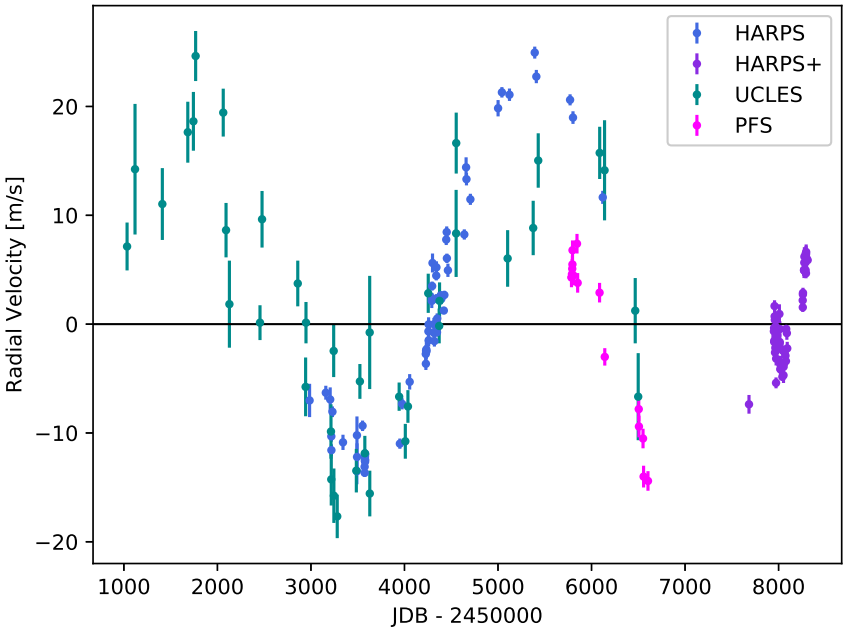

FIGURE 5.1: RV timeseries of Gl 832. Data from HARPS before (blue) and after (purple) the upgrade is shown, as well as UCLES (green) and PFS (magenta) data (Gorrini et al. in prep.).

Our data used in this study is described below.

HARPS: From the High Accuracy Radial Velocity Planet Searcher (HARPS) we used 54 published data. As for new data, we included 62 new obtained spectra. As HARPS underwent through a fiber change (Lo Curto et al., 2015), 54 of our new spectra were obtained after this upgrade and the resting 8 before it. This makes a total of 116 HARPS data, which are displayed in the Appendix, in Tables 6.1 and 6.2, corresponding to the data before and after the fiber change, respectively. The time-span corresponds to 5325 days with an average RV precision of 0.59 ms^{-1} and an average signal-to-noise ratio at order 60 of 114.014.

PFS: From the Planet Finding Spectrograph (PFS) we incorporated a total of 16 archival measurements with 818 days span and an average RV uncertainty of 0.9 ms^{-1}. The PFS data is displayed in Table 6.3.

UCLES: From the University College London Echelle Spectrograph (UCLES) we have used in our study a total of 39 archival data with a 5465 days span and mean RV error of 2.59 ms^{-1}. This data is listed in Table 6.4.

In Fig. 5.1 we show the RV timeseries of Gl 832 using data set mentioned above, denoting with a plus sign "+" the HARPS data after the fiber upgrade. We observe a clear RV variation with a dispersion of 40 ms^{-1} and a mean error 1.08 ms^{-1}.

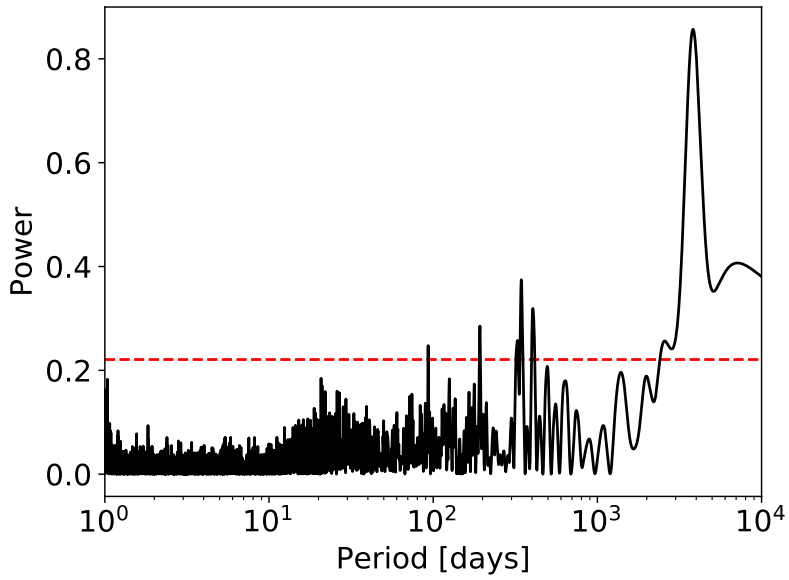

FIGURE 5.2: Generalized Lomb-Scargle (GLS) periodogram of Gl 832. The dashed red lines corresponds to the 1% FAP threshold. The highest significant peak is around 3800 days (Gorrini et al. in prep.).

5.2 Analysis

5.2.1 Periodograms

We begin our study by making a signal analysis, computing the Generalized Lomb-Scargle Periodogram (GLS; Zechmeister and Kürster, 2009) for our whole set of data, as shown in Fig 5.2. We clearly see that near 3800 days the highest peak is located, with a significance above the 1% FAP threshold. This peak agrees with the orbital period reported as planet b. Accounting for this signal we perform a Keplerian fit using RADVEL (Fulton et al., 2018), which is a python package that models RV time series by fitting the radial velocity curve given by

$$v_r = K[\cos(\nu + \omega) + e\cos(w)] \tag{5.1}$$

with

$$M = E - e\sin E \tag{5.2}$$

$$\nu = 2\tan^{-1}\left(\frac{\sqrt{1+e}}{\sqrt{1-e}}\tan\frac{E}{2}\right) \tag{5.3}$$

This Keplerian model resulted in the orbital solutions listed in Table 5.6 (1-Keplerian model). After subtracting this Keplerian solution, we computed the GLS periodogram of the residuals, displayed in Fig. 5.3. We observe that the only signal above the level of confidence is near 184 days. Therefore, the 35 days RV signal, reported as planet

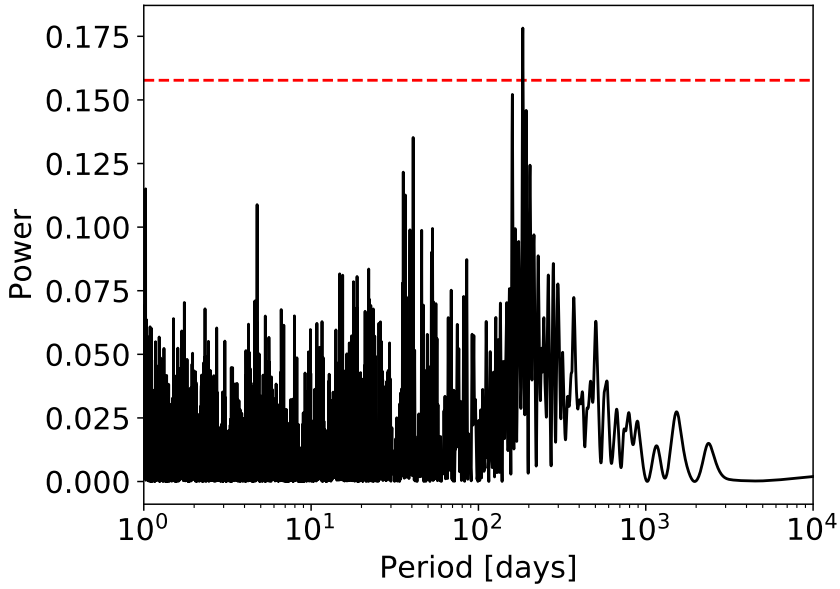

FIGURE 5.3: GLS periodograms of the residuals. The red dashed lines represent the 1% FAP threshold. The only signal above this level of confidence is near 184 days (Gorrini et al. in prep.).

c, does not reach the level of confidence. This motivates us to study its origin, as well as the dominant 184 signal in the residuals.

5.2.2 Stellar rotational period

As we have mentioned, the stellar rotational period of Gl 832 is very close to the orbital period of the reported inner planet. This, combined with the fact that the signal of this planet does not reach the 1% FAP threshold, encourage us to study its precedence. First, we calculate the stellar rotational period to see if there is an agreement with 45.7 ± 9.3 days reported by Suárez Mascareño et al. (2015).

We do this by calculating the S-index, an activity tracer (see Section 4.4) following Astudillo-Defru (2015). As activity tracers are affected by stellar activity, they can be modulated by the rotational period of the star. In this sense, we can calculate the rotational period from activity tracers (e.g. Suárez Mascareño et al., 2015). Since we only have the stellar spectra from HARPS, we were only able to compute the S-index from this instrument. After obtaining these values, we modelled this index using RADVEL performing Gaussian process regression using a quasi-periodic kernel, given by (see Section 4.5)

$$\sum_{ij} = \eta_1^2 \exp\left[-\frac{|t_i - t_j|^2}{\eta_2^2} - \frac{\sin^2(\frac{\pi|t_i - t_j|}{\eta_3^2})}{2\eta_4^2} \right]. \tag{5.4}$$

We first model each set of data set (before and after the fiber upgrade) separately, in order to constrain the amplitude. The resulting models are shown in Fig. 5.4, noticing that the S-index calculated from the HARPS data reaches an amplitude of

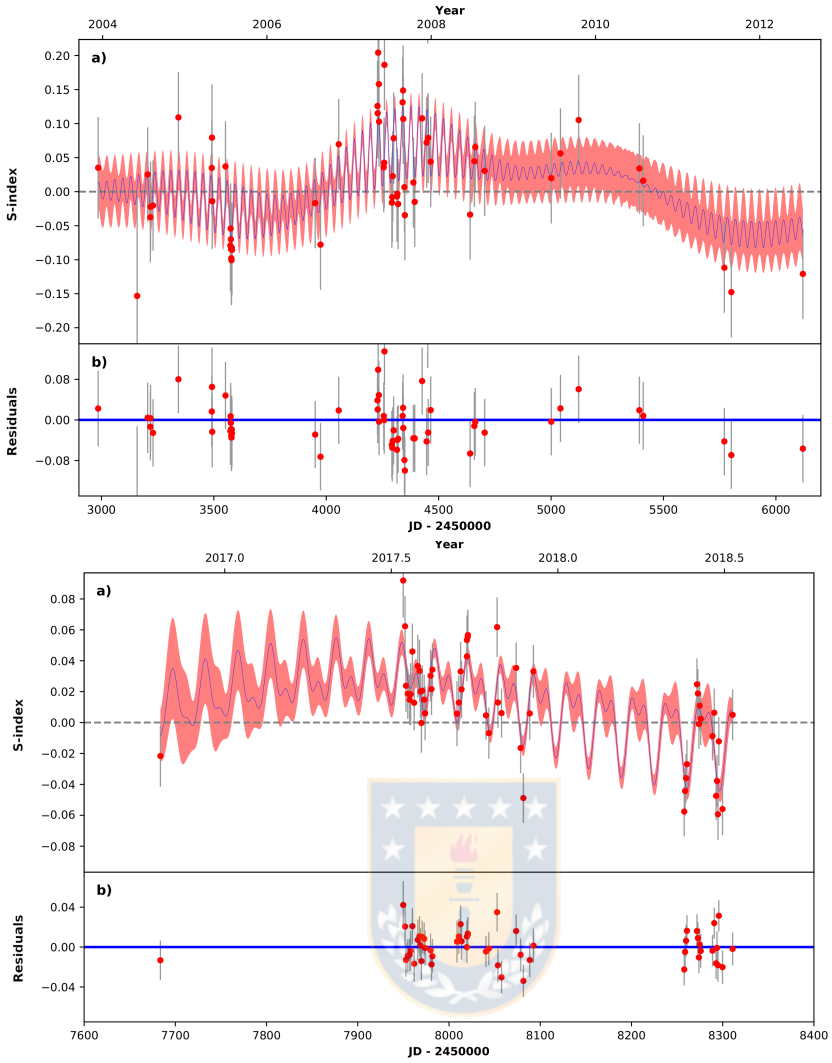

FIGURE 5.4: S-index modelled with GP for the values calculated by HARPS data before (upper) and after (bottom) the fiber change.

0.20 whereas for HARPS+ it reaches an amplitude of 0.9. In this manner, we constrained the amplitude η_1 as a bounded prior going from 0 up to 1.0, as seen in Table 5.2. We also used a bounded prior for the periodicity parameter η_3, going from 1.0 to 100 days. The resulting model is displayed in Fig. 5.5.

The posterior distributions from this model are shown in Figure 5.6, observing that the periodic component has a value of $35.7\ ^{+0.95}_{-0.26}$ days, improving this parameter by 89.78% with respect of the reported value. This value is extremely similar to the orbital period of the reported planet c (35.68 ± 0.03 days).

So far we have found that the 35-days signal, reported as planet c, does not appear as a significant signal in the residual periodogram. Moreover, the rotational period of Gl 832 resulted to be coincide with the orbital period of this inner planet. Therefore, it is probable that this planet could be an artifact of stellar activity, but in order to be certain about this we need to make a rigorous analysis. This is why we need to model the planets around this system alongside stellar activity.

TABLE 5.2: Priors used in the S-index modelling with GP.

Bounded prior: $-1000.0 < \gamma_{\rm harps} < 1000.0$
Bounded prior: $-1000.0 < \gamma_{\rm harps+} < 1000.0$
Bounded prior: $0.0 < \sigma_{\rm harps} < 0.1$
Bounded prior: $0.0 < \sigma_{\rm harps+} < 0.1$
Bounded prior: $0.0 < \eta_{1,\rm harps} < 1.0$
Bounded prior: $0.0 < \eta_2 < 4000.0$
Bounded prior: $1.0 < \eta_3 < 100.0$
Bounded prior: $0.0 < \eta_4 < 7.0$

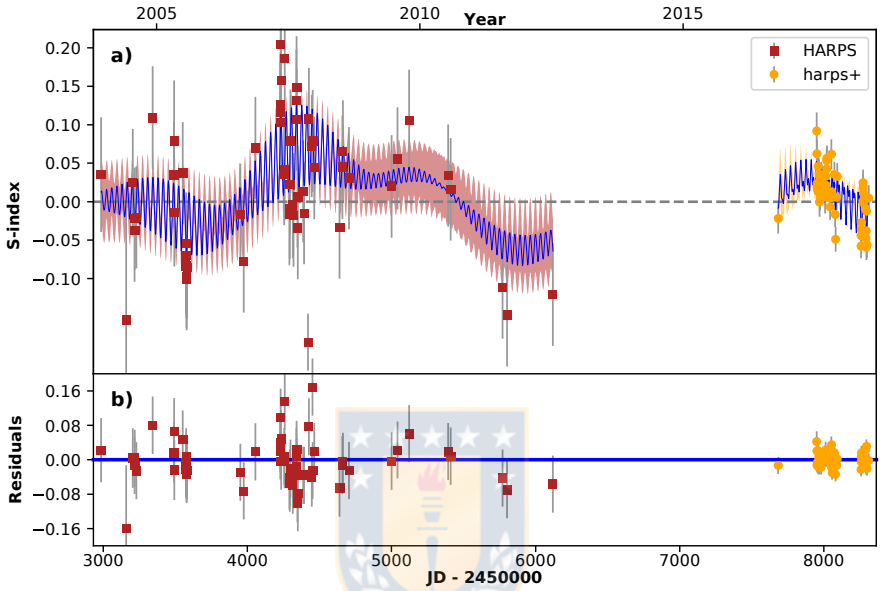

FIGURE 5.5: *Top panel*: S-index modelled with GP. HARPS data before (red squares) and after (yellow circles) the upgrade are displayed. The blue line corresponds to the fit of the data and the shaded regions indicate the confidence interval. *Bottom panel*: residuals of the GP fit (Gorrini et al. in prep.).

5.2.3 One-Keplerian model plus Gaussian Process

In this context, we performed a 1-Keplerian model with stellar activity, i.e. with GP based on the S-index modelling. This means that the priors for this model corresponds to Gaussian hyperparameters (η_2, η_3, and η_4) whose center and width correspond the posteriors of the S-index model, as seen in Table. 5.3.

The resulting fit is shown in Fig. 5.7, where the RV time series is fitted alongside the maximum-a-posteriori model. The list of posteriors, the corner plots for the derived and free parameters for this model can be found in Table 5.4, Fig. 5.8, and Fig. 5.9, respectively. We notice that the main orbital solutions agree with the ones reported as planet b, as seen in Table 5.5. After subtracting this Keplerian fit from the RV, we computed the GLS periodogram of the residuals, as seen in Fig. 5.10. We observe that this time, all the signals do not reach the 1% FAP threshold. Therefore, the 35-days and 184-days signals are absorbed by the GP.

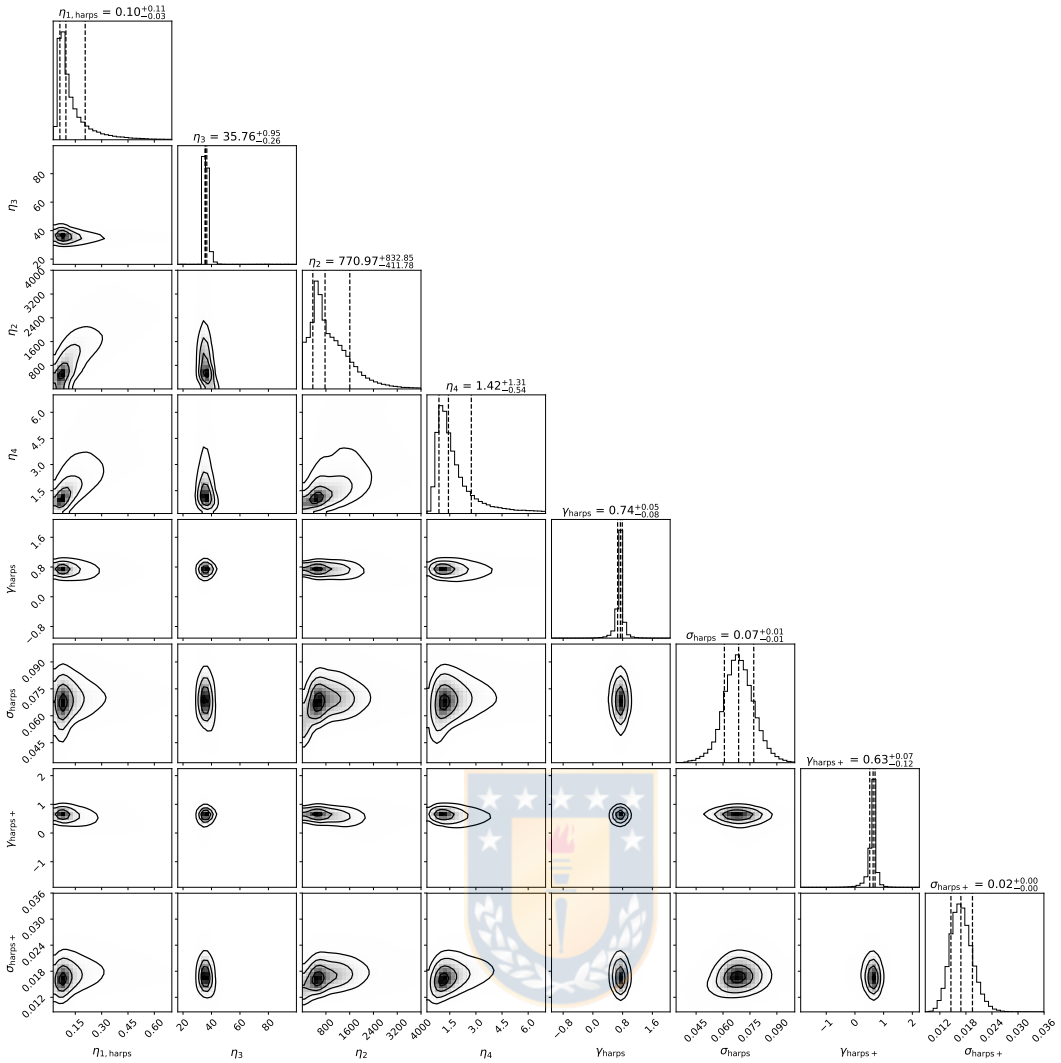

FIGURE 5.6: Marginalized posterior distribution of the GP parameters for the S-index. The parameter η_3, i.e., the stellar rotational period, has a value of approximately 35.76 days (Gorrini et al. in prep.).

TABLE 5.3: Summary of priors of the 1-planet Keplerian fit with GP.

K constrained to be > 0
e_b constrained to be < 0.99
Bounded prior: $1000 < P_b < 10000$
Bounded prior: $2454365.2 < T\mathrm{conj_b} < 2458365.2$
Bounded prior: $0.0 < \sigma_{\mathrm{harps}} < 10.0$
Bounded prior: $0.0 < \sigma_{\mathrm{harps+}} < 10.0$
Bounded prior: $0.0 < \sigma_{\mathrm{ucles}} < 20.0$
Bounded prior: $0.0 < \sigma_{\mathrm{pfs}} < 10.0$
Bounded prior: $0.0 < \eta_{1,\mathrm{harps}} < 10.0$
Bounded prior: $0.0 < \eta_{1,\mathrm{ucles}} < 20.0$
Bounded prior: $0.0 < \eta_{1,\mathrm{pfs}} < 20.0$
Gaussian prior on η_2: 771 ± 8832
Gaussian prior on η_4: 1.42 ± 1.31
Gaussian prior on η_3: 35.76 ± 0.95

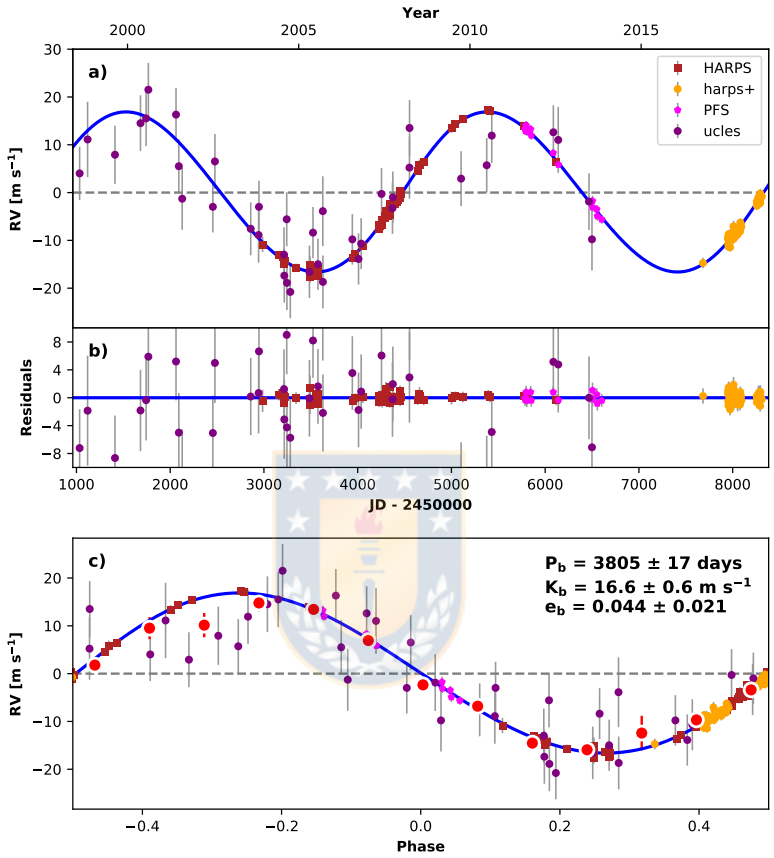

FIGURE 5.7: Best-fit of the 1-planet Keplerian orbital model plus GP for Gl 832 using our entire set of data. The thin blue line is the best fit 1-planet model. We add in quadrature the RV jitter terms with the measurement uncertainties for all RVs. **b)** Residuals to the best fit 1-planet model. **c)** RVs phase-folded to the ephemeris of planet b. The small point colors and symbols are the same as in panel **a**. Red circles are the same velocities binned in 0.08 units of orbital phase. The phase-folded model for planet b is shown as the blue line (Gorrini et al. in prep.).

TABLE 5.4: MCMC posteriors of the Keplerian-1-planet fit with GP.

Parameter	Credible Interval	Maximum Likelihood	Units
Modified MCMC Step Parameters			
P_b	3805^{+16}_{-18}	3854	days
$T\mathrm{conj_b}$	2456318^{+15}_{-12}	2456387	JD
e_b	$0.044^{+0.021}_{-0.02}$	0.042	
ω_b	$-0.69^{+0.75}_{-0.47}$	-1.38	radians
K_b	$16.57^{+0.59}_{-0.62}$	16.8	m s^{-1}
Orbital Parameters			
P_b	3805^{+16}_{-18}	3854	days
$T\mathrm{conj_b}$	2456318^{+15}_{-12}	2456387	JD
e_b	$0.044^{+0.021}_{-0.02}$	0.042	
ω_b	$-0.69^{+0.75}_{-0.47}$	-1.38	radians
K_b	$16.57^{+0.59}_{-0.62}$	16.8	m s^{-1}
Other Parameters			
γ_{ucles}	3.4 ± 1.1	3.5	m s-1
γ_{pfs}	-11 ± 1	-12	m s-1
$\gamma_{\mathrm{harps+}}$	$13355.3^{+1.0}_{-1.1}$	13357.0	m s-1
γ_{harps}	$13356.25^{+0.48}_{-0.49}$	13356.43	m s-1
$\dot{\gamma}$	$\equiv 0.0$	$\equiv 0.0$	m s^{-1} d^{-1}
$\ddot{\gamma}$	$\equiv 0.0$	$\equiv 0.0$	m s^{-1} d^{-2}
σ_{ucles}	$5.37^{+1.1}_{-0.85}$	5.12	m s^{-1}
σ_{pfs}	$2.2e-08^{+2.4e-08}_{-1.4e-08}$	$8.9e-08$	m s^{-1}
$\sigma_{\mathrm{harps+}}$	0.86 ± 0.23	0.69	m s^{-1}
σ_{harps}	$0.61^{+0.24}_{-0.21}$	0.5	m s^{-1}

1200000 links saved
Reference epoch for γ,$\dot{\gamma}$,$\ddot{\gamma}$: 2454704.703772

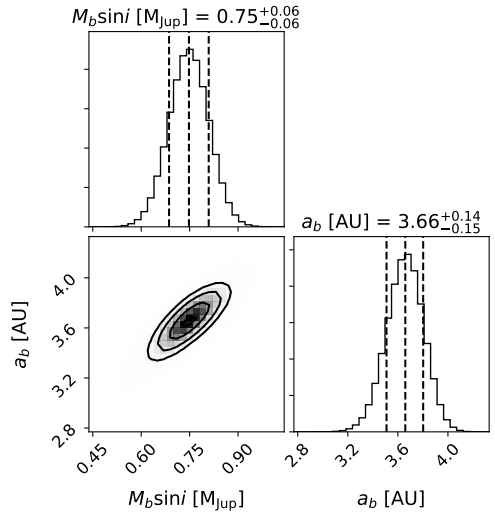

FIGURE 5.8: Posterior distributions for the derived parameter from the Keplerian fit with GP (Gorrini et al. in prep.).

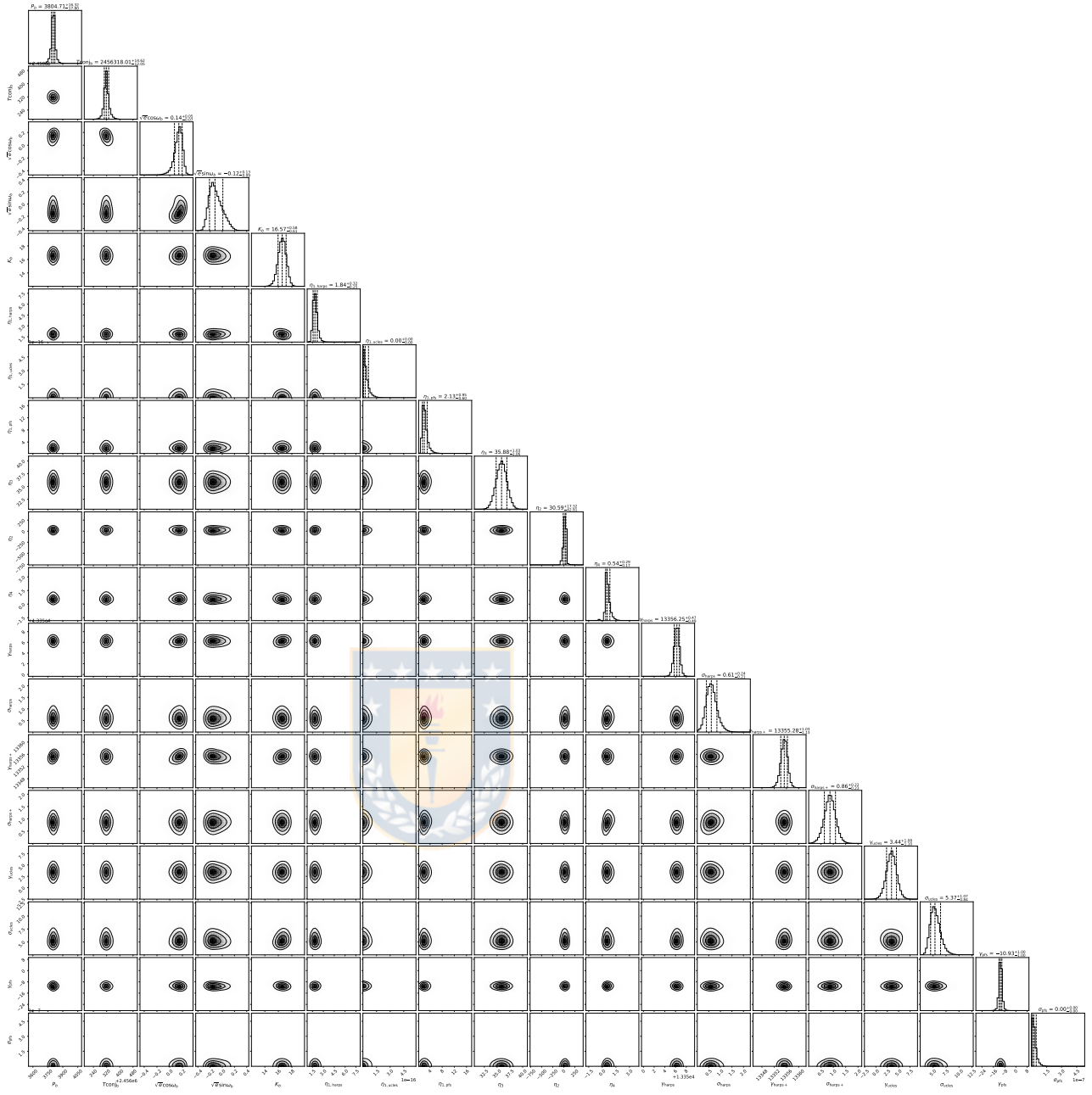

FIGURE 5.9: Posterior distributions for all free parameters derived for the 1-planet model with GP included (Gorrini et al. in prep.).

TABLE 5.5: Model comparison table between our 1-Keplerian + GP model and the reported solutions for planet b.

Parameters	1-Keplerian + GP model solutions	Solutions by Bailey et al. (2009)
Orbital period (days)	3805 ± 17	3416 ± 131
RV semi-amplitude (ms^{-1})	16.6 ± 0.6	14.9 ± 1.3
Eccentricity	0.044 ± 0.021	0.12 ± 0.11
Minimum mass (M_{JUP})	0.75 ± 0.06	0.64 ± 0.06
Semi-major axis (AU)	3.66 ± 0.15	3.4 ± 0.4

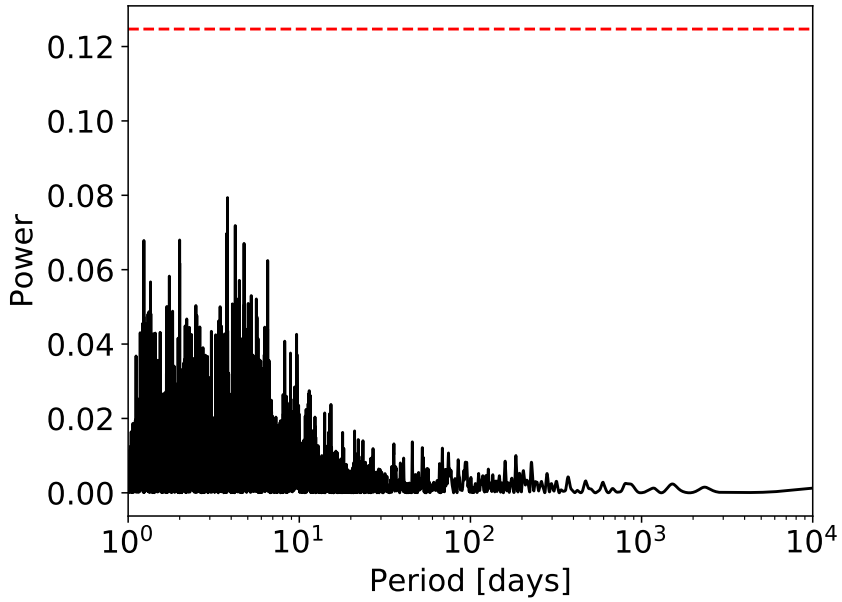

FIGURE 5.10: GLS periodogram of the residuals from the Keplerian model with GP. The dashed red lines corresponds to the 1% FAP threshold, noticing that all the signals are below it. There is no remaining significant signal left (Gorrini et al. in prep.).

5.2.4 Two Keplerian model

So far, the 1-Keplerian model with GP agrees with the solution reported for planet b. But the residuals periodogram absorbs the signals of interests of study: the 35-days and 184-days signal, where the former is reported as planet c and it coincides with the stellar rotational period, and the latter appeared in the GLS periodogram of the residuals in the Keplerian model without GP, i.e. without accounting for stellar activity.

In this sense, this lead us to consider that both of these signals might not have planetary origin. But it is necessary to add these signals in the Keplerian model in order to study them. In this manner, we perform a 2-planet Keplerian fit that includes the 35 and 184 RV signals in different models. One Keplerian to account for the planet b, and another Keplerian accounting for a planet with 35-days or 184-days periodicity, as illustrated below. This can be done as the RV dispersion of the residuals, which corresponds 24 ms^{-1}, are still significantly larger than the internal errors, meaning that the RV variation is not coming from internal errors and could be produced for another physical phenomenon.

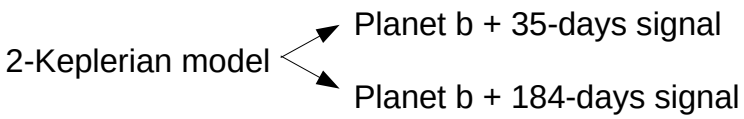

Planet b + 35-days signal model

For this model we constrained the radial velocity semi-amplitude K to be greater than zero, and for the eccentricities of both Keplerians to be less than 0.99. As for the orbital periods, we used a Bounded prior ranging from 1000 to 10000 days for planet b, and from 35 to 36 days for the other signal.

This fit is shown in Fig. 5.11. The orbital period for the outer planet resulted in P_b= 3790 $\pm$ 12 days. The RV semi-amplitude resulted in K_b= 16.81 $\pm$ 0.47 ms^{-1}. The eccentricity resulted in e_b= 0.058 $\pm$ 0.014. For the inner planet the resulting orbital parameters are given by P_c= 35.249 $\pm$ 0.021 days; K_c= 0.94 $\pm$ 0.42 ms^{-1}; e_c=0.76 $\pm$ 0.13.

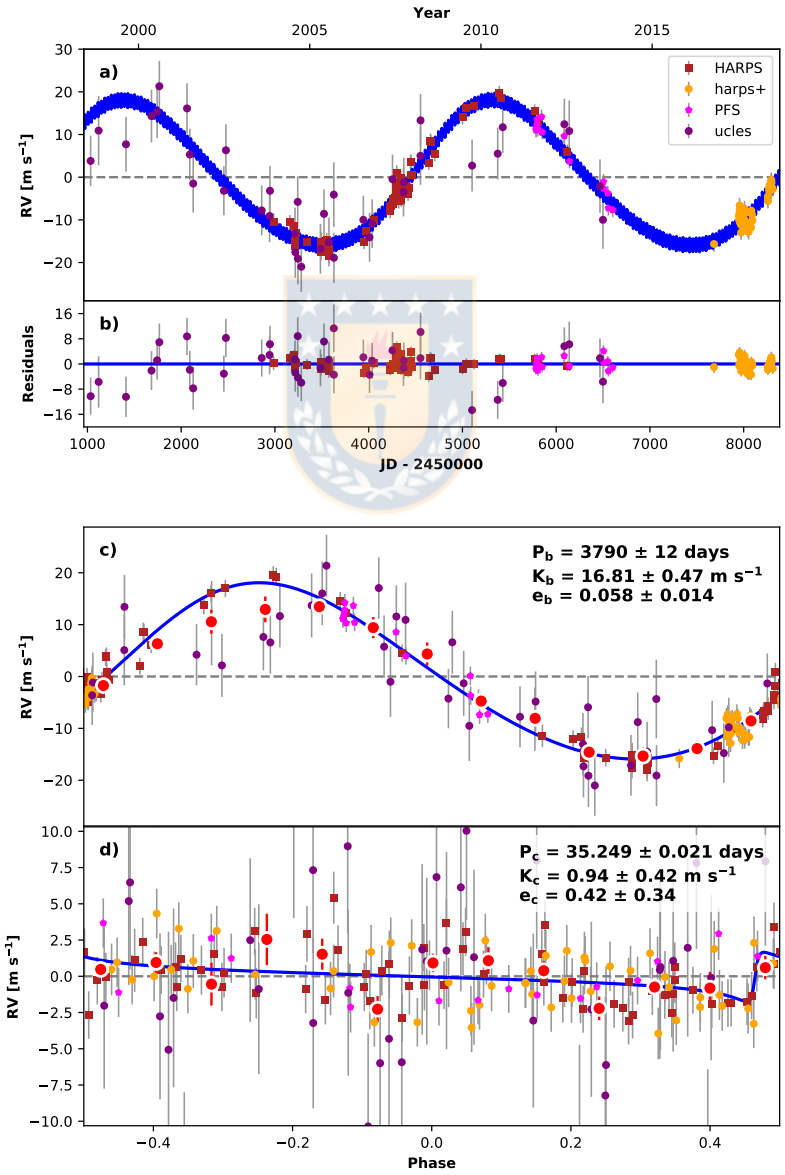

FIGURE 5.11: RV fit accounting for two Keplerians (planet b signal and 35-days signal).

Planet b + 184-days signal model

Just like as the previous model (planet b + 35-days signal), we constrained K to be positive, both eccentricities to be less than 0.99 and the orbital period for planet b as a Bounded prior ranging from 1000 until 10000 days. Since we are accounting for the 184-days signal, we used a Bounded prior ranging from 150 to 195 days to account for the 184-days periodicity. The resulting model is displayed in Fig. 5.12, with the following orbital parameters for the outer planet: P_b= 3773 $\pm$ 21 days; K_b= 16.65 $\pm$ 0.37 ms^{-1}; e_b =0.027 $\pm$ 0.014. As for the other Keplerian, the orbital parameters resulted in P_c= 183.35 $\pm$ 0.22 days; K_c= 1.86 $\pm$ 0.45 ms^{-1}; e_c =0.67 $\pm$ 0.14.

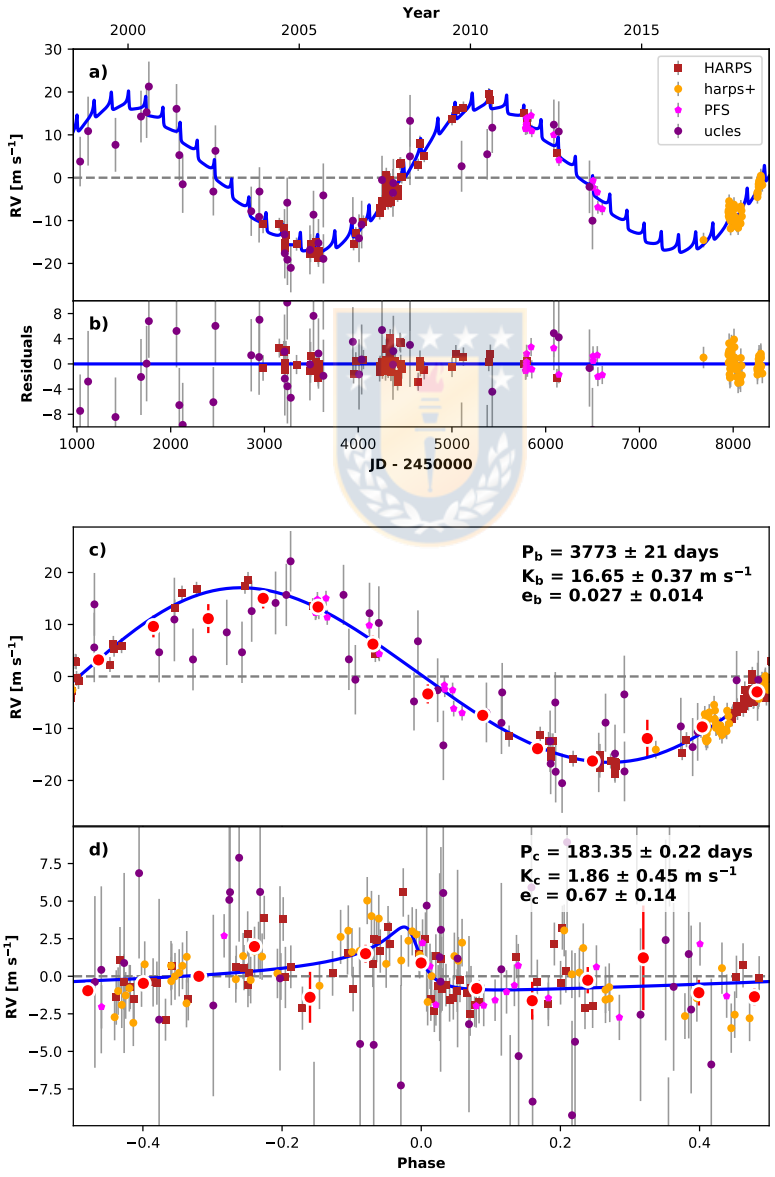

FIGURE 5.12: RV fit accounting for two Keplerians (planet b signal and 184-days signal).

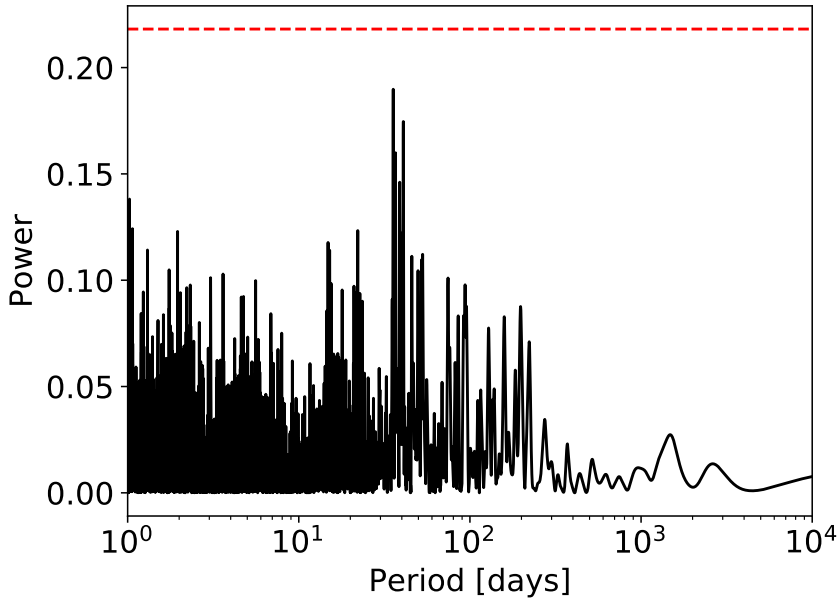

FIGURE 5.13: Same as Fig. 5.3 but without considering the data after the HARPS fiber upgrade. The 184-days signal vanished and all the remaining signals fall under the 1% FAP threshold.

We observe in Fig. 5.12 that this model shows an unsmooth fit to the RV data, as seen in panel **a)**. Moreover, we notice in panel **d)** that the fit seems to follow HARPS+ data (after the fiber upgrade from HARPS). This signal is not likely to have a telluric origin, since these lines are taking into account in NAIRA pipeline created by Astudillo-Defru (2015) (see Section 3.4.2), and therefore they have been corrected in our analysis. In order to be certain if the HARPS+ data generated the 184-days signal, we re-compute the GLS periodogram of the residuals shown in Fig. 5.3 but without this data set.

In this manner, for our set of data without considering HARPS+ data, we re-make the analysis performed in Section 5.2.1. That is, we make a 1-Keplerian fit (without GP) and we subtract it to the RV, computing in this way the GLS periodograms of the residuals, as shown in Fig. 5.13. We notice that without this data, the 184 days signal vanished, just like it did when incorporating a GP in the Keplerian fit considering this data. Therefore, is seems that the HARPS data after the fiber change generated this signal. In this periodogram, the 35-days signal is the highest, but as all the other signal, they do not reach the confidence level of 1% FAP threshold.

5.2.5 Two Keplerian model plus Gaussian Process

Now we proceed to account for stellar activity. In this manner, we add to the 2-Keplerian model a GP regression for each model. The GP priors used are the same as for the 1-Keplerian plus GP model (Section 5.2.3).

Planet b + 35-days signal + GP model

For this model we used the same priors as the 1-Keplerian model plus GP, listed in Table 5.3, but we incorporated the parameters for the second planet. For this, we used constrained the eccentricity to be less than 0.99 and used Bounded priors for the orbital period, ranging from 35 to 36 days. The resulting fit is displayed in Fig. 5.14. The orbital period for the inner planet resulted in P_c= 35.4282 $\pm$ 0.0097 days, whereas the RV semi-amplitude resulted in K_c= 1.55 $\pm$ 0.52 ms^{-1} and an eccentricity of e_c=0.76 $\pm$ 0.13. We observe that, curiously, the resulting orbital period is extremely close to the rotational period of the star ($\sim$ 35.76 days).

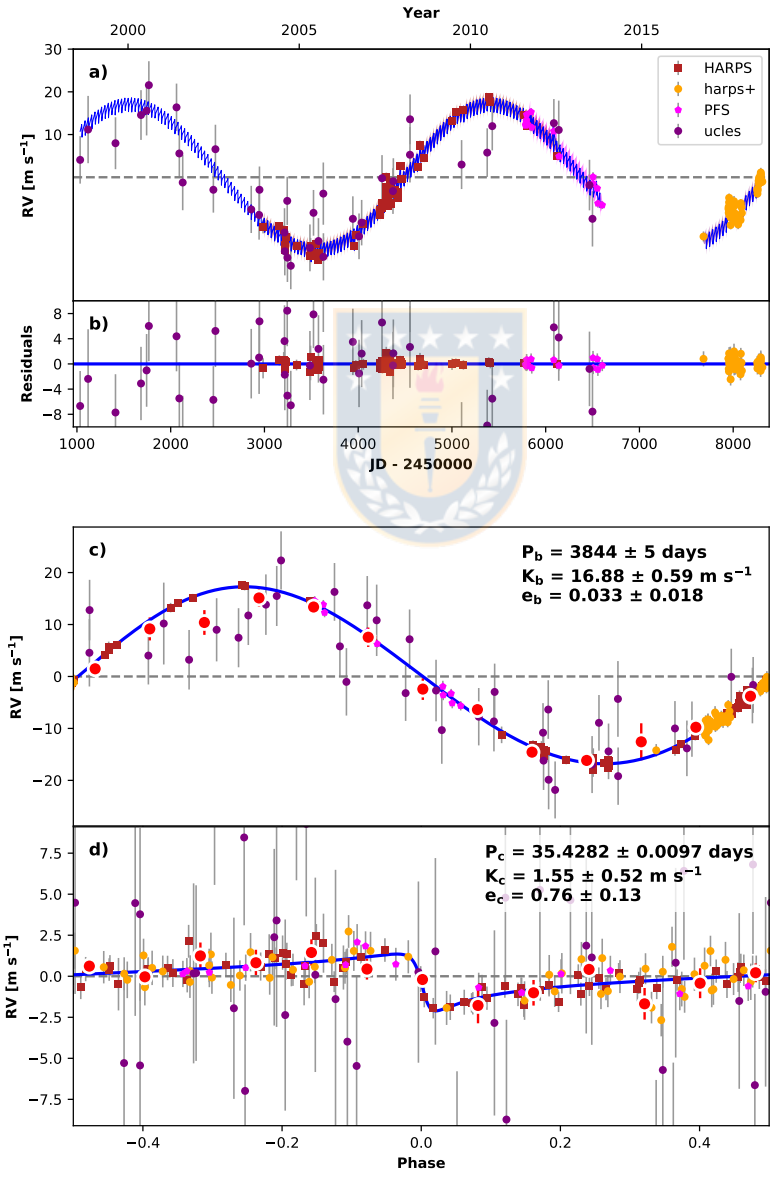

FIGURE 5.14: RV fit accounting for two Keplerians (planet b signal and 35-days signal) plus GP.

Planet b + 184-days signal + GP model

In this model we considered the resulting posteriors in the 2-Keplerian model (planet b + 184-days signal). In this manner, we constrained K to be positive and both eccentricities to be less than 0.99. We used Gaussian priors on the period of both signals (P_b= 3773 $\pm$ 23 and P_c= 183.35 $\pm$ 0.26). We also added the Gaussian hyperparameters resulting in the S-index model, which were later used in the 1-Keplerian model plus GP and in the 2-Keplerian model plus GP (planet b + 35-days signal + GP). The resulting model is shown in Fig. 5.15. The orbital values for the 184-days signal resulted in P_c= 183.393 $\pm$ 0.051 days for its orbital period, K_c= 2.4 $\pm$ 0.8 ms^{-1} for its RV semi-amplitude and e_c= 0.85 $\pm$ 0.053 for its eccentricity.

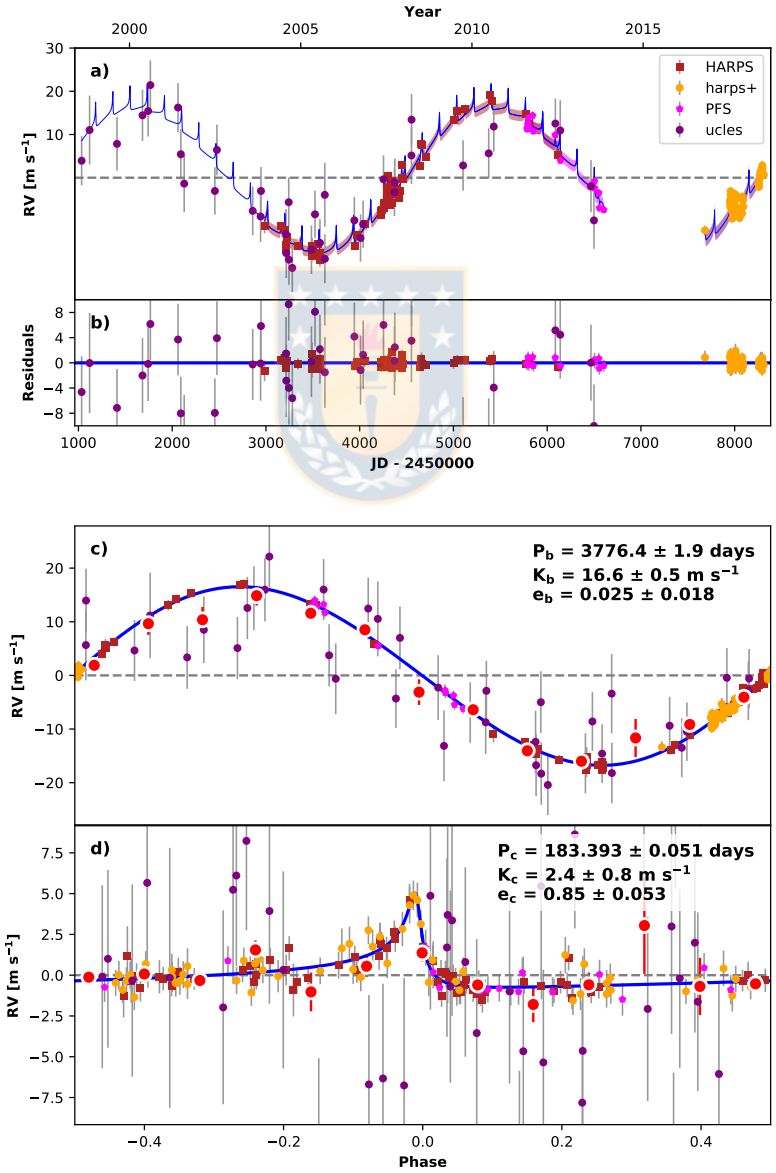

FIGURE 5.15: RV fit accounting for two Keplerians (planet b signal and 184-days signal) plus GP.

5.3 Summary and results

In this study, we began plotting the RV of Gl 832 and noticed clear RV dispersion compared to the internal errors. The GLS periodogram showed a dominant signal around 3800 days, which is reported as planet b (Bailey et al., 2009). After performing a Keplerian fit on the RV time series, we computed the GLS periodogram of the residuals, which displayed a single dominant signal on top of the 1% FAP threshold, corresponding to 184 days. The 35-days signal, reported as planet c (Wittenmyer et al., 2014), was under this level of confidence. This motivated us to study the origin of both signals.

We then re-calculated the rotational period of Gl 832 by modelling the S-index time series using GP regression, resulting in a period of 35.76 $^{+0.95}_{-0.26}$ days. We then used the posteriors distribution of the hyperparameters as priors for our subsequent GP models for account for stellar activity. First, we performed a 1-Keplerian model accounting for the 3800 days signal (planet b) plus a GP. After substracting this Keplerian model from the RV, we calculated the GLS periodogram of the residuals, where all the remaining signals were under the 1% FAP threshold, absorbing the 35 days and 184 days signals.

Subsequently we made a 2-Keplerian model accounting for planet b and for a planet with 35 or 184 days periodicity and afterwards we included GP in these models. For the models of planet b plus the 35 days signal, the orbital period of the planet resulted in a very close value of the stellar rotation period. As for the models of planet b plus the 184 days signal, the fit resulted in a very unsmooth fit and it seemed that HARPS+ (HARPS data after the fiber upgrade) data was generating this signal. Hence, the signal is not stable over time, contrary to a planetary signature. We then discarded HARPS+ data and re-did the 1-Keplerian fit (without GP). After subtracting this model, we generated the GLS periodograms of the residuals and the 184 days signal was no longer present.

The results of our models are summarized in Table 5.6, where we can statically compare our models. Below, the parameters of this table are described.

P: Orbital period (in days)
K: RV semi-amplitude (in ms^{-1})
e: Orbital eccentricity
RMS: Root mean square of the residuals (in ms^{-1}). It is used to measure the differences between the model and the data.
BIC: Bayesian information criterion. It estimates, under a Bayesian framework, the function of the posterior probability of a model from being true. Therefore, it used to select a model among a finite set of models. The model with the lowest BIC is the favoured one.
AIC: Akaike information criterion. It estimates the relative distance between the fitted and the realistic likelihood function of a model. A lower AIC value means that a

TABLE 5.6: Summary table of the models performed.

Models	P (days)	K (ms^{-1})	e	RMS (ms^{-1})	BIC	AIC	Δ AIC
1-Keplerian	P_b= 3964 ± 13	K_b= 17.09 ± 0.41	e_b= 0.061 ± 0.023	3.37	847.80	809.27	0.0
1-Keplerian + GP	P_b= 3805 ± 17	K_b= 16.6 ± 0.6	e_b= 0.044 ± 0.021	2.87	813.52	764.11	0.0
2-Keplerians (Planet b + 35)	P_b= 3790 ± 12	K_b= 16.81 ± 0.47	e_b=0.058 ± 0.014	3.26	848.90	802.16	0.0
	-----	-----	-----	-----	-----	-----	-----
	P_c= 35.349 ± 0.021	K_c= 0.94 ± 0.42	e_c= 0.42 ± 0.34				
2-Keplerians (Planet b + 184)	P_b= 3773 ± 21	K_b= 16.65 ± 0.37	e_c= 0.027 ± 0.014	3.23	822.10	775.37	0.0
	-----	-----	-----	-----	-----	-----	-----
	P_c= 183.35 ± 0.22	K_c= 1.86 ± 0.45	e_c= 0.67 ± 0.14				
2-Keplerians + GP (Planet b + 35)	P_b= 3844 ± 5	K_b= 16.88 ± 0.59	e_b= 0.033 ± 0.018	2.90	817.81	755.54	0.0
	-----	-----	-----	-----	-----	-----	-----
	P_c= 35.4282 ± 0.0097	K_c= 1.55 ± 0.52	e_c= 0.76 ± 0.13				
2-Keplerians + GP (Planet b + 184)	P_b= 3776.4 ± 1.0	K_b =16.6 ± 0.5	e_b=0.025 ± 0.018	2.98	820.84	756.09	0.0
	-----	-----	-----	-----	-----	-----	-----
	P_c= 183.393 ± 0.051	K_c= 2.4 ± 0.8	e_c= 0.85 ± 0.053				

model is considered to be closer to the truth.

In this manner, we notice that the most favoured model is the one with one planet plus GP (stellar activity), with a BIC value of 813.52. Therefore, only planet b is orbiting Gl 832. As the 184 days signal is not considered in the most probable model, and since this signal is not stable over time, we discard it to have a planetary origin.

Since the best model (1-Keplerian + GP) accounts for stellar activity, with a rotational period equivalent to the 35-days signal, we conclude that this signal is an artifact of stellar activity. This can be seen in Fig. 5.16, where we see that the periodic component of the quasi-periodic kernel is attributable to the rotational period of the star. In this manner, we conclude that this signal comes from stellar activity and not from a planetary companion, discarding in this way the existence of planet c.

In this sense, we listed the best model solutions in Table 5.7, corresponding to the updated orbital solutions of the Gl 832 planetary system.

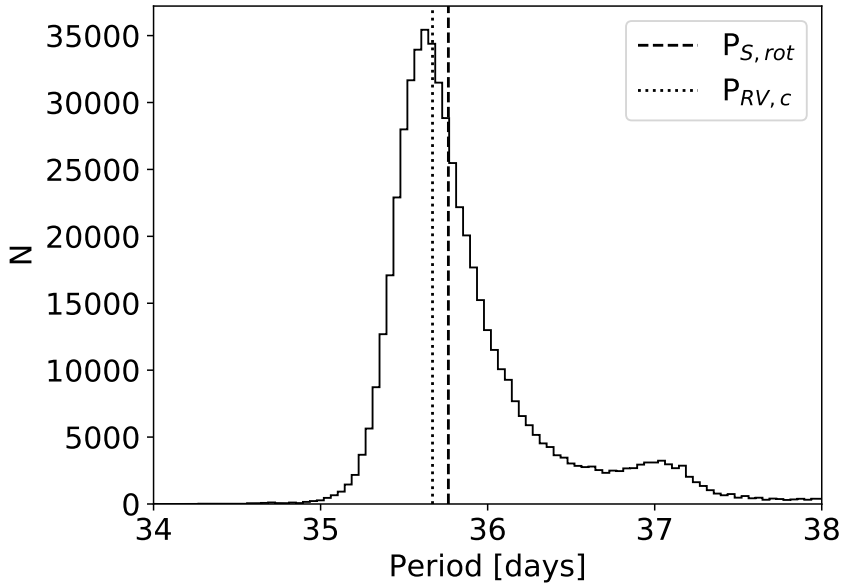

FIGURE 5.16: Histogram of the periodic component of the quasi-periodic kernel η_3, equivalent to the stellar rotation period. The vertical dashed line represents our measured value, while the dotted vertical line depicts the orbital period reported from planet c (Gorrini et al. in prep.).

TABLE 5.7: Updated orbital solutions of Gl 832.

Parameter	Value
Stellar Rotational Period (days)	$35.76\ ^{+0.95}_{-0.26}$
Orbital Period P_b (days)	3805 ± 17
Velocity semiamplitude K (ms^{-1})	16.6 ± 0.6
Eccentricity e	0.044 ± 0.021
Semi major axis a (AU)	3.66 ± 0.15
Periastron date (Julian Date)	2456318 ± 15
ω (radians)	-0.69 ± 0.75
$m \sin i$ (M_{JUP})	0.75 ± 0.06
N_{obs}	171

Chapter 6

Conclusions

In this study we have seen the main methods of detecting exoplanets, focusing in the RV method as we use it in our analysis. We have also described stellar magnetic activity, as this phenomenon is the main cause of false positives in RV data. We explained its manifestations, how to study them with spectroscopic indicators and how to model them with Gaussian Process regression (GP).

This provided the context of this thesis, as the main goal was to determine if Gl832c corresponded to a planet or by stellar activity. This planet was reported by Wittenmyer et al. (2014) but a study of rotational period of cool star performed by Suárez Mascareño et al. (2015) reported the stellar rotational period to be close to the orbital period of this inner planet.

In this research we showed that Gl 832 has only one planetary companion, planet b discovered by Bailey et al. (2009). We updated the orbital solutions for this planetary system. This was done by performing a variety of Keplerian models accounting for stellar activity by GP. Through a comparison of models by BIC value, the most likely model resulted in planet b plus stellar activity. Also, we updated the stellar rotational period, which was calculated by performing a GP over the S-index activity tracer, resulting in a value of $35.76\ ^{+0.95}_{-0.26}$ days. Since this value resulted to be attributable to the 35 days signal, reported as planet c, we discarded the existence of this planet and concluded that this signal is an artifact of stellar activity.

This shows how GP performs an exceptional task when modelling stellar activity. As we have seen, stellar activity has a great impact on planetary detection, for which is necessary to take it into consideration when analysing RV data. This phenomenon, combined with the stellar rotation, can mimic planetary companion, just like it did with Gl 832 c and many other planets (e.g. Queloz et al., 2001; Desidera et al., 2004; Udry et al., 2007; Bonfils et al., 2007; Huélamo et al., 2008; Santos et al., 2014; Robertson et al., 2014; Haywood et al., 2014; Johnson et al., 2016). In this sense, it is of great importance to study planetary systems that have planetary orbital periods close to the rotational period of its host star, as they can be produced by stellar activity.

As spectrographs are becoming more precise, detecting RV less than 1.0 ms^{-1}, such as HARPS and ESPRESSO, the RV variations caused by stellar noise will be

detected. Therefore, with the advanced technology we have nowadays, an inspection of stellar activity should always be in consideration, specially on M dwarfs as a large number of them tend to be magnetically active. These type of stars are ideal to search for exoplanets and study their magnetism will help to develop new dynamo theories for these type of stars.

Appendix

TABLE 6.1: Gl 832 HARPS data (before the fiber change)

JD-2400000	RV (kms^{-1})	Uncertainty (kms^{-1})	FWHM (kms^{-1})	Contrast	BIS (kms^{-1})	S-index
52985.519752	13.34107	0.00153	4.09968	24.20910	-0.01290	0.778938
53158.906185	13.34178	0.00064	4.04921	23.38003	-0.01698	0.590570
53205.745328	13.34116	0.00111	4.10269	24.02540	-0.01574	0.769082
53217.743898	13.33777	0.00049	4.08992	24.09481	-0.01286	0.706211
53218.707451	13.33650	0.00054	4.08924	24.03470	-0.01309	0.721721
53229.724109	13.34003	0.00049	4.09819	24.12384	-0.01305	0.723452
53342.543486	13.33722	0.00070	4.09766	24.08259	-0.01293	0.852954
53490.927221	13.33457	0.00120	4.09631	24.12619	-0.01022	0.778714
53491.913518	13.33787	0.00173	4.10742	24.02743	-0.01102	0.823226
53492.929436	13.33588	0.00125	4.09731	24.13395	-0.01276	0.729821
53551.853580	13.33874	0.00048	4.10191	24.31145	-0.01441	0.780834
53573.800209	13.33498	0.00047	4.10332	24.21516	-0.01653	0.664657
53574.733125	13.33442	0.00037	4.10304	24.27860	-0.01554	0.689627
53575.736342	13.33610	0.00042	4.10246	24.26739	-0.01502	0.673786
53576.783817	13.33554	0.00043	4.10330	24.25378	-0.01413	0.659157
53577.791707	13.33591	0.00040	4.09900	24.28294	-0.01349	0.646026
53578.746840	13.33544	0.00053	04.09939	24.25442	-0.01280	0.643162
53579.729750	13.33561	0.00049	4.10193	24.33493	-0.01334	0.661368
53580.765460	13.33615	0.00042	4.09680	24.35558	-0.01440	0.658171
53950.811870	13.33710	0.00047	4.11144	24.19916	-0.01505	0.726920
53974.635082	13.34076	0.00051	4.10318	24.20157	-0.01587	0.666015
54055.522594	13.34278	0.00071	4.10069	24.12344	-0.01618	0.813424
54227.912029	13.34534	0.00056	4.10887	24.12286	-0.01321	0.869652
54228.912771	13.34444	0.00057	4.11154	24.09726	-0.01369	0.859054
54230.881775	13.34563	0.00053	4.11308	24.04696	-0.01482	0.948125
54233.929164	13.34576	0.00086	4.10775	24.07475	-0.01006	0.901846
54234.923827	13.34558	0.00047	4.11356	24.11973	-0.01380	0.846716
54255.843190	13.34742	0.00051	4.11103	24.08475	-0.01672	0.779617
54257.882957	13.34806	0.00065	4.11495	24.11958	-0.01534	0.786320
54258.918488	13.34660	0.00058	4.11407	24.04563	-0.01331	0.930125
54291.817850	13.35022	0.00066	4.10714	23.99735	-0.01551	0.727675

Table 6.1 Continued

54293.781529	13.35047	0.00048	4.10314	24.06831	-0.01760	0.735697
54295.829509	13.35158	0.00041	4.10244	24.04360	-0.01461	0.766577
54299.835208	13.35370	0.00087	4.09939	23.93778	-0.01360	0.822307
54314.772823	13.34807	0.00059	4.10537	24.04407	-0.01354	0.736729
54316.604519	13.34727	0.00052	4.10456	24.10723	-0.01362	0.740688
54319.803791	13.34652	0.00050	4.10939	24.00040	-0.01717	0.725643
54339.648286	13.35254	0.00044	4.11561	23.97447	-0.01446	0.875083
54341.762698	13.35330	0.00055	4.10693	23.98215	-0.01286	0.892481
54342.670950	13.35043	0.00040	4.11295	24.04283	-0.01528	0.850560
54347.714531	13.34733	0.00038	4.10457	24.08693	-0.01316	0.750386
54349.729205	13.34859	0.00048	4.09811	24.04127	-0.01532	0.709234
54387.614986	13.35073	0.00038	4.10339	24.11437	-0.01361	0.757193
54393.604498	13.35039	0.00047	4.09843	24.33937	-0.01450	0.728781
54420.517975	13.34933	0.00032	4.09885	24.19178	-0.01334	1.096864
54426.517596	13.35076	0.00038	4.10184	24.16476	-0.01311	0.851506
54446.537861	13.35585	0.00050	4.10591	24.01077	-0.01624	0.816045
54451.530992	13.35654	0.00052	4.09884	23.92503	-0.01598	1.027954
54453.534279	13.35413	0.00043	4.10197	24.01523	-0.01392	0.822759
54464.538436	13.35303	0.00061	4.10250	23.97443	-0.01486	0.787767
54639.915522	13.35632	0.00047	4.09933	24.06675	-0.01481	0.710086
54658.874838	13.36249	0.00092	4.11834	24.00008	-0.01672	0.788528
54662.869727	13.36140	0.00057	4.11409	23.96877	-0.01641	0.809303
54704.703772	13.35955	0.00051	4.10277	24.15029	-0.01455	0.774324
55000.898501	13.36792	0.00075	4.10550	24.14237	-0.01570	0.763663
55041.715207	13.36938	0.00048	4.11088	24.03071	-0.01558	0.799963
55122.650028	13.36916	0.00057	4.12056	23.88694	-0.01311	0.849070
55392.785353	13.37303	0.00055	4.11205	24.03731	-0.01557	0.777894
55409.842530	13.37083	0.00061	4.10463	23.75207	-0.01476	0.759902
55770.633271	13.36869	0.00051	4.10275	23.99944	-0.01579	0.632105
55801.739503	13.36706	0.00058	4.10480	23.97652	-0.01465	0.596216
56119.858748	13.35973	0.00060	4.10929	23.95731	-0.01480	0.622958

TABLE 6.2: Gl 832 HARPS data (after the fiber change)

JD-2400000	RV (kms^{-1})	Uncertainty (kms^{-1})	FWHM (kms^{-1})	Contrast	BIS (kms^{-1})	S-index
57683.619277	13.33972	0.00086	4.13945	23.75046	0.00672	0.630911
57949.799266	13.34643	0.00103	4.15478	23.75612	0.00265	0.744521
57951.818799	13.34674	0.00081	4.15198	23.70875	0.00565	0.714882
57952.793308	13.34546	0.00057	4.14913	23.65948	0.00533	0.676372
57954.801386	13.34557	0.00053	4.15658	23.80805	0.00606	0.671237
57956.809736	13.34875	0.00053	4.15609	23.78312	0.00278	0.667328
57957.926347	13.34780	0.00079	4.15006	23.66432	0.00661	0.670867
57959.849584	13.34748	0.00055	4.14350	23.52298	0.00608	0.698532
57961.799922	13.34448	0.00060	4.14239	23.56949	0.00863	0.665392
57965.767734	13.34493	0.00082	4.15208	23.70713	0.00773	0.689149
57967.666320	13.34593	0.00090	4.15606	23.81222	0.00490	0.686005
57968.665113	13.34688	0.00062	4.15381	23.71546	0.00571	0.672592
57969.722261	13.34611	0.00083	4.14714	23.77195	0.00725	0.652290
57970.625242	13.34483	0.00054	4.15047	23.71987	0.00467	0.673192
57972.725260	13.34169	0.00050	4.14850	23.65182	0.00477	0.667389
57973.771407	13.34392	0.00063	4.14809	23.63687	0.00744	0.658560
57979.769360	13.34582	0.00050	4.14583	23.54671	0.00496	0.682896
57980.810127	13.34516	0.00054	4.14822	23.58886	0.00702	0.674189
57981.796992	13.34631	0.00056	4.14848	23.52290	0.00565	0.686809
58008.702254	13.34802	0.00089	4.15653	23.69043	0.00361	0.658323
58010.723216	13.34529	0.00058	4.13967	23.55485	0.00750	0.665487
58012.711271	13.34544	0.00072	4.14571	23.58195	0.00247	0.685649
58013.723942	13.34664	0.00071	4.14941	23.63280	0.00679	0.674079
58019.583628	13.34294	0.00047	4.15203	23.70121	0.00695	0.695348
58019.594970	13.34336	0.00045	4.15020	23.73355	0.00565	0.705989
58020.562532	13.34361	0.00057	4.15977	23.95944	0.00594	0.708174
58020.703194	13.34296	0.00050	4.14657	23.58017	0.00541	0.709220
58040.509625	13.34225	0.00036	4.15225	23.78077	0.00545	0.657217
58043.657194	13.34466	0.00047	4.13300	23.43135	0.00549	0.645712
58052.713317	13.34239	0.00071	4.13800	23.38341	0.00518	0.714325
58053.625682	13.34317	0.00047	4.13832	23.39911	0.00455	0.665564
58057.551844	13.34349	0.00036	4.13986	23.47777	0.00676	0.658691
58073.581512	13.34419	0.00043	4.12928	23.32211	0.00598	0.687914
58078.508985	13.34369	0.00045	4.13727	23.55402	0.00385	0.636125
58081.509362	13.34665	0.00038	4.13335	23.49838	0.00221	0.603707
58088.509887	13.34626	0.00061	4.13882	23.49049	0.00505	0.658480
58092.516267	13.34486	0.00060	4.14326	23.51556	0.00492	0.685674
58257.823110	13.34927	0.00056	4.15004	23.78038	0.00647	0.594954

Table 6.2 Continued

58258.787502	13.34863	0.00042	4.15249	23.76986	0.00714	0.608255
58259.814041	13.34982	0.00047	4.15489	23.77319	0.00743	0.616551
58260.786176	13.34996	0.00047	4.15319	23.80361	0.00800	0.625607
58271.766034	13.35205	0.00073	4.15061	23.71436	0.00531	0.677293
58272.807692	13.35202	0.00049	4.15572	23.75906	0.00638	0.671367
58273.919551	13.35208	0.00052	4.15124	23.72114	0.00534	0.651597
58274.787272	13.35274	0.00049	4.15265	23.73754	0.00512	0.663489
58275.906328	13.35329	0.00087	4.16342	24.03518	0.00650	0.655012
58288.839357	13.35205	0.00048	4.16083	23.84696	0.00742	0.643797
58290.756183	13.35358	0.00041	4.15789	23.82300	0.00630	0.658918
58292.746354	13.35176	0.00046	4.15062	23.77635	0.00570	0.605126
58293.764194	13.35355	0.00072	4.14734	23.77316	0.00817	0.614805
58294.827451	13.35372	0.00069	4.14888	23.65300	0.00423	0.593206
58295.760238	13.35323	0.00045	4.15876	23.83827	0.00529	0.640370
58299.797697	13.35304	0.00072	4.15286	23.77265	0.00623	0.596563
58310.880989	13.35297	0.00047	4.15063	23.57400	0.00440	0.657555

TABLE 6.3: Gl 832 PFS data

JD-2400000	RV (ms^{-1})	Uncertainty (ms^{-1})
55785.64157	0.0000	0.900
55787.61821	0.0000	0.800
55790.61508	0.3000	0.800
55793.63258	0.8000	0.900
55795.70095	1.2000	0.800
55796.71462	2.5000	0.900
55804.66221	0.2000	0.900
55844.60440	3.1000	0.900
55851.62322	-0.500	0.900
56085.87962	-1.400	0.900
56141.67188	-7.300	0.800
56504.79755	-12.10	1.100
56506.76826	-13.70	1.000
56550.60574	-14.80	0.900
56556.65127	-18.30	1.000
56603.55010	-18.70	0.900

TABLE 6.4: Gl 832 UCLES data

JD-2400000	RV (ms^{-1})	Uncertainty (ms^{-1})
51034.08733	7.5	2.2
51119.01595	14.6	6.0
51411.12220	11.4	3.3
51683.26276	18.0	2.8
51743.14564	19.0	2.7
51767.08125	25.0	2.3
52062.24434	19.8	2.2
52092.16771	9.0	2.5
52128.12730	2.2	4.0
52455.23394	0.5	1.6
52477.14549	10.0	2.6
52859.08771	-4.1	2.1
52943.03605	-5.4	2.7
52946.97093	0.5	1.9
53214.20683	-9.5	2.5
53217.21195	-13.9	2.4
53243.05806	-2.1	2.4
53245.15092	-15.4	2.5
53281.04691	-17.3	2.0
53485.30090	-13.1	2.0
53523.30055	-4.9	1.6
53576.14194	-11.5	1.6
53628.06985	-0.4	5.2
53629.05458	-15.2	2.1
53943.10723	-6.3	1.3
54009.03770	-10.4	1.6
54036.95562	-7.2	1.5
54254.19997	3.2	1.8
54371.06683	0.2	1.6
54375.04476	2.5	1.7
54552.29135	8.7	4.0
54553.30430	17.0	2.8
55102.99894	6.4	2.6
55376.26506	9.2	2.5
55430.16511	15.4	2.5
56087.23879	16.1	2.4
56139.24349	14.5	4.6
56467.24320	1.6	3.0
56499.09217	-6.3	4.0

Bibliography

Astudillo-Defru, N. et al. (Apr. 2017). "Magnetic activity in the HARPS M dwarf sample. The rotation-activity relationship for very low-mass stars through R'(HK)". In: 600, A13, A13. DOI: 10.1051/0004-6361/201527078. arXiv: 1610.09007 [astro-ph.SR].

Astudillo-Defru, Nicola (Mar. 2015). "Search for Earth-like planets in the habitable zone of M-dwarfs". Theses. Université Grenoble Alpes. URL: https://tel.archives-ouvertes.fr/tel-01214382.

Bailey, Jeremy et al. (2009). "A Jupiter-Like Planet Orbiting the Nearby M dwarf GJ 832". In: 690.1, pp. 743–747. DOI: 10.1088/0004-637X/690/1/743. arXiv: 0809.0172 [astro-ph].

Baliunas, Sallie L. et al. (1998). "Activity Cycles in Lower Main Sequence and POST Main Sequence Stars: The HK Project". In: *Cool Stars, Stellar Systems, and the Sun*. Ed. by Robert A. Donahue and Jay A. Bookbinder. Vol. 154. Astronomical Society of the Pacific Conference Series, p. 153.

Barge, P. et al. (May 2008). "Transiting exoplanets from the CoRoT space mission. I. CoRoT-Exo-1b: a low-density short-period planet around a G0V star". In: 482.3, pp. L17–L20. DOI: 10.1051/0004-6361:200809353. arXiv: 0803.3202 [astro-ph].

Barman, Travis (May 2014). "Astronomy: A new spin on exoplanets". In: 509.7498, pp. 41–42. DOI: 10.1038/509041a.

Barning, F. J. M. (Aug. 1963). "The numerical analysis of the light-curve of 12 Lacertae". In: 17, p. 22.

Bonfils, X. et al. (2007). "The HARPS search for southern extra-solar planets. X. A m sin i = 11 M_⊕ planet around the nearby spotted M dwarf <ASTROBJ>GJ 674</ASTROBJ>". In: 474.1, pp. 293–299. DOI: 10.1051/0004-6361:20077068. arXiv: 0704.0270 [astro-ph].

Bonfils, X. et al. (2013). "The HARPS search for southern extra-solar planets. XXXI. The M-dwarf sample". In: 549, A109, A109. DOI: 10.1051/0004-6361/201014704. arXiv: 1111.5019 [astro-ph.EP].

Borucki, William J. et al. (Feb. 2010). "Kepler Planet-Detection Mission: Introduction and First Results". In: *Science* 327.5968, p. 977. DOI: 10.1126/science.1185402.

Boyajian, Tabetha S. et al. (Oct. 2012). "Stellar Diameters and Temperatures. II. Main-sequence K- and M-stars". In: 757.2, 112, p. 112. DOI: 10.1088/0004-637X/757/2/112. arXiv: 1208.2431 [astro-ph.SR].

Bray, R. J., R. E. Loughhead, and C. J. Durrant (1984). *The solar granulation Durrant.*

Chabrier, G. and M. Küker (Feb. 2006). "Large-scale $\alpha\hat{2}$-dynamo in low-mass stars and brown dwarfs". In: 446.3, pp. 1027–1037. DOI: 10.1051/0004-6361:20042475. arXiv: astro-ph/0510075 [astro-ph].

Damasso, M. and F. Del Sordo (Mar. 2017). "Proxima Centauri reloaded: Unravelling the stellar noise in radial velocities". In: 599, A126, A126. DOI: 10.1051/0004-6361/201630050. arXiv: 1612.03786 [astro-ph.EP].

Del Moro, D. (Dec. 2004). "Solar granulation properties derived from three different time series". In: 428, pp. 1007–1015. DOI: 10.1051/0004-6361:20040466.

Desidera, S. et al. (2004). "No planet around HD 219542 B". In: 420, pp. L27–L30. DOI: 10.1051/0004-6361:20040155. arXiv: astro-ph/0405054 [astro-ph].

Donati, J. F. et al. (Oct. 2008). "Large-scale magnetic topologies of early M dwarfs". In: 390.2, pp. 545–560. DOI: 10.1111/j.1365-2966.2008.13799.x. arXiv: 0809.0269 [astro-ph].

Dumusque, X. et al. (Jan. 2011). "Planetary detection limits taking into account stellar noise. I. Observational strategies to reduce stellar oscillation and granulation effects". In: 525, A140, A140. DOI: 10.1051/0004-6361/201014097. arXiv: 1010.2616 [astro-ph.EP].

Faria, J. P. et al. (2016). "Uncovering the planets and stellar activity of CoRoT-7 using only radial velocities". In: 588, A31, A31. DOI: 10.1051/0004-6361/201527899. arXiv: 1601.07495 [astro-ph.EP].

Farr, Will M. et al. (Oct. 2018). "Aldebaran b's Temperate Past Uncovered in Planet Search Data". In: 865.2, L20, p. L20. DOI: 10.3847/2041-8213/aadfde. arXiv: 1802.09812 [astro-ph.SR].

Fulton, Benjamin J. et al. (2018). "RadVel: The Radial Velocity Modeling Toolkit". In: 130.986, p. 044504. DOI: 10.1088/1538-3873/aaaaa8. arXiv: 1801.01947 [astro-ph.IM].

Gaia Collaboration (Apr. 2018). "VizieR Online Data Catalog: Gaia DR2 (Gaia Collaboration, 2018)". In: *VizieR Online Data Catalog*, I/345, pp. I/345.

Gaidos, E. et al. (Sept. 2014). "Trumpeting M dwarfs with CONCH-SHELL: a catalogue of nearby cool host-stars for habitable exoplanets and life". In: 443.3, pp. 2561–2578. DOI: 10.1093/mnras/stu1313. arXiv: 1406.7353 [astro-ph.SR].

Gibson, N. P. et al. (Jan. 2012). "A Gaussian process framework for modelling instrumental systematics: application to transmission spectroscopy". In: 419.3, pp. 2683–2694. DOI: 10.1111/j.1365-2966.2011.19915.x. arXiv: 1109.3251 [astro-ph.EP].

Gomes da Silva, J. et al. (2011). "Long-term magnetic activity of a sample of M-dwarf stars from the HARPS program. I. Comparison of activity indices". In: 534, A30, A30. DOI: 10.1051/0004-6361/201116971. arXiv: 1109.0321 [astro-ph.SR].

Gomes da Silva, J. et al. (May 2012). "Long-term magnetic activity of a sample of M-dwarf stars from the HARPS program . II. Activity and radial velocity". In: 541, A9, A9. DOI: 10.1051/0004-6361/201118598. arXiv: 1202.1564 [astro-ph.SR].

Grunblatt, Samuel K., Andrew W. Howard, and Raphaëlle D. Haywood (2015). "Determining the Mass of Kepler-78b with Nonparametric Gaussian Process Estimation". In: 808.2, 127, p. 127. DOI: 10.1088/0004-637X/808/2/127. arXiv: 1501.00369 [astro-ph.EP].

Hale, George E. (Nov. 1908). "On the Probable Existence of a Magnetic Field in Sun-Spots". In: 28, p. 315. DOI: 10.1086/141602.

Hanuschik, R. W. (2003). "A flux-calibrated, high-resolution atlas of optical sky emission from UVES". In: 407, pp. 1157–1164. DOI: 10.1051/0004-6361:20030885.

Hathaway, David H. (Mar. 2010). "The Solar Cycle". In: *Living Reviews in Solar Physics* 7.1, 1, p. 1. DOI: 10.12942/lrsp-2010-1.

Haywood, R. D. et al. (2014). "Planets and stellar activity: hide and seek in the CoRoT-7 system". In: 443.3, pp. 2517–2531. DOI: 10.1093/mnras/stu1320. arXiv: 1407.1044 [astro-ph.EP].

Haywood, Raphaëlle Dawn (2015). "Hide and Seek: Radial-Velocity Searches for Planets around Active Stars". PhD thesis. University of St Andrews.

Hirzberger, J. et al. (Apr. 1999). "Time Series of Solar Granulation Images. II. Evolution of Individual Granules". In: 515.1, pp. 441–454. DOI: 10.1086/307018.

Howe, Rachel (Feb. 2009). "Solar Interior Rotation and its Variation". In: *Living Reviews in Solar Physics* 6.1, 1, p. 1. DOI: 10.12942/lrsp-2009-1. arXiv: 0902.2406 [astro-ph.SR].

Huélamo, N. et al. (2008). "TW Hydrae: evidence of stellar spots instead of a Hot Jupiter". In: 489.2, pp. L9–L13. DOI: 10.1051/0004-6361:200810596. arXiv: 0808.2386 [astro-ph].

Jenkins, J. S. et al. (2006). "An activity catalogue of southern stars". In: 372.1, pp. 163–173. DOI: 10.1111/j.1365-2966.2006.10811.x. arXiv: astro-ph/0607336 [astro-ph].

Johnson, Marshall C. et al. (2016). "A 12-year Activity Cycle for the Nearby Planet Host Star HD 219134". In: 821.2, 74, p. 74. DOI: 10.3847/0004-637X/821/2/74. arXiv: 1602.05200 [astro-ph.EP].

Kasting, James F., Daniel P. Whitmire, and Ray T. Reynolds (1993). "Habitable Zones around Main Sequence Stars". In: 101.1, pp. 108–128. DOI: 10.1006/icar.1993.1010.

Lafarga, M. et al. (Apr. 2020). "The CARMENES search for exoplanets around M dwarfs. Radial velocities and activity indicators from cross-correlation functions with weighted binary masks". In: 636, A36, A36. DOI: 10.1051/0004-6361/201937222. arXiv: 2003.07471 [astro-ph.IM].

Leighton, Robert B., Robert W. Noyes, and George W. Simon (Mar. 1962). "Velocity Fields in the Solar Atmosphere. I. Preliminary Report." In: 135, p. 474. DOI: 10.1086/147285.

Lindegren, L. et al. (July 2008). "The Gaia mission: science, organization and present status". In: *A Giant Step: from Milli- to Micro-arcsecond Astrometry*. Ed. by W. J. Jin,

I. Platais, and M. A. C. Perryman. Vol. 248. IAU Symposium, pp. 217–223. DOI: 10.1017/S1743921308019133.

Lindegren, Lennart and Dainis Dravins (Apr. 2003). "The fundamental definition of "radial velocity"". In: 401, pp. 1185–1201. DOI: 10.1051/0004-6361:20030181. arXiv: astro-ph/0302522 [astro-ph].

Lo Curto, G. et al. (2015). "HARPS Gets New Fibres After 12 Years of Operations". In: *The Messenger* 162, pp. 9–15.

Lomb, N. R. (1976). "Least-Squares Frequency Analysis of Unequally Spaced Data". In: 39.2, pp. 447–462. DOI: 10.1007/BF00648343.

Macintosh, B. et al. (Oct. 2015). "Discovery and spectroscopy of the young jovian planet 51 Eri b with the Gemini Planet Imager". In: *Science* 350.6256, pp. 64–67. DOI: 10.1126/science.aac5891. arXiv: 1508.03084 [astro-ph.EP].

Mauas, Pablo J. D. (2000). "Building Reliable Models of M Dwarf Chromospheres: The Spectral Diagnostics". In: 539.2, pp. 858–864. DOI: 10.1086/309271.

Mayor, M. et al. (1995). "51 Pegasi". In: *International Astronomical Union Circular* 6251, p. 1.

Mayor, M. et al. (Dec. 2003). "Setting New Standards with HARPS". In: *The Messenger* 114, pp. 20–24.

Mordasini, C. et al. (Feb. 2011). "The HARPS search for southern extra-solar planets. XXIV. Companions to HD 85390, HD 90156, and HD 103197: a Neptune analog and two intermediate-mass planets". In: 526, A111, A111. DOI: 10.1051/0004-6361/200913521. arXiv: 1010.0856 [astro-ph.EP].

Morin, J. et al. (Feb. 2008). "The stable magnetic field of the fully convective star V374 Peg". In: 384.1, pp. 77–86. DOI: 10.1111/j.1365-2966.2007.12709.x. arXiv: 0711.1418 [astro-ph].

Murray, C. D. and A. C. M. Correia (2010). "Keplerian Orbits and Dynamics of Exoplanets". In: *Exoplanets, edited by S. Seager. Tucson, AZ: University of Arizona Press, 2010, 526 pp. ISBN 978-0-8165-2945-2., p.15-23*. Ed. by S. Seager, pp. 15–23.

Parker, Eugene N. (Sept. 1955). "Hydromagnetic Dynamo Models." In: 122, p. 293. DOI: 10.1086/146087.

Pepe, Francesco A. et al. (2010). "ESPRESSO: the Echelle spectrograph for rocky exoplanets and stable spectroscopic observations". In: vol. 7735. Society of Photo-Optical Instrumentation Engineers (SPIE) Conference Series, 77350F. DOI: 10.1117/12.857122.

Queloz, D. et al. (Jan. 2000). "Extrasolar Planets in the Southern Hemisphere: The CORALIE Survey". In: *From Extrasolar Planets to Cosmology: The VLT Opening Symposium*. Ed. by Jacqueline Bergeron and Alvio Renzini, p. 548. DOI: 10.1007/10720961_79.

Queloz, D. et al. (2001). "No planet for HD 166435". In: 379, pp. 279–287. DOI: 10.1051/0004-6361:20011308. arXiv: astro-ph/0109491 [astro-ph].

Queloz, Didier (Jan. 1995). "Echelle Spectroscopy with a CCD at Low Signal-To-Noise Ratio". In: *New Developments in Array Technology and Applications*. Ed. by

A. G. Davis Philip, Kenneth Janes, and Arthur R. Upgren. Vol. 167. IAU Symposium, p. 221.

Quirrenbach, A. et al. (2010). "CARMENES: Calar Alto high-resolution search for M dwarfs with exo-earths with a near-infrared Echelle spectrograph". In: vol. 7735. Society of Photo-Optical Instrumentation Engineers (SPIE) Conference Series, p. 773513. DOI: 10.1117/12.857777.

Rajpaul, V. et al. (2015). "A Gaussian process framework for modelling stellar activity signals in radial velocity data". In: 452.3, pp. 2269–2291. DOI: 10.1093/mnras/stv1428. arXiv: 1506.07304 [astro-ph.EP].

Rasmussen, Carl Edward and Christopher K. I. Williams (2006). *Gaussian Processes for Machine Learning*.

Rast, Mark Peter (Nov. 2003). "The Scales of Granulation, Mesogranulation, and Supergranulation". In: 597.2, pp. 1200–1210. DOI: 10.1086/381221.

Reiners, Ansgar, Nandan Joshi, and Bertrand Goldman (2012). "A Catalog of Rotation and Activity in Early-M Stars". In: 143.4, 93, p. 93. DOI: 10.1088/0004-6256/143/4/93. arXiv: 1201.5774 [astro-ph.SR].

Ricker, George R. et al. (Jan. 2009). "The Transiting Exoplanet Survey Satellite (TESS)". In: *American Astronomical Society Meeting Abstracts #213*. Vol. 213. American Astronomical Society Meeting Abstracts, p. 403.01.

Roberts, S. et al. (Dec. 2012). "Gaussian processes for time-series modelling". In: *Philosophical Transactions of the Royal Society of London Series A* 371.1984, pp. 20110550–20110550. DOI: 10.1098/rsta.2011.0550.

Robertson, Paul et al. (2014). "Stellar activity masquerading as planets in the habitable zone of the M dwarf Gliese 581". In: *Science* 345.6195, pp. 440–444. DOI: 10.1126/science.1253253. arXiv: 1407.1049 [astro-ph.EP].

Saar, Steven H. and Robert A. Donahue (Aug. 1997). "Activity-Related Radial Velocity Variation in Cool Stars". In: 485.1, pp. 319–327. DOI: 10.1086/304392.

Santos, N. C. et al. (Aug. 2013). "SWEET-Cat: A catalogue of parameters for Stars With ExoplanETs. I. New atmospheric parameters and masses for 48 stars with planets". In: 556, A150, A150. DOI: 10.1051/0004-6361/201321286. arXiv: 1307.0354 [astro-ph.SR].

Santos, N. C. et al. (2014). "The HARPS search for southern extra-solar planets. XXXV. The interesting case of HD 41248: stellar activity, no planets?" In: 566, A35, A35. DOI: 10.1051/0004-6361/201423808. arXiv: 1404.6135 [astro-ph.EP].

Scargle, J. D. (1982). "Studies in astronomical time series analysis. II. Statistical aspects of spectral analysis of unevenly spaced data." In: 263, pp. 835–853. DOI: 10.1086/160554.

Schrijver, Carolus J. and Cornelis Zwaan (2000). *Solar and Stellar Magnetic Activity*.

Shulyak, D. et al. (June 2019). "Magnetic fields in M dwarfs from the CARMENES survey". In: 626, A86, A86. DOI: 10.1051/0004-6361/201935315. arXiv: 1904.12762 [astro-ph.SR].

Spiegel, E. A. and J. P. Zahn (Nov. 1992). "The solar tachocline." In: 265, pp. 106–114.

Suárez Mascareño, A. et al. (2015). "Rotation periods of late-type dwarf stars from time series high-resolution spectroscopy of chromospheric indicators". In: 452.3, pp. 2745–2756. DOI: 10.1093/mnras/stv1441. arXiv: 1506.08039 [astro-ph.EP].

Suárez Mascareño, A. et al. (Apr. 2018). "The RoPES project with HARPS and HARPS-N. I. A system of super-Earths orbiting the moderately active K-dwarf HD 176986". In: 612, A41, A41. DOI: 10.1051/0004-6361/201732042. arXiv: 1712.01046 [astro-ph.EP].

Udry, S. et al. (2007). "The HARPS search for southern extra-solar planets. XI. Super-Earths (5 and 8 M{⊕}) in a 3-planet system". In: 469.3, pp. L43–L47. DOI: 10.1051/0004-6361:20077612. arXiv: 0704.3841 [astro-ph].

Vaughan, A. H., G. W. Preston, and O. C. Wilson (1978). "Flux measurements of Ca II and K emission." In: 90, pp. 267–274. DOI: 10.1086/130324.

Wittenmyer, Robert A. et al. (2014). "GJ 832c: A Super-Earth in the Habitable Zone". In: 791.2, 114, p. 114. DOI: 10.1088/0004-637X/791/2/114. arXiv: 1406.5587 [astro-ph.EP].

Wolszczan, A. and D. A. Frail (Jan. 1992). "A planetary system around the millisecond pulsar PSR1257 + 12". In: 355.6356, pp. 145–147. DOI: 10.1038/355145a0.

Wright, Jason T. and B. Scott Gaudi (2013). "Exoplanet Detection Methods". In: *Planets, Stars and Stellar Systems. Volume 3: Solar and Stellar Planetary Systems*. Ed. by Terry D. Oswalt, Linda M. French, and Paul Kalas, p. 489. DOI: 10.1007/978-94-007-5606-9_10.

Zechmeister, M. and M. Kürster (2009). "The generalised Lomb-Scargle periodogram. A new formalism for the floating-mean and Keplerian periodograms". In: 496.2, pp. 577–584. DOI: 10.1051/0004-6361:200811296. arXiv: 0901.2573 [astro-ph.IM].